UC San Diego

UC San Diego Electronic Theses and Dissertations

Title

Topics in kinetics of tokamak edge plasma and laser-plasma interactions

Permalink

Author

Knyazev, Alexey

Publication Date

2023

Peer reviewed|Thesis/dissertation

UNIVERSITY OF CALIFORNIA SAN DIEGO

Topics in kinetics of tokamak edge plasma and laser-plasma interactions

A dissertation submitted in partial satisfaction
of the requirements for the degree
Doctor of Philosophy

in

Engineering Sciences (Engineering Physics)

by

Alexey Knyazev

Committee in charge:

 Sergei I. Krasheninnikov, Chair
 Alexey Arefiev
 Dan Dubin
 Christopher Holland
 George R. Tynan

2023

The Dissertation of Alexey Knyazev is approved, and it is acceptable in quality and form for publication on microfilm and electronically.

University of California San Diego

2023

DEDICATION

To my grandmother.

EPIGRAPH

Спасибо тебе, Господи, что Ты создал все
нужное нетрудным, а все трудное – ненужным.

Григорий Саввич Сковорода, 1772

TABLE OF CONTENTS

ACKNOWLEDGEMENTS

Chapter 5 summarizes the presented work.

2017 Bachelor of Science,
     Moscow Institute of Physics and Technology

2023 Doctor of Philosophy, Engineering Sciences (Engineering Physics)
     University of California San Diego

PUBLICATIONS

Knyazev, A. R., M. Dorf, and S. I. Krasheninnikov. "Implementation and verification of a model linearized multi-species collision operator in the COGENT code." Computer Physics Communications (2023): 108829.

Krasheninnikov, S. I., and **A. R. Knyazev**. "Resonance three-wave interactions and strange attractor." Physics of Plasmas 29, no. 1 (2022).

Knyazev, A. R., and S. I. Krasheninnikov. "Stochastic electron motion in colliding plane waves." Physical Review E 103, no. 6 (2021): 063213.

Knyazev, A. R., Y. Zhang, and S. I. Krasheninnikov. "Laser-driven electron acceleration in nanoplate array targets." Physical Review E 103, no. 1 (2021): 013204.

Zhang, Yanzeng, S. I. Krasheninnikov, and **A. Knyazev**. "Stochastic electron heating in the laser and quasi-static electric and magnetic fields." Physics of Plasmas 25, no. 12 (2018).

ABSTRACT OF THE DISSERTATION

Topics in kinetics of tokamak edge plasma and laser-plasma interactions

by

Alexey Knyazev

Doctor of Philosophy in Engineering Sciences (Engineering Physics)

University of California San Diego, 2023

Sergei I. Krasheninnikov, Chair

Kinetic models are often necessary to adequately describe plasma dynamics. Firstly, important kinetic effects in plasmas can persist even in a fluid parameter regime, such as the thermal force in the Braginskii model. Secondly, many plasmas of interest – such as occur in laser-plasma interactions – are far from the thermal equilibrium assumed by fluid models, and must be described using the Vlasov equation.

Direct kinetic simulations of plasmas are computationally expensive. Therefore, reduced models and simplified problem setups are instrumental to the study of kinetic plasma effects.

This dissertation is divided into three projects, each addressing kinetic plasma

effects with a reduced model.

The first project investigates relativistic electron dynamics in the presence of colliding laser pulses. The stochastic dynamics of an electron in counter-propagating linearly polarized laser beams is analyzed using a recently developed 3/2-dimensional Hamiltonian approach. It is shown that perpendicular canonical momentum suppresses stochasticity, helping to explain the results from recently reported numerical studies of stochastic dynamics in a similar setting. The stochasticity in a perpendicular polarization setup is demonstrated. Lastly, the impact of radiation friction effects is considered, and shown to be negligible in the classical radiation reaction limit.

The second project investigates electron dynamics during laser-target interaction. The model is proposed to describe the laser-driven electron acceleration that occurs when a high-intensity laser interacts with a nanoplate target. Formation of the quasi-static electric and magnetic fields is described, and the residual between these static fields is shown to be crucial for stochastic the electron acceleration beyond the ponderomotive scaling.

The third project is dedicated to reduced modeling of Coulomb collisions in gyrokinetic simulations. A linearized multi-species model collision operator is adapted for the continuum gyrokinetic code COGENT. It is used to simulate highly collisional plasmas to illustrate that the operator recovers both friction and thermal forces of the Braginskii fluid model. The neoclassical transport of heavy impurities simulated with COGENT is shown to agree with previously published theoretical results.

Chapter 1

Introduction

1.1 Kinetic plasma description

Kinetics of the ideal, classical, fully ionized plasma can be described with a system of Boltzmann equations for each plasma species. For s species with charge e_s and mass m_s, the Boltzmann kinetic equation,

$$\frac{\partial f_s}{\partial t} + \frac{d\mathbf{x}_s}{dt}\frac{\partial f_s}{\partial \mathbf{x}_s} + \frac{d\mathbf{P}_s}{dt}\frac{\partial f_\mathrm{s}}{\partial \mathbf{P}_s} = \left(\frac{df_s}{dt}\right)_\mathrm{c}, \tag{1.1}$$

describes particle dynamics in the presence of external forces and the self-consistent fields, where $f_s(\mathbf{x}_s, \mathbf{P}_s, t)d\mathbf{x}_s d\mathbf{P}_s$ is the number of particles in the $d\mathbf{x}_s d\mathbf{P}_s$ phase space volume element of the s species, $\mathbf{x}_s$ (and $\mathbf{P}_s$) are canonical coordinates (and momenta).

For high-temperature plasmas, such as those produced by the laser with relativistic intensity $I \geq 1.37 \times 10^{18}(1\mu\mathrm{m}/\lambda)^2$ W/cm^2 – where λ is the laser wavelength – collisions can be ignored completely, resulting in the Vlasov equation,

$$\frac{\partial f_s}{\partial t} + \frac{d\mathbf{x}_s}{dt}\frac{\partial f_s}{\partial \mathbf{x}_s} + \frac{d\mathbf{P}_s}{dt}\frac{\partial f_\mathrm{s}}{\partial \mathbf{P}_s} = 0. \tag{1.2}$$

Relativistic intensity laser-plasma interaction is considered in Chapter 2 and 3 of this thesis. Observe that the left-hand side of the Vlasov equation is the full-time derivative of $f_\mathrm{s}(\mathbf{x}_\mathrm{s}, \mathbf{P}_\mathrm{s})$ in a phase space, so $Df_s/Dt = 0$ without collisions. This incompressibility
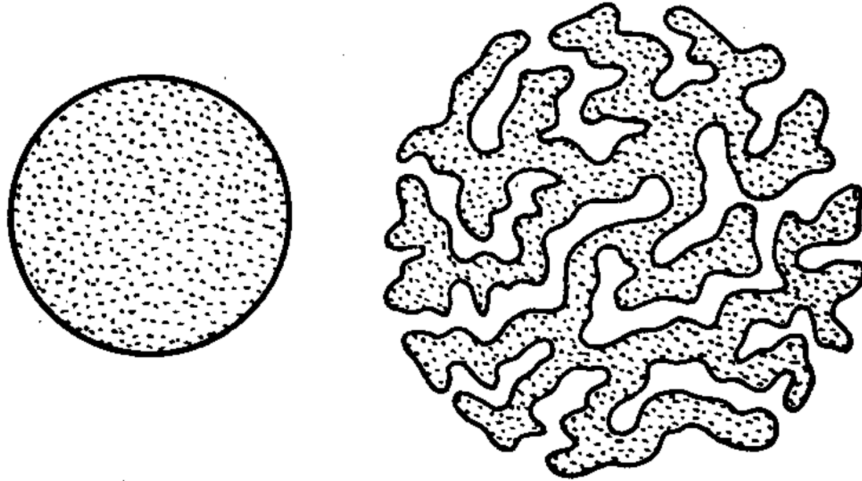
Figure 1.1. Despite that the phase space flow in Vlasov equation Eq. (1.2) is Hamiltonian and therefore volume preserving, stochasticity can cause the "drop" of nearby initial condition to spill over the large "effective" phase space volume. Image taken from [1].

in the phase-space is a consequence of particle dynamics being Hamiltonian. Notably, despite the volume-preserving nature of the Hamiltonian flow, a "drop" of initial conditions – depicted schematically in Figure 1.1 – may spill over the large "effective" phase space volume due to *stochasticity* that will be discussed in the section below.

As will be shown in Chapters 2 and 3 of this thesis, stochastic "spilling" across the phase space may be utilized to accelerate electrons in relativistic laser-plasma interactions. In various relativistic laser setups, stochastic electron heating – triggered by additional perturbation laser or static electromagnetic fields in the plasma – can produce electron energies larger than the maximum energy of the electron quiver motion in the relativistic laser field alone (the so-called *ponderomotive scaling*). Design and analysis of efficient acceleration techniques – such as stochastic acceleration mentioned here – is an active research area, both due to the rapid advancements in high-power laser technology [2] and due to prospective applications for produced energetic electron bunches [3].

Analysis in Chapter 2 and 3 is primarily concerned with the Hamiltonian dynamics of electrons, as is assumed by the Vlasov equation Eq. (1.2). However, certain processes of

interest are not easily handled within the Hamiltonian formalism. One such example is the radiation friction experienced by the electron in a high-intensity laser field, considered in Chapter 2. Another example is the impact of small scale electromagnetic fluctuations [4] – called Coulomb *collisions* – on a single-particle distribution function f_s.

Coulomb collisions are described by a collision operator on the right-hand-side of the kinetic equation Eq. (1.1). The Landau form [5] of the collision operator is often used, suitable for deriving collisional transport of energy, momentum, and particles in Braginskii [6] fluid model. Notably, because the thermal conductivity of the plasma is determined [7] by particles with superthermal energies, the high-collisionality limit analysis of Braginskii-type models is only applicable to plasmas with $\lambda_{\mathrm{C}}/L_{\mathrm{T}} \lesssim 10^{-2}$, where λ_{C} is the Coulomb mean free path of thermal electrons and L_{T} is the characteristic gradient scale length of the plasma temperature profile. Such a high collisionality requirement is not satisfied for parallel transport in typical tokamak-relevant plasmas. As a result, tokamak plasma simulation tools must either implement workarounds in the parallel transport treatment, such as flux limited Braginskii model in the SOLPS-ITER [8] code, or resort to kinetic models. Kinetic simulations of collisional plasma are, however, numerically expensive, and the high computational cost of the Landau operator makes it impractical for many problems of interest. Instead, various reduced operators are used to capture collision effects in the kinetic model. Such reduced operators are typically designed to be simple and numerically efficient, but may decrease simulation fidelity. For example, some reduced operators do not recover any thermal forces between the colliding species, which is important for simulating impurity transport in the tokamak. Chapter 4 of this thesis presents an implementation of the model linearized multi-species operator into a gyrokinetic code. The implemented collision operator is based on the Landau operator, with approximations that allow to circumvent numerically expensive steps by analytical treatment. The resulting model operator recovers thermal and friction forces as they appear in the Braginskii model.

1.2 Cyclic coordinates and integrals of motion

If the Hamiltonian of a system does not depend on a certain coordinate x_c, such coordinate is called cyclic, and its conjugate momentum is an integral of motion,

$$\frac{dP_c}{dt} = -\frac{\partial H}{\partial x_c} = 0. \tag{1.3}$$

More generally, Nether's theorem – stating the existence of a motion integral associated with a symmetry of the Hamiltonian – can be reduced to a cyclic coordinate argument above. For example, consider a setup from Chapter 3, where a particle of charge q and mass m interacts with a static electric field described by a scalar potential $U(y)$, a static magnetic field described by the vector potential $A_B(y)\mathbf{e}_z$, and an electromagnetic wave described by the vector potential $A(ct - kz)\mathbf{e}_y$. The dynamics of such a particle is described by the extended Hamiltonian,

$$H_e = P_t + mc^2\sqrt{1 + \frac{P_x^2}{m^2c^2} + \frac{(P_y + \frac{q}{c}A(ct - kz))^2}{m^2c^2} + \frac{(P_z + \frac{q}{c}A_B(y))^2}{m^2c^2}} + qU(y), \tag{1.4}$$

where t is the canonical coordinate with the corresponding momentum $P_t = -\gamma mc^2 - qU(u)$. Since H_e does not depend on x, the canonical momentum P_x is conserved

$$\frac{dP_x}{dt} = -\frac{\partial H_e}{\partial x} = 0. \tag{1.5}$$

Furthermore, observe that t and z coordinates appear in H_e as combination $ct - kz$. Accordingly, coordinate transformation $t' = t + æ/\omega$, $z' = z + æ/k$ keeps H_e unchanged. Parameter $æ$ can be used instead of z as a canonical coordinate, and the corresponding

canonical momentum is conserved since æ does not enter H_e explicitly,

$$\frac{dP_æ}{dt} = \frac{d}{dt}\left(\frac{P_t}{\omega} + \frac{P_z}{k}\right) = \frac{d}{dt}(P_t + cP_z) = \tag{1.6}$$

$$= \frac{d}{dt}(-\gamma mc^2 - qU(y) + c[\gamma mv_z + \frac{q}{c}A_B(y)]) = \tag{1.7}$$

$$= -\frac{d}{dt}\left(\gamma mc^2\left(1 - \frac{v_z}{c}\right) + q\big[(U(y) - A_B(y)]\big]\right) = -\frac{\partial H_e}{\partial æ} = 0. \tag{1.8}$$

Integrals of motion reduce the dimensionality of the system. The next section explains how the dimensionality of the problem can have significant implications for the character of dynamics.

1.3   Stochasticity in Hamiltonian systems

Dynamics of nonlinear systems can become stochastic. Stochasticity – also referred to as "chaos" – is a special kind of instability that occurs in nonlinear dynamical systems. Its distinguishing characteristic is that, despite the deterministic nature of equations of motion, various characteristics of the system behave like random quantities. Stochasticity is surprisingly common in nonlinear Hamiltonian systems. Chapters 2 and 3 of this thesis demonstrate examples of stochastic electron dynamics in different laser plasma setups, and investigate the role of chaos in the electron acceleration. The rest of this section introduces the *stochasticity criterion* $K \gtrsim 1$, that will later be used in electron dynamics analysis.

It is important to emphasize that the stochastic trajectories in classical (i.e., not quantum) systems are produced from deterministic Hamiltonian equations, without any ad hoc random forces. Notably, stochastic dynamics of the underlying deterministic system often serves as justification for including random forces – that are also often called "stochastic" – to capture the phenomenology of the dynamics with a reduced model. One such example is a Langevin equation [9] describing the Brownian motion [10] of a suspended body due to interactions with a heat bath of other particles in a fluid. Another

example [11] is "stochastic" description of the wave propagation in random media. In this thesis, the terms stochasticity and chaos will be both used to describe chaotic dynamics in deterministic Hamiltonian systems [12, 13].

Stochasticity requires an instability of the system's motion. One of the commonly occurring instabilities that lead to stochastic dynamics is *phase-stretching* instability. It can be illustrated by Fermi's problem of a ball bouncing between two walls [14], proposed to explain the acceleration mechanism [15] of charged particles interacting with magnetic clouds in space. Let the two walls be a distance L apart, with the moving wall position given by $x = L + d\sin(\omega t)$, $d \ll L$. The ball dynamics is trivial everywhere except during collisions with the moving wall. Therefore, given time t_n and ball velocity v_n after the last moving wall collision, one can calculate the time of the next collision t_{n+1} and the velocity v_{n+1} that results from it. Taking the ball to be much faster than the wall $v \gg \omega d$, the motion can be described with a trajectory mapping,

$$v_{n+1} = v_n + 2\omega d \sin \psi_n, \tag{1.9}$$

$$\psi_{n+1} \approx \psi_n + \frac{2L\omega}{v_{n+1}} \approx \tag{1.10}$$

$$\approx \psi_n + \frac{2L\omega}{v_n}\left(1 - \frac{v_{n+1} - v_n}{v_n}\right) \approx \tag{1.11}$$

$$\approx \psi_n + \frac{2L\omega}{v_n} - \frac{4L\omega^2 d}{v_n^2}\sin \psi_n \quad \text{mod } 2\pi, \tag{1.12}$$

where $\psi = \omega t$ is the phase of the moving wall. Observe that even if velocity v does not change much during collisions $\delta v \sim \omega d \ll v$, the phase ψ can change significantly. The phase stretching instability can occur if

$$\left|\frac{\delta \psi_{n+1}}{\delta \psi_n} - 1\right| \approx \frac{4L\omega^2 d}{v_n^2}|\cos \psi_n| \equiv K|\cos \psi_n| > 1, \tag{1.13}$$

and can cause the onset of stochasticity. Since $K > 1$ is necessary for instability, there

6

exists an upper bound on the energy of the ball, $v^2 \lesssim 4L\omega^2 d$.

Note that stochastic dynamics is not possible in one-dimensional conservative systems $H(x, P)$. The stochastic motion in the ball problem considered above becomes possible due to explicit time-dependence $H(x, P, t)$, which increases the dimensionality of the phase space. Indeed, as was illustrated in the section on cyclic coordinates above, time can serve as a canonical coordinate in the extended Hamiltonian $H_e(x, P, t, P_t) = P_t + H = 0$. Extended Hamiltonian shows that explicit time dependence of $H(x, P, t)$ adds another phase space dimension, $dP_t/dt = -\partial H_e/\partial t \neq 0$. Because of the degeneracy $H_e \equiv 0$ of the extended Hamiltonian treatment, time-dependent $H(x, P, t)$ systems are often called 3/2-dimensional instead of 2-dimensional.

If the motion is described by a 2-dimensional Hamiltonian H occurs in the finite volume of phase space, surfaces of constant H are nested tori in the action-angle variables. Such tori divide the 2-dimensional space into two subspaces, restricting [13] stochasticity to the finite volume of the phase space. For higher dimensions, this is not the case, and stochasticity can explore the entire phase space via Arnold diffusion. This highlights the uniqueness of stochastic dynamics in 2-dimensional systems.

Chapter 2

Stochastic electron motion in colliding plane waves

Stochastic dynamics of electrons interacting with multiple electromagnetic waves has been studied using Hamiltonian formalism [16, 17] and investigated via numerical simulations [18, 19, 20, 21]. Recently, a novel approach [22] was proposed, where the dynamics of the relativistic electron in two collinearly polarized counter-propagating plane waves was described with a 3/2-dimensional Hamiltonian, allowing to apply the techniques used in previous studies of stochastic dynamics in such systems [13, 12]. However, the effects of perpendicular canonical momenta $\mathbf{P}_\perp$ of the electron were not considered in the previous analysis of stochasticity. Considering these effects enables better understanding of the recent numerical results of stochastic heating in colliding laser pulses, such as the dependence on the initial laser phases [20].

In this chapter, we expand on the previous stochastic motion analysis [22] to account for perpendicular canonical momenta $\mathbf{P}_\perp$, and allow for an arbitrary angle between linear polarizations of the waves. We discuss the effect of $\mathbf{P}_\perp$ on the stochastic heating, and relate that effect to the impact of the initial laser phases. Finally, we consider stochastic heating in the presence of radiation friction.

2.1 Stochastic motion

To provide context for the present discussion, it is instructive to revisit the well-known problem of the interaction between a single electron in vacuum with the laser pulse described by a vector potential $\mathbf{a}_1 = a_1 \sin(\eta)\mathbf{e}_{\mathrm{x}}$, where $\eta = t - z$, $a_1 = eE_1/mc\omega$ is the normalized amplitude of the vector potential, E_1 is the maximum electric field of the laser, λ is the laser wavelength, c is speed of light in vacuum, and m and $-e$ are electron's mass and charge, respectively. In what follows, we use dimensionless units, normalized by the introduced constants as follows: length is normalized by $k = 2\pi/\lambda$, time by ω, electron's velocity $\mathbf{v}$ and canonical momenta $\mathbf{P}$ by c and mc, respectively, electric and magnetic fields by $e/mc\omega$. The outlined problem has three well-known integrals of motion,

$$\gamma - P_{\mathrm{z}} = H = const, \ P_{\mathrm{x,y}} = const, \tag{2.1}$$

where $P_{\mathrm{x,y,z}}$ are components of $\mathbf{P} = \gamma\mathbf{v} - \mathbf{A}$, γ is the Lorentz factor of the electron, and $\mathbf{A}$ is the vector potential of electric $-\partial_t\mathbf{A}$ and magnetic $\nabla \times \mathbf{A}$ field. In the reference setup $\mathbf{A}$ equals simply $\mathbf{a}_1$. From the integrals of motion in Eqs. (2.1) follow the expression for the Lorentz factor of the electron,

$$\gamma = \frac{1}{2}\Big(H + \frac{\mathcal{E}_p}{H}\Big), \tag{2.2}$$

where $\mathcal{E}_p = 1 + (P_{\mathrm{x}} + A_{\mathrm{x}})^2 + (P_{\mathrm{y}} + A_{\mathrm{y}})^2$. In the rest of the chapter, we will refer to the maximum of Eq. (2.2) as ponderomotive scaling γ_{p}.

Now, consider that a second laser was added to the setup, described by $\mathbf{a}_2 = a_2 \sin(k_2\tau)(\alpha\mathbf{e}_{\mathrm{x}} + \sqrt{1 - \alpha^2}\mathbf{e}_{\mathrm{y}})$, where $\tau = t + z$, k_2 is the wavenumber of the second laser, and α is the cosine of the angle between $\mathbf{a}_1$ and $\mathbf{a}_2$. Introduction of $\mathbf{a}_2$ breaks the conservation of H, and it was shown that even $a_2 \ll a_1$ can enhance the maximum Lorentz factor γ. Significant physical insight into this phenomenon was obtained by using

a 3/2-dimensional Hamiltonian description [22] of the electron dynamics in colliding laser beams, where it was shown that the role of the perturbation laser $\mathbf{a}_2$ is to onset stochasticity in H, with the stochastic change in H then leading to increase in electron energy γ_{p}. The previously performed analysis of stochasticity [22] was, however, limited to the case of parallel pulse polarization with both lasers propagating along the general momenta of the electron, $P_\perp = 0$. In this section, we will generalize the analysis of stochastic heating to the case of $P_\perp \neq 0$. We show that both $P_{\mathrm{x}} \gg a_1$ and $P_{\mathrm{y}} \gg a_1$ suppress stochasticity. For cases where stochasticity is still present, we show that $P_{\mathrm{y}} > 0$ and $P_{\mathrm{x}} \gtrsim a_1$ increases the lower stochastic limit $H_{\min}$, while keeping the higher stochastic limit $H_{\max}$ intact. Based on the $H_{\min/\max}$ limits, we explain how $|P_{\mathrm{x}}|$ and $|P_{\mathrm{y}}|$ affect the limits of stochastic heating relative to the ponderomotive scaling $\max(\gamma_s)/\mathcal{E}_p$, where γ_s is the ponderomotive scaling Eq. (2.2) for the initial value of the dephasing rate H_0. We verify our analysis with a series of Poincaré maps obtained from numerical integration of Eqs. (2.3-2.5) below.

We begin by describing the dynamics of the electron interacting with both laser beams $\mathbf{A} = \mathbf{a}_1 + \mathbf{a}_2$ as a 3/2D Hamiltonian [22] system:

$$
\begin{aligned}
H = \frac{1}{\chi}\Bigg[&1 + \big(P_{\mathrm{x}} + a_1 \sin(\eta) + \alpha a_2 \sin(k_2\tau)\big)^2 \\
&+ \big(P_{\mathrm{y}} + \sqrt{1-\alpha^2}\, a_2 \sin(k_2\tau)\big)^2 \Bigg] = \gamma - P_{\mathrm{z}},
\end{aligned}
\tag{2.3}
$$

$$
\frac{d\eta}{d\tau} \equiv \dot{\eta} = -\frac{\partial H}{\partial \chi} = \frac{H}{\chi},
\tag{2.4}
$$

$$
\frac{d\chi}{d\tau} \equiv \dot{\chi} = \frac{1}{\chi}\left\{ a_1 \cos(\eta)\left[P_{\mathrm{x}} + a_1 \sin(\eta) + a_2 \sin(k_2\tau)\right]\right\},
\tag{2.5}
$$

where $\chi = \gamma + P_{\mathrm{z}}$. Because the onset of stochasticity is typically attributed to the overlap of high harmonic resonances, [13] it is instructive to begin analysis with the study of the Fourier harmonics $\hat{\chi}_0(\Omega)$ of the unperturbed ($a_2 = 0$) $\chi_0(\tau)$ electron motion, and analyze how the spectrum depends on $P_{\mathrm{x,y}}$. As Fig. (2.1) illustrates, the unperturbed electron motion $\chi_0(\tau)$ is a nonlinear periodic oscillation with base frequency Ω, and so the

Fourier spectrum consists of discrete harmonics $\hat{\chi}_{0,n}$, where n is the harmonic's number. A typical $\hat{\chi}_0(\Omega)$ spectrum has a tail of Fourier harmonics with power law amplitude decay $|\hat{\chi}_{0,n}| \propto 1/n^2$, followed by an exponential cut-off $|\hat{\chi}_{0,n}| \propto \exp[-(n - n_c)]$, where n_c is the cut-off harmonic number,

$$n_c^2 = \frac{\Omega_c^2}{\Omega^2} \approx \frac{1}{\Omega^2} \max\left(\frac{1}{\chi}\frac{d^2\chi}{d\tau^2}\right). \tag{2.6}$$

The cut-off frequency $\Omega_c \approx \max(\ddot{\chi}_0/\chi_0)$ corresponds to the most rugged parts of $\chi_0(\tau)$. Unless $P_x \approx a_1$, $\max(\ddot{\chi}_0/\chi_0)$ occurs at minima $\min(\chi_0) \equiv \chi_m$ along the unperturbed trajectory, so we can estimate cutoff frequency as

$$\begin{aligned}
\Omega_c^2 = \left.\frac{1}{\chi}\frac{d^2\chi}{d\tau^2}\right|_{\chi_m} &= 2a_1 H^4 \times \\
&\times \frac{a_1 \cos^2(\eta_m) - \sin(\eta_m)[P_x + a_1\sin(\eta_m)]}{(1 + P_y^2 + [P_x + a_1\sin(\eta_m)]^2)^3},
\end{aligned} \tag{2.7}$$

where η_m is the value of η corresponding to χ_m. It follows from the Hamiltonian Eq. (2.3) that $\sin(\eta_m) = -a_1/P_x$ for $|P_x| < a_1$, and $\sin(\eta_m) = -P_x/|P_x|$ otherwise. We can use Eqs. (2.6, 2.7) to determine the number of unsuppressed Fourier harmonics n_c by comparing Ω_c with the frequency of unperturbed motion Ω. To find Ω, we solve for implicit $\eta_0(\tau)$ dependence

$$\begin{aligned}
\tau + const = \frac{1}{H^2}\bigg(&\left(1 + P_x^2 + P_y^2 + \frac{a_1^2}{2}\right)\eta_0 \\
&- 2a_1 P_x \cos(\eta_0) - \frac{a_1^2}{4}\sin(2\eta_0)\bigg),
\end{aligned} \tag{2.8}$$

and calculate the unperturbed frequency as

$$\Omega = \frac{2\pi}{\tau(\eta_0 + 2\pi) - \tau(\eta_0)} = \frac{H^2}{1 + P_x^2 + P_y^2 + a_1^2/2}. \tag{2.9}$$

11

Combining Eq. (2.6) with results from Eqs. (2.7, 2.9) gives

$$n_c^2 = \frac{2a_1(1 + P_x^2 + P_y^2 + a_1^2/2)^2(|P_x| - a_1)}{[1 + P_y^2 + (|P_x| - a_1)^2]^3} \tag{2.10}$$

for $|P_x| \gg a_1$ case and

$$n_c^2 = \frac{2(1 + P_x^2 + P_y^2 + a_1^2/2)^2(a_1^2 - P_x^2)}{(1 + P_y^2)^3} \tag{2.11}$$

in $|P_x| \ll a_1$ case. Estimates Eq. (2.10, 2.11) agree with Fourier transforms $\hat{\chi}_0$ shown in Fig. (2.1), where the sharp corners in $P_x \ll a_1$ case results in a long tail of harmonics, while $P_x \gg a_1$ case has virtually instant exponential cut-off of its spectra. It follows from Eqs. (2.10, 2.11) that both $|P_x| \gg a_1$ and $|P_y| \gg a_1$ result in low frequency cutoff $\Omega_c \approx \Omega$ and therefore suppress stochasticity. However, for moderate values of $|P_x|$ and $P_y|$, there exists a long tail of unsuppressed Fourier harmonics in the spectrum of unperturbed motion. From Chirikov's stochasticity criterion, this long tail in the spectrum allows for island overlap and results in a wider stochastic region [13].

Our next step is to determine how components of canonical momenta $P_\perp$ affect the stochasticity boundaries $H_{\max/\min}$. For the electron with initial Hamiltonian H_0, Eq. (2.2) predicts that increased stochastic region will subsequently lead to further heating for cases where stochastic limits $H_{\max} > \mathcal{E}_p$ or $H_{\min} < 1$. To find the $H_{\max/\min}$ limits, we note that the evolution of Hamiltonian

$$\frac{dH}{d\tau} = \frac{2a_2 k_2 \cos(k_2\tau)}{\chi} \left[\alpha P_x + \sqrt{1 - \alpha^2} P_y + \right.$$
$$\left. + \alpha a_1 \sin(\eta) + a_2 \sin(k_2\tau) \right] \tag{2.12}$$

is adiabatic outside of regions with minimal χ. If the second laser $\mathbf{a}_2$ is a perturbation $a_2 \ll a_1$, from Eqs.(2.3,2.12) follows that the value of H changes during "kicks" at $\sin(\eta) = -a_1/P_x$ for $P_x < a_1$ and $\sin(\eta) = -P_x/|P_x|$ otherwise, as illustrated in Fig. (2.2).
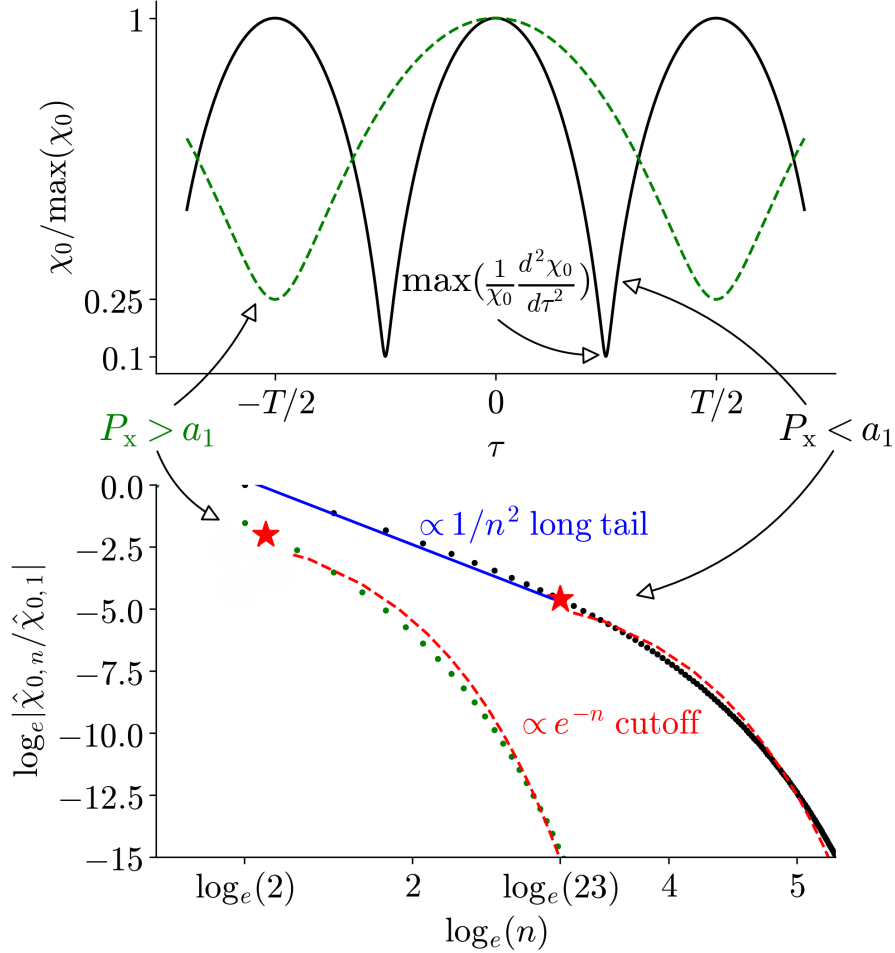
Figure 2.1. Top panel: Unperturbed trajectories $\chi_0(\tau)$ for $P_{\mathrm{x}} < a_1$ ($P_{\mathrm{x}} = 0$, $P_{\mathrm{y}} = 0$, $a_1 = 3.0$ for black solid curve), and for $P_x > a_1$ ($P_{\mathrm{x}} = 15$, $P_{\mathrm{y}} = 0$, $a_1 = 5.0$ for green dashed curve). Bottom panel: Corresponding magnitudes of normalized harmonics $|\hat{\chi}_{0,n}|$ for $P_{\mathrm{x}} > a_1$ (curve on the left), and for $P_{\mathrm{x}} < a_1$ (curve on the right). The blue solid line shows the long tail of Fourier harmonics, and red dashed curves show the exponential decay of harmonic amplitudes. Red stars show the exponential cut-off estimates (2.10) and (2.11)
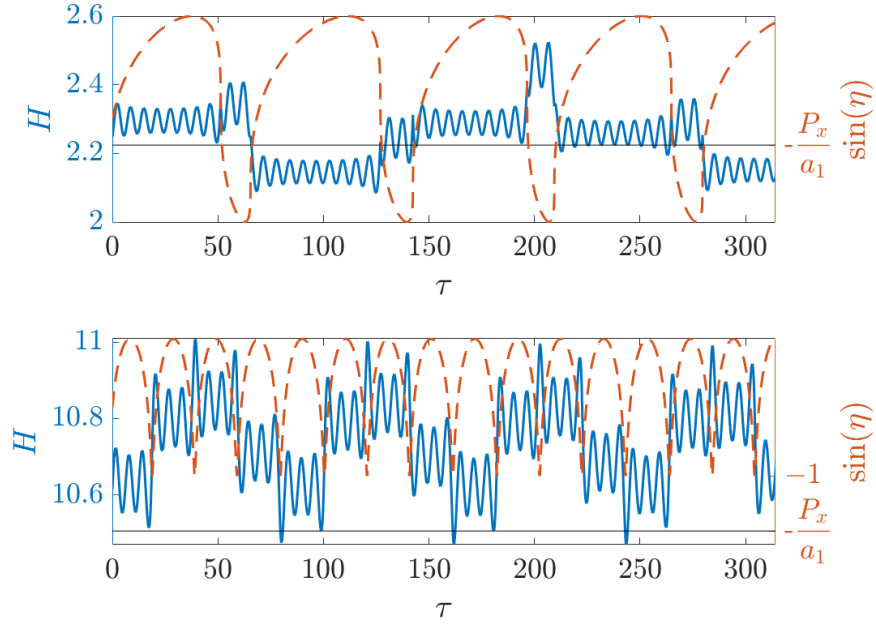
Figure 2.2. Hamiltonian H (solid blue curves) and $\sin(\eta)$ (dashed orange curves) for $a_1 = 10$, $a_2 = 0.1$, $k_2 = 1$. The top panel shows case with $P_{\mathrm{x}}/a_1 \approx 0.25$, where "kicks" occur at $\sin(\eta) = -a_1/P_{\mathrm{x}}$. The bottom panel shows a case with $P_{\mathrm{x}}/a_1 = 1.8$, where "kicks" occur at $\sin(\eta) = -P_{\mathrm{x}}/|P_{\mathrm{x}}| = -1$

The change in H during one kick is

$$\Delta H_n = \int \frac{dH}{d\tau} d\tau = \int \frac{\chi}{H} \frac{dH}{d\tau} d\eta, \tag{2.13}$$

and the difference in phase of $\mathbf{a}_2$ between two consecutive kicks is

$$\Delta \psi_n = \frac{2\pi k_2}{\Omega_{n+1}} = \frac{2\pi k_2}{H_{n+1}^2}\left(1 + P_{\mathrm{x}}^2 + P_{\mathrm{y}}^2 + \frac{a_1^2}{2}\right), \tag{2.14}$$

if $|P_{\mathrm{x}}| > a_1$, and

$$\Delta \psi_n = \frac{(\pi \pm 2\arcsin(P_{\mathrm{x}}/a_1))k_2}{H_{n+1}^2}\left(1 + P_{\mathrm{x}}^2 + P_{\mathrm{y}}^2 + \frac{a_1^2}{2}\right) \tag{2.15}$$

14

otherwise. The sequence of kicks described by (2.13-2.15) will lead to stochasticity if [13]

$$K \equiv \left| \frac{d\Delta\psi_n}{dH_{n+1}} \frac{d\Delta H_n}{d\psi_n} \right| \gtrsim 1. \tag{2.16}$$

From Eq. (2.16), we can obtain the limits of stochasticity $H_{\mathrm{max/min}}$, and the corresponding maximum electron energy (2.2). Details of the calculation are outlined in equations (2.17-2.20) below, followed by the resulting expressions for stochastic boundaries.

As discussed above, the motion outside the kicks regions can be approximated as adiabatic, allowing to substitute the unperturbed trajectory Eq. (2.8) into Eq. (2.12) for evaluating the integral in Eq. (2.13). For kicks in $|P_{\mathrm{x}}| < a_1$ regime, the outlined substitution yields

$$\begin{aligned}
k_2\tau = \tilde{\phi} + \frac{k_2}{H^2}\bigg(&[1 + P_{\mathrm{x}}^2 + P_{\mathrm{y}}^2 + \frac{a_1^2}{2}]\eta - \\
&- 2P_{\mathrm{x}}^2 \sin(\eta) - 2P_{\mathrm{x}}\sqrt{a_1^2 - P_{\mathrm{x}}^2}\cos(\eta) + \\
&(\frac{P_{\mathrm{x}}^2}{2} - \frac{a_1^2}{4}\sin(2\eta)) + \frac{1}{2}P_{\mathrm{x}}\sqrt{a_1^2 - P_{\mathrm{x}}^2}\cos(2\eta)\bigg),
\end{aligned} \tag{2.17}$$

where

$$\tilde{\phi} = const - \frac{k_2}{H^2}\Big(1 + P_{\mathrm{x}}^2 + P_{\mathrm{y}}^2 + \frac{a_1^2}{2}\Big)\arcsin(\frac{P_{\mathrm{x}}}{a_1}). \tag{2.18}$$

Note that in the stochastic regime where H exhibits random behavior, the $\tilde{\phi}$ also becomes random. To simplify the notation below, we combine $\tilde{\phi}$ with all other constants independent of η. We can now approximate the trajectory around the kick with a Taylor expansion of Eq. (2.17) at $\sin(\eta_m) = -P_{\mathrm{x}}/a_1$, allowing for the following approximation for integrals

in (2.13):

$$\int_{\tau_{\text{kick}}} \cos(k_2\tau)d\eta = \int_{-\infty}^{\infty} \cos(\tilde{\phi} + \frac{k_2}{H^2}(1 + P_{\text{y}}^2)\eta +$$
$$\frac{1}{3}(a_1^2 - P_{\text{x}}^2)\eta^3 + P_{\text{x}}\sqrt{a_1^2 - P_{\text{x}}^2}\eta^4 - \frac{1}{60}(4a_1^2 - 7P_{\text{x}}^2)\eta^5)d\eta. \tag{2.19}$$

The phase of cosine terms in integral Eq. (2.19) varies rapidly away from the $\eta = 0$ point, and so for asymptotic analysis is suffices to keep the lowest nonlinear term (η^3 for $P_{\text{x}} < a_1$ and η^5 for $P_{\text{x}} = a_1$).

Analysis done in Eq. (2.17-2.19) can be repeated for $P_{\text{x}} \gtrsim a_1$, where kicks occur at $\sin(\eta_m) = -P_{\text{x}}/|P_{\text{x}}|$, and the resulting approximations for integrals in Eq. (2.13) is different from Eq. (2.19):

$$\int_{\tau_{\text{kick}}} \cos(k_2\tau)d\eta = \int_{-\infty}^{\infty} \cos(\tilde{\phi} + \frac{k_2}{H^2}(1 + P_{\text{y}}^2 +$$
$$+ (P_{\text{x}} - a_1)^2)\eta + \frac{a_1}{3}(P_{\text{x}} - a_1)\eta^3 - \frac{a_1}{60}(4a_1 - P_{\text{x}})\eta^5)d\eta. \tag{2.20}$$

For even larger $P_{\text{x}} \gg a_1$ values, the kicks approximation is no longer valid, and the motion is non-stochastic in agreement with the analysis of trajectory spectra Eq. (2.10).

Note that in the Hamiltonian description, the phase trajectory explicitly depends solely on $\mathbf{P}_\perp$ and the initial conditions $\eta(\tau_0)$, $\chi(\tau_0)$, and does not depend on initial phases ϕ_1 and ϕ_2 of the lasers. In the previous study of interaction between the multi-picosecond laser and the overdense plasma target, [20] stochastic electron dynamics of the electron in the presence of incident and reflected laser pulses was numerically simulated using non-canonical variables $\gamma\mathbf{v}$, $a_1\sin(\phi_1)$, $a_2\sin(\phi_2)$ to describe the electron dynamics, resulting in appearance of laser phases ϕ_1 and ϕ_2 in final answer. The use of canonical variables χ and η (η corresponding to "phase slip" from [20]) enables to understand the physics of the stochasticity onset, illustrating that stochasticity is impacted by canonical momenta $\mathbf{P}_\perp$ rather than the laser phases.

Equipped with approximations Eq. (2.19)-(2.20), we can now evaluate integral Eq. (2.13) in $P_\mathrm{x} < a_1$, $P_\mathrm{x} = a_1$ and $P_\mathrm{x} > a_1$ regimes, and assess the impact of P_x and P_y on the stochastic boundaries $H_\mathrm{max/min}$. For moderate values of $P_\mathrm{x} < a_1$, "kicks" correspond to $\sin(\eta_m) = -P_\mathrm{x}/a_1$, giving the stochasticity condition

$$\left| 8\pi a_2 \left(\sqrt{1-\alpha^2} \frac{a_1^{5/3}|P_\mathrm{y}|\beta^{5/2}}{(a_1^2 - P_\mathrm{x}^2)^{1/3}} \mathrm{Ai}\left[\frac{a_1^{2/3}(1+P_\mathrm{y}^2)\beta}{(a_1^2 - P_\mathrm{x}^2)^{1/3}} \right] - \alpha \frac{a_1^{4/3}\beta^2}{(a_1^2 - P_\mathrm{x}^2)^{1/6}} \mathrm{Ai'}\left[\frac{a_1^{2/3}(1+P_\mathrm{y}^2)\beta}{(a_1^2 - P_\mathrm{x}^2)^{1/3}} \right] + \right. \right.$$
$$\left. \left. + \frac{a_1^{5/3} a_2 \beta^{5/2}}{2^{1/3}(a_1^2 - P_\mathrm{x}^2)^{1/3}} \mathrm{Ai}\left[\frac{(2a_1)^{2/3}(1+P_\mathrm{y}^2)\beta}{(a_1^2 - P_\mathrm{x}^2)^{1/3}} \right] \right)\left(1 + P_\mathrm{x}^2 + P_\mathrm{y}^2 + \frac{a_1^2}{2} \right)\left[\pi \pm 2\arcsin\left(\frac{P_\mathrm{x}}{a_1} \right) \right] \right| \gtrless 1, \tag{2.21}$$

where we introduced parameter $\beta = (k_2/a_1 H^2)^{2/3}$. For $P_\mathrm{x} \gtrsim a_1$, the stochasticity condition is

$$\left| \frac{8\pi^2 a_1^{4/3} a_2 \beta^{5/2}}{(P_\mathrm{x} - a_1)^{1/3}} \left(\left(\alpha(P_\mathrm{x} - a_1) + \sqrt{1-\alpha^2}P_\mathrm{y} \right) \mathrm{Ai}\left[\frac{(1 + (P_\mathrm{x} - a_1)^2 + P_\mathrm{y}^2)a_1^{1/3}\beta}{(P_\mathrm{x} - a_1)^{1/3}} \right] + \right. \right.$$
$$\left. \left. + \frac{a_2}{2^{1/3}} \mathrm{Ai}\left[\frac{(1 + (P_\mathrm{x} - a_1)^2 + P_\mathrm{y}^2)(4a_1)^{1/3}\beta}{(P_\mathrm{x} - a_1)^{1/3}} \right] \right)\left(1 + P_\mathrm{x}^2 + P_\mathrm{y}^2 + \frac{a_1^2}{2} \right) \right| \gtrless 1. \tag{2.22}$$

To compare Eq. (2.21) and Eq. (2.22) with results obtained from numerically integrating Eqs. (2.3-2.5), we calculated the Poincaré maps of the electron's dynamics in lasers with various a_1, a_2, k_2, α, for various initial H and $\mathbf{P}_\perp$. Resulting Poincaré maps (see Fig. (2.3) for example) allow to estimate the stochastic boundary $\beta_\mathrm{max/min}$, since

$$H_\mathrm{min/max} = \sqrt{k_2/a_1 \beta_\mathrm{max/min}^{3/2}}. \tag{2.23}$$

Figure (2.4) demonstrates the agreement between estimates from Eq. (2.21) and Eq. (2.22) and numerical simulations with initial $\beta = (0.1)^{2/3}$. Despite preserved KAM surfaces (such as the smooth curve on the top and island in the Fig. (2.3)) preventing the precise measurement of the stochastic boundary in some simulations, results shown in Fig. (2.4)
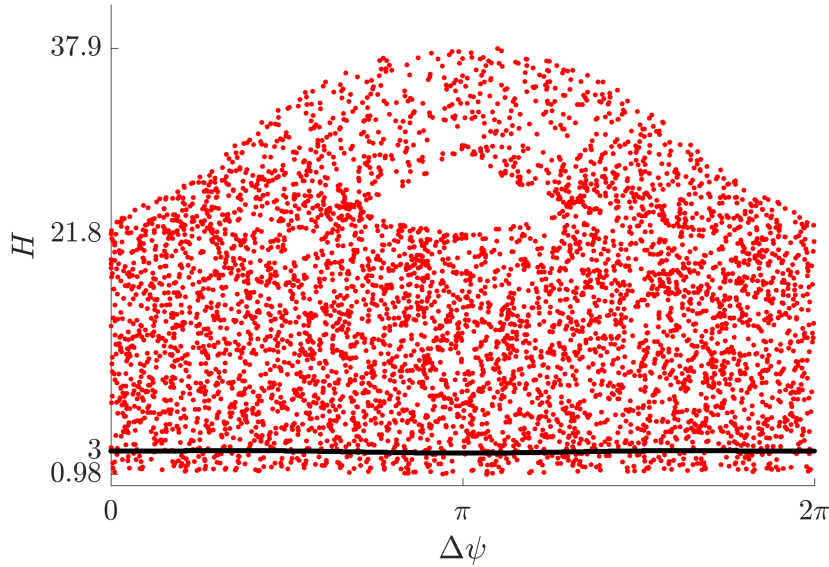
Figure 2.3. Poincaré cross-sections for electron with initial $H(0) = 3$, $\eta(0) = 0$, and $\mathbf{P}_\perp = P_y \mathbf{e}_y$ from a setup with parameters: $a_1 = 10$, $a_2 = 1$, $k_2 = 9$, $\alpha = 1$. Red dots show stochastic motion for $P_y = 2$, black line at $H = 3$ shows regular motion for $P_y = 5$

show good agreement of the numerical results with analysis.

From estimates in Eq. (2.21) and Eq. (2.22), and given the asymptotics of Airy function ($\mathrm{Ai}(x) \sim 0.36 - 0.26x$ for $x \to 0$ and $\mathrm{Ai}(x) \sim 0.28 x^{1/4} \exp(-2x^{3/2}/3)$ for $x \to \infty$), it follows that the stochastic region $\beta_{\max} - \beta_{\min}$ is maximized for $P_\perp = 0$. Both $\beta_{\max}$ and $\beta_{\min}$ decrease with growth of $|P_\perp|$; however, the $\beta_{\min}$ boundary is much less sensitive to both P_x and P_y. From Eq. (2.23) we then conclude that $H_{\max}$ decreases with $|\mathbf{P}_\perp|$, while $H_{\min}$ remains intact. At large $|\mathbf{P}_\perp|$, it follows from Eq. (2.21) and Eq. (2.22) that stochasticity becomes completely suppressed, in agreement with the spectral analysis above.

Because $H_{\min}$ increases with P_y^2, stochastic energy is suppressed if its maximum $\max(\gamma_s)$ corresponds to $H_{\min} < 1$. However, if $\max(\gamma_s)$ corresponds to $H_{\max} > \mathcal{E}_p$, the efficiency of stochastic heating $\max(\gamma_s)/\mathcal{E}_p$ remains the same with increase of P_y. $H_{\max} > \mathcal{E}_p$
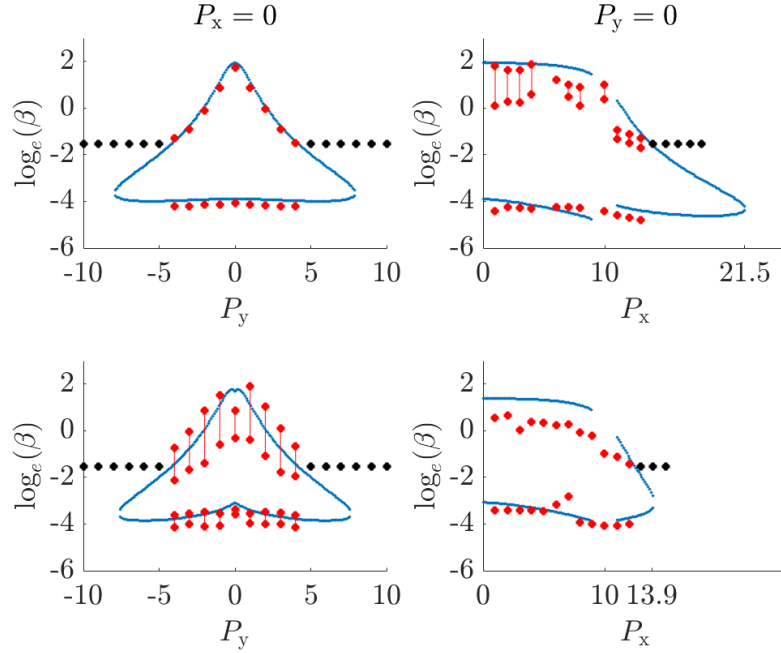
Figure 2.4. Stochastic boundary Eq. (2.21) and Eq. (2.22) for $K = 5$, plotted with blue lines for laser amplitudes $a_1 = 10$, $a_2 = 1$, in cases of parallel ($\alpha = 1$, top panels) and perpendicular ($\alpha = 0$, bottom panels) polarizations. Electrons have either $P_x = 0$ or $P_y = 0$ on the left and right panels, respectively. Red dots show the stochastic boundary from the series of Poincaré simulations with initial $\beta = (0.1)^{2/3}$, $\eta(0) = 0$, and with $k_2 = 9$ or 1089 (Using larger values of k_2 allows for a more precise measurement of β from the Poincare maps in some simulations, since the stochastic region is remains in $H > 1$). Black dots mark simulations with no stochasticity
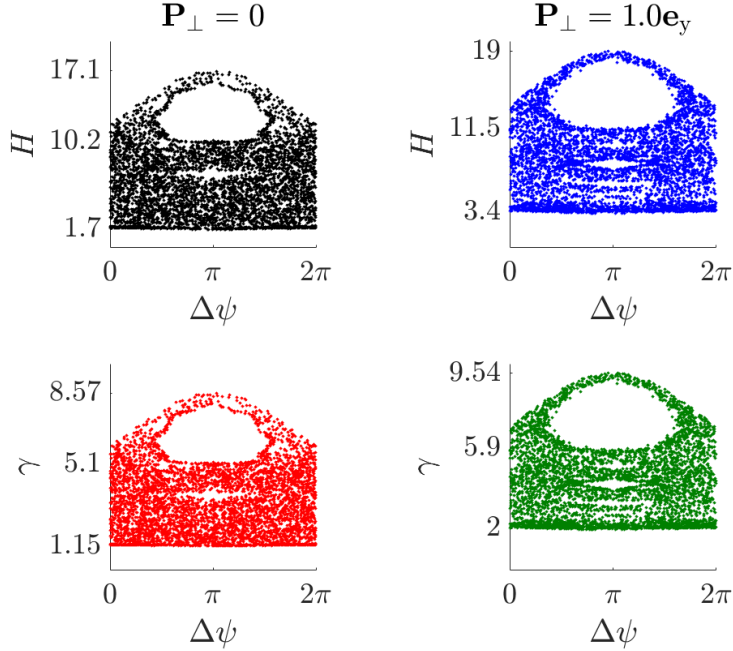
Figure 2.5. Poincaré cross-sections for $\alpha = 1$, $a_1 = 2$, $a_2 = 0.1$, $k_2 = 50$, $\mathbf{P}_\perp = 0$ (left panels), and $\mathbf{P}_\perp = 1.0\mathbf{e}_y$ (right panels). The corresponding ponderomotive energies $\gamma_p \approx 2.4$ ($\mathbf{P}_\perp = 0$) and 2.6 ($\mathbf{P}_\perp = 1.0\mathbf{e}_y$)

requires large, k_2,

$$k_2 > \left(1 + (P_x + A_x)^2 + (P_y + A_y)^2\right)a_1\beta_{\min}^{3/2}, \tag{2.24}$$

as in the simulation shown in Fig. (2.5).

The analysis above demonstrated that large $|\mathbf{P}_\perp| \gg a_1$ suppresses stochastic heating. For larger amplitudes of the main laser $\mathbf{a}_1$, the perpendicular canonical momentum will no longer be conserved due to radiation friction effects. To see how radiation friction (RF) effects affect the stochastic heating, we use the classical Landau & Lifshitz [23] approximation for RF force,

$$\begin{aligned}
\mathbf{f} = \rho_f\{ &-\gamma^2\mathbf{v}[(\mathbf{E} + \mathbf{v} \times \mathbf{B})^2 - (\mathbf{v} \cdot \mathbf{E})^2] + \\
&+ \gamma[(\partial_t + \mathbf{v} \cdot \nabla)\mathbf{E} + \mathbf{v} \times (\partial_t + \mathbf{v} \cdot \nabla)\mathbf{B}] + \\
&+ [\mathbf{E} \times \mathbf{B} + \mathbf{B} \times (\mathbf{B} \times \mathbf{v}) + \mathbf{E}(\mathbf{v} \cdot \mathbf{E})])\},
\end{aligned} \tag{2.25}$$

where $\mathbf{E} = -\partial_t \mathbf{a}_1$, $\mathbf{B} = \nabla \times \mathbf{a_1}$, $\rho_f = 2kr_e/3$, and $r_e = e^2/mc^2 \approx 2.8$ fm is the classical radius of electron. Estimating $\gamma \sim a_1^2$, $\mathbf{E} \sim a_1$, it follows from Eq. (2.25) that RF force is comparable to Lorentz force when $\rho_f a_1^5 \sim 1$. For lasers with a wavelength of about $0.5\ \mu m$, the $\rho_f a_1^5 \sim 1$ condition is satisfied for $a_1 \gtrsim 40$. Substituting $\mathbf{a}_1 = a_1 \sin(\eta)$ into Eq. (2.25) gives

$$
\begin{aligned}
\mathbf{f} = \rho_f \{ &a_1 H (1 - v_z) \sin(\eta) \mathbf{e}_x - \mathbf{v} a_1^2 H^2 \cos^2(\eta) \\
&+ a_1 H v_x \sin(\eta) \mathbf{e}_z + \\
&+ a_1^2 (1 - v_z) \cos^2(\eta) \mathbf{e}_z \},
\end{aligned}
\tag{2.26}
$$

that we combine with the equations of motion for the electron,

$$
\frac{d\mathbf{P}}{d\tau} = \frac{\gamma}{\chi} \mathbf{f}.
\tag{2.27}
$$

The $\mathbf{P}_\perp$ components of (2.27) are

$$
\frac{dP_x}{d\tau} = -\frac{\rho_f a_1^2 H^2}{\chi} \left([P_x + A_x] \cos^2(\eta) - \frac{\sin(\eta)}{a_1} \right),
\tag{2.28}
$$

$$
\frac{dP_y}{d\tau} = -\frac{\rho_f a_1^2 H^2}{\chi} [P_y + A_y] \cos^2(\eta),
\tag{2.29}
$$

where $A_{x,y}$ are components of $\mathbf{A} = \mathbf{a}_1 + \mathbf{a}_2$. Evolution of χ is described by

$$
\frac{d\chi}{d\tau} = \frac{\partial H}{\partial \eta} + \frac{\gamma}{\chi} (\mathbf{v} \cdot \mathbf{f} + f_z).
\tag{2.30}
$$

Using Eq. (2.26), expression Eq. (2.30) can be rewritten as

$$
\frac{d\chi}{d\tau} = \frac{\partial H}{\partial \eta} + \frac{H + \chi}{2\chi} \rho_f \left(a_1^2 \cos^2(\eta) [1 - v_z^2 - H^2 (v_z + \mathbf{v}^2)] + 2a_1 H v_x \sin(\eta) \right),
\tag{2.31}
$$

21

where the velocity components can be expressed as

$$v_{x,y} = \frac{2(P_{x,y} + A_{x,y})}{\chi + H}, \quad v_z = \frac{\chi - H}{\chi + H}. \tag{2.32}$$

Finally, equation (2.4) does not change in the presence of RF, since

$$\frac{d\eta}{d\tau} = \frac{1 - v_z}{1 + v_z} = \frac{\gamma - p_z}{\gamma + p_z} = \frac{H}{\chi} = -\frac{\partial H}{\partial \chi}. \tag{2.33}$$

It follows from Eq. (2.28) and Eq. (2.29) that $|P_\perp| > a_1$ converge to $P_x \sim a_1$ and $P_y \sim \sqrt{1 - \alpha^2} a_2$. For electrons with initial $P_\perp = 0$, the period of electron motion $T = 2\pi/\Omega \sim a_1^2$ and, since $\chi = \gamma + P_z \sim a_1^2$, from Eq. (2.28) follows that $P_x(T) \sim \rho_f a_1^3$. Since for lasers with micron wavelength $\rho_f \sim 10^{-8}$, it follows that P_x and P_y will remain zero for laser amplitudes $a_0 \ll 10^3$ consistent [24] with the classical approximation from [23] given by Eq. (2.25). Since $\rho_f H^2 \ll \Omega$ for $P_\perp \lesssim a_0$ values, dynamics described by Eqs. (2.28,2.29) are much slower than the characteristic period of electron motion (as illustrated in Fig. (2.6)), and so analysis of stochastic heating performed for taking $P_\perp$ constant remains valid.

2.2 Conclusion

In this chapter, we described stochastic heating of the electron with arbitrary canonical momentum $\mathbf{P}$ in the presence of two counter-propagating linear plane waves with an arbitrary angle between the polarization. We demonstrated that the onset of stochasticity is possible for both parallel and perpendicular polarization setups. For $a_2 \ll a_1$ case, we derived the stochasticity threshold and showed how the stochastic region of H decreases with the increase in perpendicular canonical momenta $\mathbf{P}_\perp$. We demonstrated that for $|\mathbf{P}_\perp| \ll a_1$, the Fourier spectrum of unperturbed $a_2 = 0$ electron motion has a long tail of harmonics with power law amplitude decay $|\hat{\chi}_{0,n}| \propto 1/n^2$, allowing for resonant
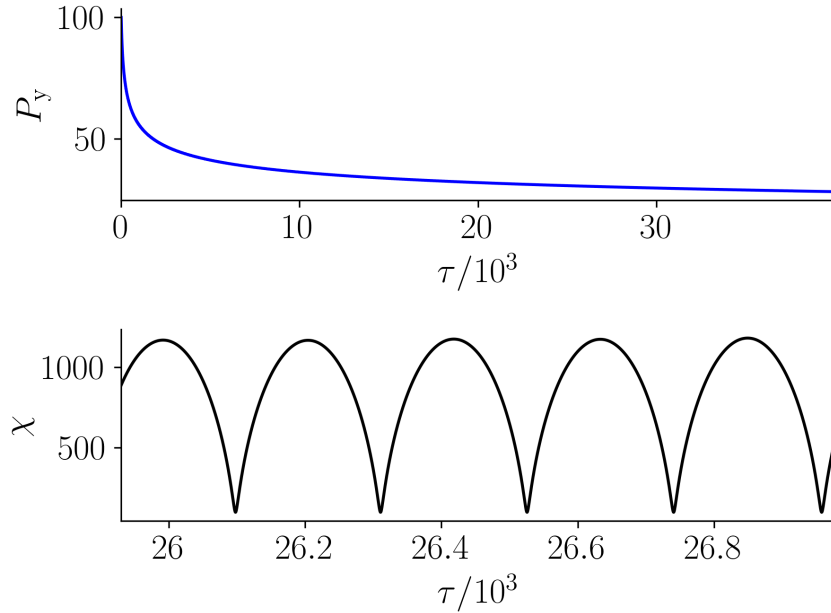
Figure 2.6. (Top panel) Decay of $P_\perp(\tau)$ and H caused by radiation friction for $\lambda = 1 \ \mu m$, $a_1 = 100$, and initial $\mathbf{P}_\perp = 100\mathbf{e_y}$. (Bottom panel) Corresponding evolution on $\chi(\tau)$

overlap and onset of stochasticity in agreement with Chirikov criterion. [13] Meanwhile, in $|\mathbf{P}_\perp| \gg a_1$ case, the exponential cut-off in Fourier spectrum $|\hat{\chi}_{0,n}| \propto \exp(-n)$ prevents the onset of stochasticity. Presented results reveal the physics behind the impact of $\mathbf{P}_\perp$ on the stochasticity boundary. Finally, we expanded the Hamiltonian analysis to include the impact of radiation friction in the classical radiation reaction limit. We demonstrated that within the applicability of classical approximation from [23], the impact of $P_\perp$ is much slower than the period of electron motion, and the Hamiltonian analysis $P_\perp = const$ for stochastic heating remains valid.

The presented results are useful for understanding electron dynamics in counter-propagating laser pulses such as, for example, the incident-reflected laser pulses in laser-target interactions [20, 21, 25].

The work presented in this chapter is a reprint of the material as it appears in *Stochastic electron motion in colliding plane waves* in Physical Review E 103, 063213

(2021), by A. R. Knyazev and S. I. Krasheninnikov. The dissertation author was the primary investigator and author of this paper.

Chapter 3

Laser-driven electron acceleration in nanoplate arrays targets

Interaction of high-intensity lasers with solid targets can result in a high yield of both x-ray and energetic electrons. To efficiently convert the energy of the incident laser into the energy of the radiated x-ray and emitted electrons, it is necessary that the target absorbs most of the incident laser energy. Multiple studies [26, 27] indicate that flat targets typically absorb less than 10% of the laser pulse energy, while structured targets can absorb over 90%. Laser interaction with different structured targets, such as "nanorod" arrays [27], "velvet" targets [28], "smoked" targets [29] and "foamed" targets [30] were studied experimentally and via computer simulations. However, the physics of the electron acceleration during the laser-target interaction is not yet completely described. It was shown [31] that the interaction of the micro-channel target with the laser creates the quasi-static electric fields in the cavities of the target. The presence of static electric and magnetic fields can lead to the stochastic acceleration of the electrons by the laser, as was demonstrated [32, 33, 34] with the Hamiltonian formalism.

In this chapter, we model the interaction of a laser with a periodic nanoplate array target. We show that quasi-static electric $\mathbf{E}_{qs}$ and magnetic $\mathbf{B}_{qs}$ fields can emerge in this setup, and develop a semi-analytic model for the formation of such fields. We use the 3/2-dimentional Hamiltonian [34] formalism to describe the motion of a single

electron in the presence of the laser and prescribed $\mathbf{E}_{qs}$ and magnetic $\mathbf{B}_{qs}$ fields. From the single electron model, we find the condition for the onset of stochastic electron heating. We also determine when the maximum electron energy $\mathcal{E}_{max}$ from stochastic heating exceeds ponderomotive energy scaling [35]. We verify our analytic results with a series of 2-dimensional Particle-In-Cell (2D PIC) simulations. The maximum electron energy in our PIC simulations can be explained with the proposed stochastic acceleration mechanism.

The rest of the chapter is organized as follows. In Section 3.1 we describe the simulation setup. Extraction of the electrons from the target by the laser pulse and formation of the quasi-static electromagnetic fields are analyzed in Section 3.2. In Section 3.3 we examine the acceleration of electrons in the laser and quasi-static fields. The results of PIC simulations are presented in Section 3.4. Section 3.5 is the conclusion.

3.1 Setup Description

Laser-target interaction experiments typically involve complex, often irregular structures. Direct simulation of such structures requires a 3D consideration [30, 36, 37], which poses significant computational challenges. Modeling complex structures can also make it hard to pinpoint important physics mechanisms. In this work, we consider a simplified 2D model of a nanoplate target as shown in Fig. 3.1. We model the target by filling a region of the simulation domain with a cold plasma, as shown with black color in Fig. 3.1. The nanoplates of the target are modeled as rectangular regions with a length of sides $d = 0.1\lambda$ along $\mathbf{e}_y$, and $L = 20\lambda$ along $\mathbf{e}_z$, where $\lambda = 400$ nm is the wavelength of the incident laser pulse propagating along $\mathbf{e}_z$. The backplate of the target is modeled as a slab of size $L_{bp} = \lambda$ along $\mathbf{e}_z$. The gaps between neighboring nanoplates are all equal to D, with different values of D from 0.25λ to 12λ considered in our series of PIC simulations. The material of a target is modeled by a cold plasma, composed of immobile ions pre-ionized to an arbitrarily chosen value $Z = 5$, and the electrons. The number density of the electrons
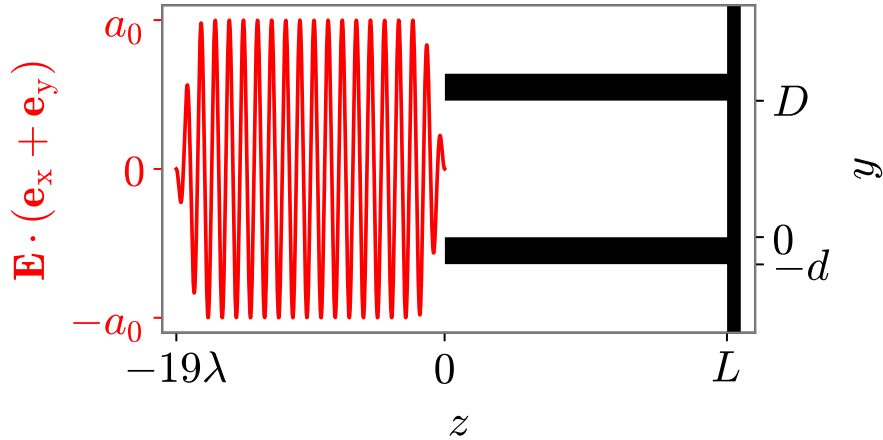
Figure 3.1. Schematic view of the simulation setup. The black region corresponds to where the target is located in the domain. The nanoplates are separated by vacuum gaps of width D. Each nanoplate has the width d along y-axis and length L along z-axis. Nanoplates are connected on the right side at $z = L$ with the bulk of width λ. The top and bottom boundaries of the simulation domain are periodic, left and right boundaries are open. The laser pulse arrives from the left boundary. The electric field of the laser at time $t = 0$ is shown by the red curve at z between -19λ and 0.

is set to $n_e = 50 n_{cr}$, where $n_{cr} = m\omega^2/4\pi e^2 = 6.97 \times 10^{21}$ cm^{-3} is critical plasma density, m is the electron mass, e is the electron charge, and $\omega = 2\pi c/\lambda$ is the laser frequency. The number density of ions is set to $n_i = n_e/Z \approx 6 \times 10^{22}$ cm^{-3}, which is similar to the number density of ions in solid copper.

The laser consists of a 2λ long ramp-up, followed by a 15λ long main pulse and a 2λ decay, as shown in Fig. 3.1. The main pulse is described by a vector potential $\mathbf{a}$ of magnitude $a = -a_0 \cos(\xi)$, where $a_0 = eE/mc\omega$ is the normalized vector potential, $\xi = \omega(t - z/c)$, c is the speed of light in vacuum. We considered two laser polarizations, described by $\mathbf{a} = a\mathbf{e}_x$ (x-polarized) and $\mathbf{a} = a\mathbf{e}_y$ (y-polarized). The value of a_0 ranged from 1.0 to 4.0, corresponding to laser intensities from 1.8×10^{19} W/cm^2 to 1×10^{20} W/cm^2. We choose the frame of reference so that the laser ramp-up reaches the nanoplates at $z = 0$ at the time $t = 0$, as shown in Fig. 3.1.

We conduct our particle-in-cell simulations with the fully relativistic 2D3V PIC

code EPOCH [38]. The simulation domain has the size of $2d + 2D$ along the y-axis, and $31\lambda + L$ along the z-axis. Each cell has a size of 0.01λ along both y and z axes. Boundaries normal to the y-axis are periodic for both particles and fields. Boundaries normal to the z-axis are open for both particles and fields.

The rest of this chapter uses normalized units marked with a hat. Distances are normalized by $\lambda/2\pi$. Velocities of electrons are normalized by the speed of light c. Number densities are normalized by n_{cr}. Time is normalized by $1/\omega$. The momentum of electrons is normalized by mc. The magnitudes of the electric and magnetic fields are normalized by $mc\omega/e$. Potentials of electric and magnetic fields are normalized by mc^2/e. Electric currents are normalized by $en_{\mathrm{cr}}c$.

3.1.1 Role of the laser polarization

Polarization of the laser pulse significantly affects the laser-target interaction. In the rest of this section, we will show that the y-polarized pulse can propagate into the gap of any size $\hat{D}$, while the x-polarized pulse is reflected if $\hat{D} < \pi$. Furthermore, as will be discussed in Section 3.2, only the y-polarized pulse creates the quasi-static fields inside the gap.

Because of the high conductivity of nanoplates, we can approximate them as ideal conductor and explain the difference between x and y polarization of laser with a simple model of a lossless multi-connected waveguide. Specifically, consider the waveguide formed by two parallel, ideally conducting plates located at $\hat{y} = 0$ and $\hat{y} = \hat{D}$. Such waveguide has three types [39] of $\mathbf{E}, \mathbf{B} \propto \exp\left(i(\hat{t} - \hat{z})\right)$ modes: purely transverse (TEM) modes, modes with longitudinal components of the electric field (TM modes), and modes with longitudinal components of the magnetic field (TE modes). Due to $E_{\mathrm{x}} = 0$ boundary conditions, TEM modes in such a waveguide can only be polarized along $\mathbf{e}_{\mathrm{y}}$, and have the same electric and magnetic fields as a plane wave. Furthermore, TEM modes can propagate in a gap of any size $\hat{D}$, and have luminal phase velocity. The electric field

of such TEM mode is normal to the waveguide boundary, and therefore it can extract electrons from the boundary by the electric force.

Meanwhile, the only x-polarized modes in the aforementioned waveguide are TE modes. Dispersion relation for TE modes suggests $\omega \geq c\pi/D$, therefore TE modes can only propagate in a gap $\hat{D} > \pi$. As a crude model for the propagation of the x-polarized pulse inside the gap, one can Fourier expand the plane wave at the gap entrance $|\mathbf{E}| = |E(y, z = 0)\mathbf{e}_x| = \tilde{E}_x = const$ into a sum of TE modes. The resulting expansion of $\tilde{E}_x$ gives $E_{TE} = \alpha_l E_{x,l}$, where

$$\alpha_l = \frac{2\tilde{E}_x(1 - \cos(\pi l))}{\pi l}, \ E_{x,l} \propto \sin\left(\pi l \frac{y}{D}\right), \tag{3.1}$$

l is an integer. The expression for the z-component of magnetic field B_{TE} is $B_{TE} = \alpha_l B_{z,l}$, where $B_{z,l}$ is the z-component of magnetic field of the TE mode with electric field $E_{x,l}\mathbf{e}_x$.

Electrons subjected to $E_{TE}\mathbf{e}_x$ and $B_{TE}\mathbf{e}_z$ experience the ponderomotive force pushing the electrons from the gap into the plasma, where there is no laser field and therefore no efficient electron acceleration. Since this chapter focuses on laser-driven electron acceleration, in the rest of the chapter we will primarily study the y-polarization case.

3.2 Electron extraction and formation of quasi-static electromagnetic field

As the y-polarized pulse propagates between the nanoplates, it extracts some of the electrons from them. The extracted electrons can then either return to their parent nanoplate or stream away from it, depending on the laser phase. The counter-propagating bunches of streaming electrons with laser phase difference of π, extracted from the opposite boundaries of the gap between nanoplates, eventually pass through each other, mix up and form an approximately homogeneous electron density $\bar{n}$ in the gap.

To have some understanding of the extraction process, we consider the following model. We consider the electron located at the boundary between the nanoplate and the gap. We also assume that the field acting on this electron is the same as the field of a plane wave, propagating along the surface of the nanoplate. Specifically, we consider a motion of a single electron in the plane wave described by a vector potential $-a_0 \cos(\xi + \xi_0)\mathbf{e_y}$, where ξ_0 is the phase of the plane wave at the moment of electron extraction. The electron is assumed to be initially immobile. The motion of an initially immobile electron in a plane EM wave has three well-known integrals of motion:

$$\hat{p}_x = 0, \ \hat{p}_y + a_0 \cos(\xi + \xi_0) = a_0 \cos(\xi_0), \ \gamma - \hat{p}_z = 1, \qquad (3.2)$$

where $\gamma^2 = 1 + \hat{\mathbf{p}}^2$. Without loss of generality, we set the y-coordinate of the nanoplate surface from which the electron is extracted to $\hat{y}_0 = 0$. From Eqs. (3.2), it follows that

$$\frac{d\hat{y}}{d\xi} = a_0 \big(\cos(\xi_0) - \cos(\xi + \xi_0) \big). \qquad (3.3)$$

Equation (3.3) shows that only specific values of the initial phase ξ_0 lead to the extraction of the electron into the gap. Indeed, if the gap is in the $\hat{y} < 0$ region, the electron is only extracted if $\sin(\xi_0) > 0$. Likewise, for the gap in $\hat{y} > 0$ region, the electron is extracted if $\sin(\xi_0) < 0$. From Eqs. (3.2) we can derive the equations for the electron's trajectory,

$$\hat{y} = a_0 \big(\xi \cos(\xi_0) + \sin(\xi_0) - \sin(\xi + \xi_0) \big), \qquad (3.4)$$

$$\hat{z} - \hat{z}_0 = \frac{a_0^2}{2} \Big[\xi \big(1 + \frac{1}{2} \cos(2\xi_0) \big) + \frac{1}{4} \sin \big(2(\xi + \xi_0) \big) $$
$$- \sin(\xi) - \sin(\xi + 2\xi_0) \Big], \qquad (3.5)$$

where $\hat{z}_0$ is the z-coordinate of the electron before the extraction. From Eq. (3.4) we conclude that depending on the phase ξ_0, the extracted electron may either return to its

parent nanoplate or stream away from it. The electron bunches that stream along y-axis have a phase difference of $\Delta\xi = \pi$ with the electron bunches that stream in the opposite direction. From Eqs. (3.4) and (3.5), we can estimate the maximum angle θ between the radius vector of the electron and the $y = 0$ boundary as

$$\lim_{\xi \to \infty} \frac{\hat{y}(\xi)}{\hat{z}(\xi) - \hat{z}_0} = \frac{4\cos(\xi_0)}{a_0(2 + \cos(2\xi_0))} < \frac{\sqrt{2}}{a_0} = \tan(\theta). \tag{3.6}$$

The estimate given by Eq. (3.6) neglects the effect of the Coulomb forces between the extracted electrons and the parent nanoplate, and therefore is only accurate for extracted electrons with small $\hat{y}$. As extracted electrons move away from the parent nanoplate, the value of streaming angle θ becomes less than predicted by Eq. (3.6).

As bunches of the electrons propagate away from their parent nanoplates along the y-axis, they eventually meet a counter-propagating bunch of electrons. From Eq. (3.6), we conclude that the length $\hat{L}$ of the gap needs to be at least $\hat{L} > a_0\hat{D}/\sqrt{2}$ for the first extracted bunches of electrons to start mixing with the counter-propagating bunches. When the mixing occurs, mixed electron bunches form the homogeneous electron density $\bar{n}$ inside the gap. The charge density inside the gap creates the electric field $\mathbf{E}_{qs}$. The current of the extracted electrons in the gap $\hat{j} = \hat{\bar{n}}\hat{v}_z$ creates the magnetic field $\mathbf{B}_{qs}$. Velocity $\hat{v}_z$ can be estimated from Eqs. (3.2) as

$$\hat{v}_z = \frac{\hat{p}_y^2}{2 + \hat{p}_y^2} \sim \frac{a_0^2}{2 + a_0^2}. \tag{3.7}$$

Since $\hat{v}_z < 1$, the magnitude of the magnetic field B_{qs} is weaker than the magnitude of the electric field E_{qs}. In Section 3.3 we will show that the difference between E_{qs} and B_{qs} is important for the onset of stochastic electron acceleration.

Assuming that electron extraction stops when the electric field $\mathbf{E}_{qs}$ from the electrons in the gap compensates the electric field of the laser pulse at the boundary, the density of

the electrons $\hat{\hat{n}}$ after mixing can be estimated as

$$\hat{\hat{n}} = \frac{2a_0}{\hat{D}}.$$ (3.8)

The analysis above assumes ions are immobile. Mobile ions will expand into the $\hat{D}$ gap when subjected to $\mathbf{E}_{qs}$ field, closing the gaps between nanoplates. For non-relativistic ion motion, the time τ_i to cross the gap $\hat{D}$ is $\tau_i \sim \sqrt{2\hat{D}\hat{m}_i/Za_0}$, where $\hat{m}_i$ is the ion mass in units of electron mass. Therefore, our immobile ion analysis with the y-polarized pulse will only be applicable during times shorter than $\hat{\tau}_i$. For the copper target with parameters from Section 3.1, $\hat{\tau}_i > 100$ and the immobile ions assumption holds. In our PIC simulations with y-polarized laser, the time it takes for the laser pulse to reach the back wall is less than τ_i, and hence the immobile ions assumption applies. For larger $a_0 \sim 100$, the motion of ions can no longer be neglected for practical $\hat{D} \sim 10$ gap sizes.

Concluding this section, we note the differences of the quasi-static electric and magnetic fields in the gap from the quasi-static fields in another laser-plasma interaction setup, the evacuated ion channel [40]. As a matter of fact, the quasi-static electric and magnetic fields in the gap can be called "electron" channel, where $\mathbf{E}_{qs} \times \mathbf{B}_{qs}$ is along the direction of laser propagation. Whereas, in the ion channel, the $\mathbf{E}_{qs} \times \mathbf{B}_{qs}$ is directed against laser propagation.

3.3 Stochastic acceleration

In this section, we examine the electron acceleration in laser and quasi-static fields. Based on the results from Section 3.2, fields $\hat{\mathbf{E}}_{qs}$ and $\hat{\mathbf{B}}_{qs}$ between two neighbor nanoplates can be described with scalar $\hat{U}(\hat{y})$ and vector $\hat{A}_B(\hat{y})$ potentials as $\hat{\mathbf{E}}_{qs} = \nabla \hat{U}(\hat{y})$

and $\hat{\mathbf{B}}_{\mathrm{qs}} = -\nabla \times (\hat{A}_\mathrm{B}\mathbf{e}_\mathrm{z})$, where

$$\hat{U}(\hat{y}) = \frac{\kappa_U}{2}\left(\frac{\hat{D}^2}{4} - \left(\hat{y} - \frac{\hat{D}}{2}\right)^2\right), \tag{3.9}$$

$$\hat{A}_\mathrm{B}(\hat{y}) = \frac{\kappa_\mathrm{B}}{2}\left(\frac{\hat{D}^2}{4} - \left(\hat{y} - \frac{\hat{D}}{2}\right)^2\right), \tag{3.10}$$

$\kappa_U = \hat{\tilde{n}}$ and $\kappa_\mathrm{B} = \kappa_U \hat{v}_\mathrm{z}$. The signs of $\hat{U}$ and $\hat{A}_\mathrm{B}$ defined in (3.9) and (3.10) are chosen to be positive, opposite to the conventional electrostatic and vector potential. In the rest of the section, we will neglect the size of each nanoplate $\hat{d} = 0$, so the structure of $\hat{\mathbf{E}}_{\mathrm{qs}}$ and $\hat{\mathbf{B}}_{\mathrm{qs}}$ fields in the target is described by a chain of $\hat{U}(\hat{y})$ and $A_\mathrm{B}(\hat{y})\mathbf{e}_\mathrm{z}$ potentials defined in (3.9) and (3.10). The motion of a single electron in the presence of $\hat{\mathbf{E}}_{\mathrm{qs}}$ and $\hat{\mathbf{B}}_{\mathrm{qs}}$ fields and the laser wave with vector potential $\mathbf{a} = -a_0\cos(\xi)\mathbf{e}_\mathrm{y}$, is described by a 3/2-dimentional Hamiltonian [33] as

$$\frac{d\hat{P}_\mathrm{y}}{d\xi} = -\frac{\partial\hat{H}}{\partial\hat{y}}, \ \frac{d\hat{y}}{d\xi} = \frac{\partial\hat{H}}{\partial\hat{P}_\mathrm{y}}, \tag{3.11}$$

$$\hat{H} = \frac{1}{2}\left\{\frac{1 + \left[\hat{P}_\mathrm{y} - a_0\cos(\xi)\right]^2}{C - W^{(-)}(\hat{y})} + W^{(+)}(\hat{y}) + C\right\}, \tag{3.12}$$

$$W^{(\pm)}(\hat{y}) = \hat{U}(\hat{y}) \pm \hat{A}_\mathrm{B}(\hat{y}), \tag{3.13}$$

$$C = \gamma + W^{(-)}(\hat{y}) - \hat{p}_\mathrm{z} = const. \tag{3.14}$$

where $\hat{P}_\mathrm{y} = \hat{p}_\mathrm{y} + a_0\cos(\xi)$ is the canonical momentum, and $\hat{p}_\mathrm{x} = const$ is set as zero. The Hamiltonian (3.12) is equal to the total electron energy $\hat{H} = \gamma + \hat{U}$. Without the laser $a_0 = 0$, the energy is conserved $\hat{H} = const$ and the corresponding unperturbed electron motion is periodic with some frequency $\hat{\Omega}$. To heat the electron efficiently, the laser pulse has to resonate with the harmonics of unperturbed electron, motion [13] which is only

possible for $\hat{\Omega} < 1$. For $\hat{\Omega} < 1$, the resonances of laser with harmonics of electron motion can occur, and overlap of such resonances enables stochastic acceleration.

Stochastic electron motion can be imagined as a series of "kicks" separated by adiabatic motion. These kicks can lead to stochasticity [34] if

$$K \approx \left| \frac{\partial \hat{T}_e}{\partial \hat{H}} \Delta \hat{H} \right| \gtrsim 1, \tag{3.15}$$

where $\hat{T}_e = 2\pi/\hat{\Omega}$ and $\Delta \hat{H}$ are, respectively, the time and change of electron Hamiltonian between two consecutive kicks. In this section, we will use condition (3.15) to estimate the maximum energy of the stochastic electron motion.

Since we are interested in energetic electrons, we consider

$$\hat{H} \gg \max\left(1, C, W_{\max}^{(+)} = \frac{\kappa_U + \kappa_B}{8} \hat{D}^2\right). \tag{3.16}$$

Using Eq. (3.8), we estimate $W_{\max}^{(+)} \sim a_0 \hat{D}/2$. Under assumption (3.16), the Hamiltonian (3.12) can be approximated as

$$\hat{H} \approx \frac{1}{2} \left\{ \frac{1 + \left[\hat{P}_y - a_0 \cos(\xi)\right]^2}{C - W^{(-)}(\hat{y})} \right\}. \tag{3.17}$$

Unperturbed trajectories described by (3.17) are shown in Fig. 3.2. These unperturbed trajectories are bounded if $C < 1/2\hat{H} + W_{\max}^{(-)}$, where $W_{\max}^{(-)} = (\kappa_U - \kappa_B)\hat{D}^2/8$, and unbounded otherwise.

To examine the unperturbed motion frequency $\hat{\Omega}$ of bounded and passing electrons, we use action-angle variables $(\mathcal{I}, \vartheta)$. Let $\ae = ((2\hat{H})^{-1} + W_{\max}^{(-)} - C)/W_{\max}^{(-)}$ characterize the distance from the electron's trajectory to the separatrix, in the range from $-\infty$ to 1. Indeed, $\ae{=}0$ corresponds to the separatrix, $\ae{>} 0$ is bounded motion, $\ae{=}1$ is the equilibrium point at $\hat{y} = 0$, $\hat{P}_y = 0$, and negative $\ae$ corresponds to passing trajectories.

34
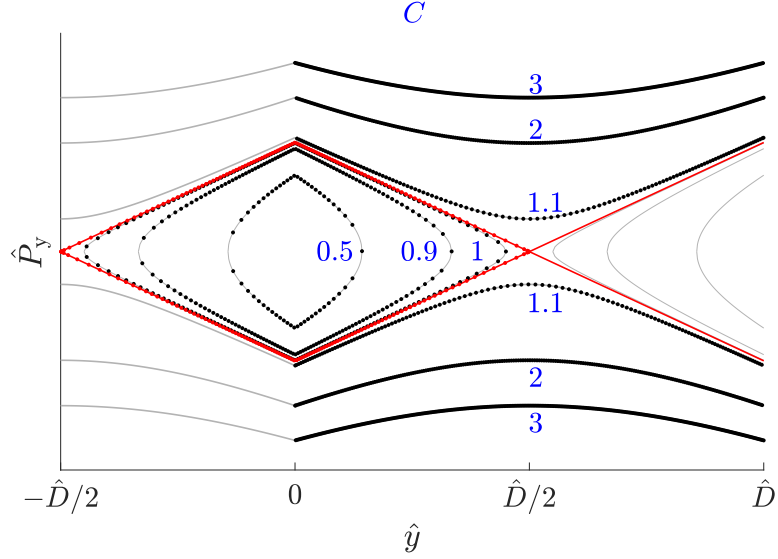
Figure 3.2. Unperturbed trajectories of energetic electrons (3.17) for $\hat{H} = 50$, $W_{\text{max}}^{(-)} = 1$, and various values of C. Red lines that cross at $\hat{D}/2$ show trajectory with $C = 1/2\hat{H} + W_{\text{max}}^{(-)} = 1.01$, separating bounded and unbounded trajectories. Dots show the stroboscopic portrait of the motion.

For bounded motion, $2\pi\mathcal{I} = \oint \hat{P}_{\text{y}} d\hat{y}$, and for the passing electrons $2\pi\mathcal{I} = \int_{\hat{y}}^{\hat{y}+\hat{D}} \hat{P}_{\text{y}} d\hat{y}$. The frequency is calculated as $\hat{\Omega} = (d\mathcal{I}/d\hat{H})^{-1}$, and the resulting $\hat{\Omega}(æ)$ dependence is shown in Fig. 3.3. As æ goes to zero, the frequency $\hat{\Omega}$ also goes to zero. Transformation to canonical variables allows determining how $\hat{\Omega}$ depends on $W_{\text{max}}^{(-)}$, $\hat{D}$, and particle energy $\hat{H}$. We will get this dependencies in an easier way later in this section. We will now determine the maximum stochastic energies for the cases when unperturbed electron motion is unbounded $C \gg W_{\text{max}}^{(-)}$, close to separatrix $C \sim W_{\text{max}}^{(-)}$, and bounded $C \ll W_{\text{max}}^{(-)}$.

For $C \gg W_{\text{max}}^{(-)}$ case, Hamiltonian (3.17) can be approximated as

$$\hat{H} \approx \hat{H}_1 = \frac{1}{2} \left\{ \frac{1 + \left[\hat{P}_{\text{y}} - a_0 \cos(\xi) \right]^2}{C} \right\}, \tag{3.18}$$

35
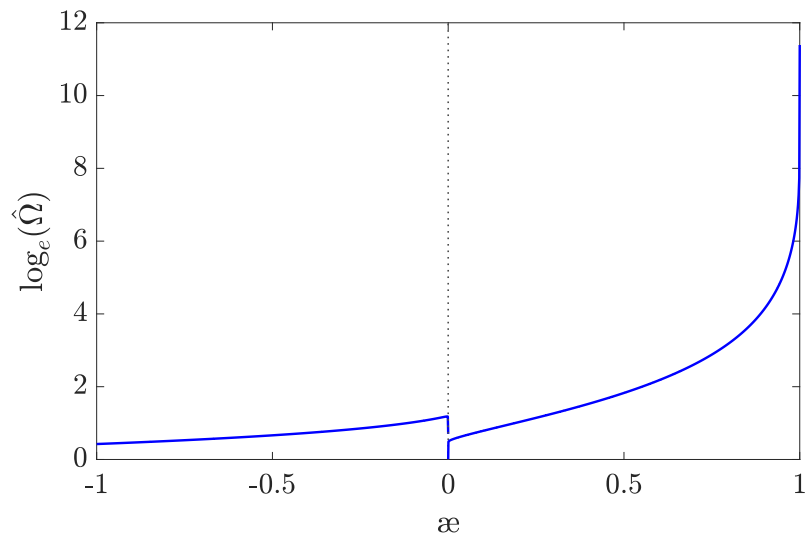
Figure 3.3. Frequency $\hat{\Omega} = (d\hat{H}/d\mathcal{I})$ of unperturbed electron motion (3.17) for $\hat{H} = 50$, $W_{\max}^{(-)} = 2$, $\hat{D} = 8\pi$ and various æ values. The bifurcation at æ=0 corresponds to the separatrix, where $\hat{\Omega} = 0$.

which is equivalent to the Hamiltonian (3.12) for the ponderomotive acceleration case $\hat{A}_{\mathrm{B}} = \hat{U} = 0$. Hamiltonian (3.18) corresponds to a linear equation of motion, meaning that no stochasticity is possible. Another way to see that the system with Hamiltonian (3.18) has no stochasticity is to note that the spectra of the oscillations described by Hamiltonian (3.18) consists of a single harmonic, and therefore a Chirikov's resonance overlap criterion can not be satisfied. Ponderomotive acceleration $\hat{\mathcal{E}}_{\mathrm{pond}} = a_0^2/C$ described by Hamiltonian (3.18) is only efficient for the small dephasing rate $\gamma - \hat{p}_{\mathrm{z}} \ll 1$. But if the dephasing rate is small, then from (3.14) we conclude that $C \sim W^{(-)}(\hat{y})$, which contradicts the $C \gg W_{\mathrm{max}}^{(-)}$ condition. Therefore, in $C \gg W_{\mathrm{max}}^{(-)}$ case no stochastic acceleration occurs, and the electron acceleration is inefficient.

For $C \approx W_{\mathrm{max}}^{(-)}$, Eq. (3.17) illustrates that the resonant points are $|\hat{y}| \approx \hat{D}/2$. It is convenient to rewrite Eq. (3.17) as

$$\frac{4W_{\mathrm{max}}^{(-)}}{\hat{D}^2}\left(\hat{y} - \frac{\hat{D}}{2}\right)^2 - \frac{\hat{P}_y^2}{2\hat{H}_2} \approx W_{\mathrm{max}}^{(-)} - C. \tag{3.19}$$

Therefore, for $C \approx W_{\mathrm{max}}^{(-)}$, Eq. (3.19) describes two lines, one of which is

$$\hat{P}_y = \frac{\sqrt{8\hat{H}_2 C}}{\hat{D}}\left(\hat{y} - \frac{\hat{D}}{2}\right). \tag{3.20}$$

From Eqs. (3.11) and (3.20) we get the equation of unperturbed electron motion

$$\sqrt{\frac{C}{2\hat{H}_2}}\frac{1}{\hat{D}}\left(\hat{y} - \frac{\hat{D}}{2}\right)^2 = \xi - \xi_{\mathrm{max}}, \tag{3.21}$$

where ξ_{max} is when the electron is at $\hat{y} = \hat{D}/2$. For C slightly less than $W_{\mathrm{max}}^{(-)}$, the electron trajectory is bounded, and it takes a quarter of the period $\hat{T}_2$ of the electron's motion to

go from $\hat{y} = 0$ to $\hat{y} = \hat{D}/2$. We can estimate $\hat{T}_2$ as

$$\hat{T}_2 = \sqrt{\frac{C}{2\hat{H}_2}}\hat{D} \propto \frac{\zeta\hat{\mathcal{E}}_{\text{pond}}^{1/2}}{\hat{H}_2^{1/2}}, \tag{3.22}$$

and hence the frequency of motion is $\hat{\Omega}_2 \sim \hat{D}\sqrt{\hat{H}_2/C}$. Stochastic heating requires overlapping of high harmonics resonance and thus $\hat{\Omega}_2 \ll 1$. Therefore, the maximum energy scaling we should expect is $\hat{H}_2 < C\hat{D}^2$ ($\hat{\Omega}_2 \approx 1$). If it exceeds the ponderomotive scaling $\hat{\mathcal{E}}_{\text{pond}}$, we have

$$\frac{a_0^2}{C} \leq C\hat{D}^2 \Leftrightarrow \zeta \equiv \frac{\hat{D}C}{a_0} > 1. \tag{3.23}$$

We can use Eqs. (3.11) and (3.20) to estimate change $\Delta\hat{H}_2$ of electron's energy during $\hat{T}_2$ in presence of the laser as

$$\Delta\hat{H}_2 = \int \frac{\partial\hat{H}_2}{\partial\xi}\frac{d\xi}{d\hat{y}}d\hat{y} \propto (\hat{H}_2\zeta^2\hat{\mathcal{E}}_{\text{pond}}^3)^{1/4}. \tag{3.24}$$

Therefore, the maximum energy of stochastic motion is determined by

$$K = \left|\frac{\partial\hat{T}_2}{\partial\hat{H}_2}\Delta\hat{H}_2\right| \sim \zeta^{3/2}\left(\frac{\hat{\mathcal{E}}_{\text{pond}}}{\max(\hat{H}_2)}\right)^{5/4} = 1, \tag{3.25}$$

where we used estimates (3.22) and (3.24). From Eq. (3.25) we determine the scaling of $\max(\hat{H}_2)$ to be

$$\max(\hat{H}_2) \propto \hat{\mathcal{E}}_{\text{pond}}\zeta^{6/5}. \tag{3.26}$$

For $C \ll W_{\max}^{(-)}$, from Eq. (3.12) we know that the electron motion is bound to $\hat{y} \ll \hat{D}$, so we can approximate Hamiltonian (3.17) as

$$\hat{H}_3 = \frac{1}{2C}\left\{\frac{1 + \left[\hat{P}_{\text{y}} - a_0\cos(\xi)\right]^2}{1 - \alpha|\hat{y}|}\right\}, \tag{3.27}$$

where $\alpha = 4W_{\max}^{(-)}/C\hat{D}$. It follows that the resonant points are $|\hat{y}| \approx 1/\alpha$. For Hamiltonian (3.27) we find the equation of unperturbed electron motion from (3.11) to be

$$\sqrt{\frac{2C}{\hat{H}_3}}\frac{2}{3\alpha}\left(1 - \alpha|\hat{y}|\right)^{3/2} = \xi - \xi_{\max}, \tag{3.28}$$

where $\xi_{\max}$ is when the electron is at $\max(|\hat{y}|) = 1/\alpha$. It takes a quarter of the period for the electron to go from $\hat{y} = 0$ to $\hat{y} = 1/\alpha$, and we can use that to estimate the period $\hat{T}_3$ from Eq. (3.28) to be

$$\hat{T}_3 \propto \frac{\zeta\hat{\mathcal{E}}_{\text{pond}}^{1/2}C}{\hat{H}_3^{1/2}W_{\max}^{(-)}}. \tag{3.29}$$

Based on Eq. (3.29), the resonance overlap condition $\hat{\Omega}_3 < 1$ for the stochastic heating sets a limit on the energy of stochastic motion $\hat{H}_3 < \hat{D}^2 C^3/W_{\max}^{(-)}$, which exceeds $\hat{\mathcal{E}}_{\text{pond}}$ if $\zeta > W_{\max}^{(-)}/C$. This condition can be easily satisfied since $W_{\max}^{(-)} \ll C$. We can use Eqs. (3.11) and (3.27) to estimate the energy change $\Delta\hat{H}_3$ during one oscillation of the electron in the presence of the laser,

$$\Delta\hat{H}_3 = \int_{\hat{y}_{\max}}^{\hat{y}} \frac{\partial\hat{H}_3}{\partial\xi}\frac{d\xi}{d\hat{y}}d\hat{y} \propto \left(\frac{\hat{H}_3\zeta\hat{\mathcal{E}}_{\text{pond}}^2 C}{W_{\max}^{(-)}}\right)^{1/3}, \tag{3.30}$$

where we assumed that $\hat{H}_3 \gg \Delta\hat{H}_3 \gg \hat{\mathcal{E}}_{\text{pond}}$. The scaling of maximum energy of stochastic motion for $C \ll W_{\max}^{(-)}$ can be estimated from

$$K \approx \left|\frac{\partial\hat{T}_3}{\partial\hat{H}_3}\Delta\hat{H}_3\right| \sim \left(\frac{\hat{\mathcal{E}}_{\text{pond}}}{\max(\hat{H}_3)}\right)^{7/6}\left(\frac{\zeta C}{W_{\max}^{(-)}}\right)^{4/3} = 1 \tag{3.31}$$

to be

$$\max(\hat{H}_3) \propto \hat{\mathcal{E}}_{\text{pond}}\left(\frac{\zeta C}{W_{\max}^{(-)}}\right)^{8/7}, \tag{3.32}$$

where we used estimates (3.29) and (3.30).

We now determine what C corresponds to the largest stochastic energy for given

a_0 and $\hat{D}$ parameters. Using estimates (3.7) and (3.8), we express $W_{\text{max}}^{(-)}$ as

$$W_{\text{max}}^{(-)} = \frac{\kappa_U - \kappa_B}{8} \hat{D}^2 = \frac{a_0 \hat{D}}{2(2 + a_0^2)}. \tag{3.33}$$

Combining estimate (3.33) with energy limits (3.26) and (3.32) gives

$$\max(\hat{H}_2) \propto \frac{a_0 \hat{D}^{7/5}}{(2 + a_0^2)^{1/5}}, \tag{3.34}$$

$$\max(\hat{H}_3) \propto \frac{(2 + a_0^2)^{8/7} C^{9/7}}{a_0^{2/7}} \ll \frac{a_0 \hat{D}^{9/7}}{(2 + a_0^2)^{10/7}}. \tag{3.35}$$

Analysis above neglects the following aspects of the laser-target interaction. The length $\hat{L}$ of the gaps was assumed infinite, meanwhile in practice the value of $\hat{L}$ may be insufficient to both establish $\hat{\mathbf{E}}_{\text{qs}}$ and $\hat{\mathbf{B}}_{\text{qs}}$ and let the electrons reach maximum energy. Analysis neglects the energy balance between the laser and the plasma, meanwhile in reality the laser will decay and hence $a_0 = a_0(\hat{z})$. For the laser with vector potential $-a_0(\hat{z})\cos(\xi)$, C may no longer be a constant of motion, and associated change in ζ affects the energy scaling. Note that we also neglected the nanoplate size $\hat{d}$. Since the laser field is absent inside the nanoplate, nonzero $\hat{d}$ means that when an electron escapes into the nanoplate at some ξ_{in}, it leaves the nanoplate at $\xi_{\text{out}} \neq \xi_{\text{in}}$. This $\xi_{\text{out}} - \xi_{\text{in}}$ jump changes the value of C, and associated change in ζ affects the energy scaling. Analysis also neglected radiation and collision stopping power that occurs when the electron is passing though the nanoplates. Such dissipative effects become important if they cause electrons to lose a significant part $\delta\gamma \sim \gamma$ of their kinetic energy γ. Based on the stopping power data for electrons in solid copper, reported by National Institute of Standards and Technology (NIST) [41], the estimated electron energy loss is negligible $\delta\gamma \ll \gamma$ for our target's parameters, for kinetic energies $\gamma \lesssim 10^3$, as shown in the Fig. 3.4.

In Section 3.4 we will show that despite the mentioned neglected aspects, the analysis of stochastic electron motion can explain the generation of high-energy electrons
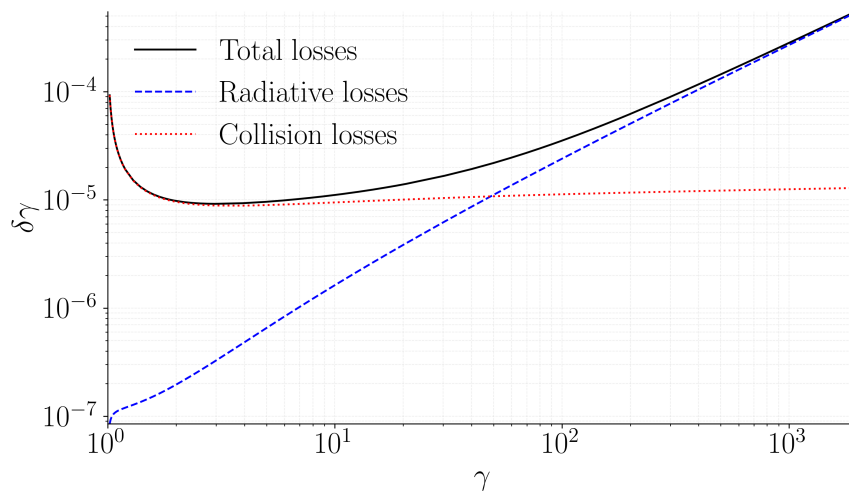
Figure 3.4. The electron energy losses $\delta\gamma$ due to radiation and collision stopping powers, experienced by the electron with kinetic energy γ from penetrating the nanoplate of solid copper with the thickness of $\hat{\lambda} = 0.2\pi$. The data reported by NIST [41] is used, demonstrating that $\delta\gamma \ll \gamma$ for the target parameters considered in this chapter.

in our PIC simulations.

3.3.1 Numerical verification

Analysis from Section 3.3 is verified with the series of single-particle simulations. In these simulations, we vary setup parameters a_0, $\hat{D}$, $W_{\max}^{(-)}$ and $W_{\max}^{(+)}$, and the initial conditions of the electron $\hat{y}(0)$, $\hat{P}_y(0)$, C. Initial conditions are chosen so that the assumption (3.16) is satisfied at the beginning of the simulation. We run simulations for several ζ, changing ζ between simulations by changing a_0, $\hat{D}$, and C parameters. We examine the Poincaré cross-section of the electron trajectory, showing the electrons energies when electron crosses $W^{(+)}(\hat{y}) = 0$ versus corresponding laser phase ξ modulo π, that is, $\xi - [\xi, \pi]$, as in Fig. 3.5. Poincaré cross-sections allow distinguishing stochastic and quasi-periodic electron motion because, for quasi-periodic motion, Poincaré cross-section shows smooth curves of preserved KAM surfaces. Some Poincaré cross-sections still have preserved KAM surfaces (smooth arms at larger energies in Fig. 3.5). For these cases, we
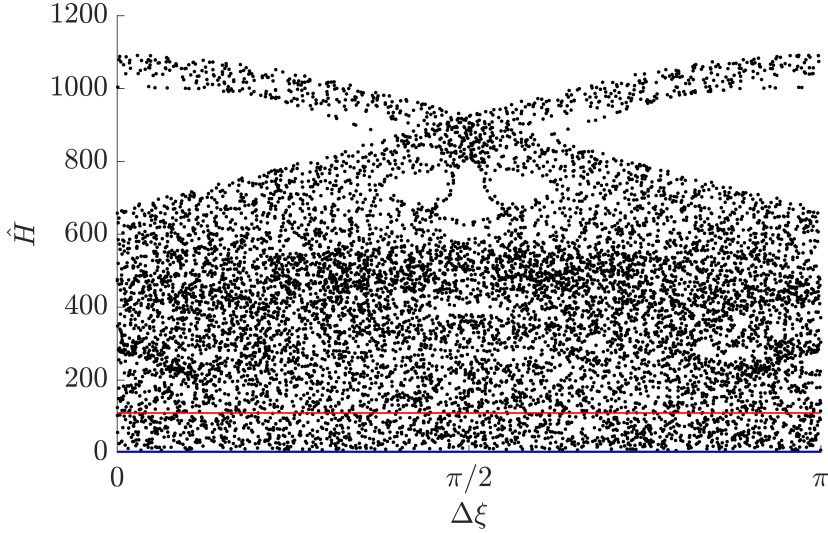
Figure 3.5. Poincaré cross-section for the electron with $C = W_{\mathrm{max}}^{(-)} = 2$, $W_{\mathrm{max}}^{(+)} = 5$, $\hat{y}(0) = 0.4\hat{D}$, $\hat{P}_y(0) = 3.0$, $\hat{D} = 500$. Parameters are chosen so that $\zeta = 1000$, and assumptions of analysis are satisfied. The motion is stochastic; however, a stability island exists for energies above 600. The red line at $\hat{H} \sim 100$ shows the initial energy of the electron, and the blue line at $\hat{H} = 7$ shows $W_{\mathrm{max}}^{(+)} + C$.

consider the maximum of $\hat{H}$ below the stability islands. The scalings from single particle simulations match with (3.26) and (3.32), as shown in Fig. 3.6.

3.4 Simulation results and discussion

Here we present our PIC simulation results and compare them to the analytical models from previous sections.

3.4.1 x-polarized laser

To show how the x-polarized laser propagates into the target, we consider the setup with normalized laser amplitude $a_0 = 2.4$ and gaps between nanoplates $\hat{D} = 4\pi$. From the PIC simulation of that setup, we plot the components of electric and magnetic fields, and compare them to our analytical model from Section 3.1.1. We choose $\hat{t} = 22\pi$, when

42
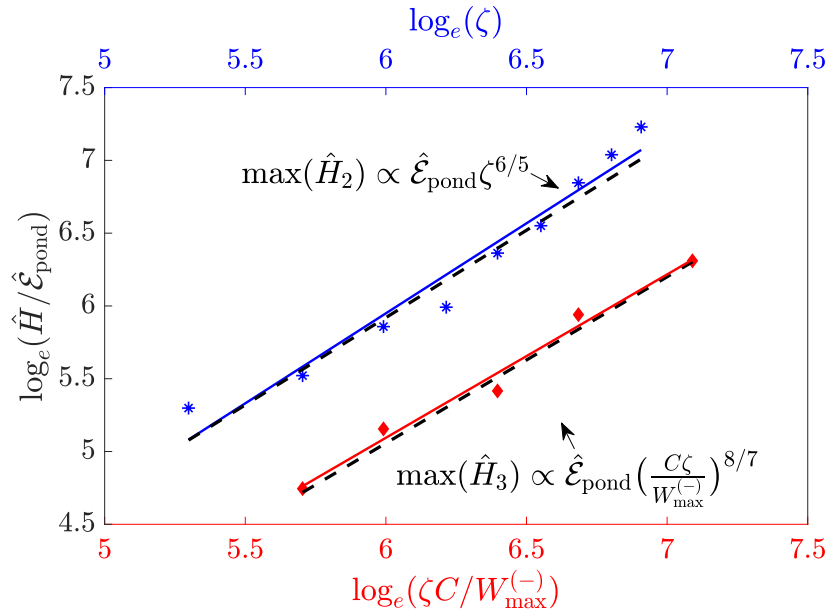
Figure 3.6. Scaling of maximum stochastic energy for cases $C \sim W_{\max}^{(-)}$ (blue line corresponding to $\max(\hat{H}_2)$) and $C \ll W_{\max}^{(-)}$ (red line corresponding to $\max(\hat{H}_3)$), for various values of ζ, C and $W_{\max}^{(-)}$ Dashed lines shows scalings (3.26) and (3.32) for reference.
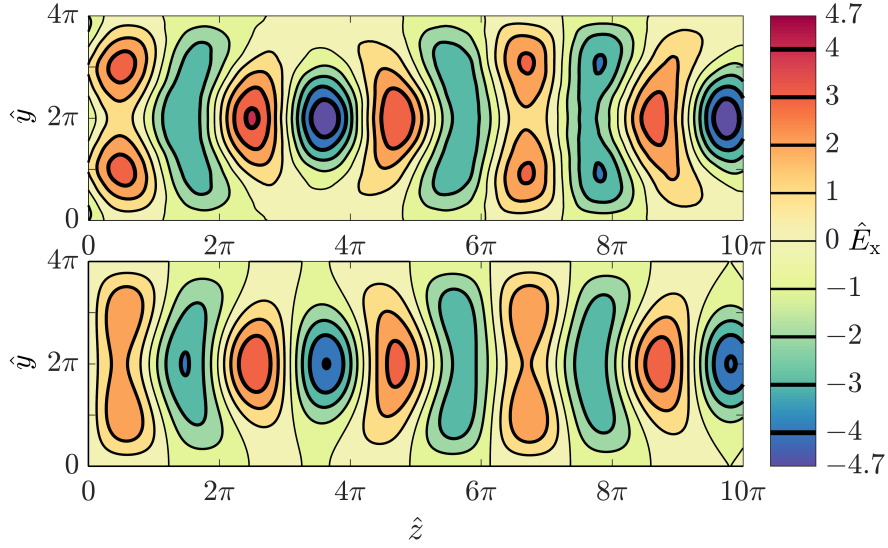
Figure 3.7. The x-component of the electric field $\hat{E}_x$ inside the gap of size $\hat{D} = 4\pi$, obtained from PIC simulation (top) with x-polarized laser and analytical model from Subsection 3.1.1 (bottom).

roughly half of the laser pulse has passed the gap entrance at $\hat{z} = 0$. The x-component of the electric field $\hat{E}_x$ is shown in Fig. 3.7, where the top subplot shows data from PIC and the bottom subplot shows analytical prediction. Likewise, the z-component of the magnetic field $\hat{B}_z$ is shown in Fig. 3.8. Note that the model proposed in Section 3.1.1 does not deal with electrodynamics of plasma and does not consider any specific relativistic effects. Despite its primitivity, the model captures the structure of $\hat{E}_x$ from the relativistic PIC simulation.

In Section 3.1.1 we predicted that the x-polarized pulse will not extract as many electrons as the y-polarized pulse will from the same target. In order to compare the density of extracted electrons, we plot the density of electrons from our PIC simulation in Fig. 3.9. In agreement with Section 3.1.1, PIC simulations show that an x-polarized pulse heats electrons less efficiently than a y-polarized pulse, as demonstrated in Fig. 3.14.
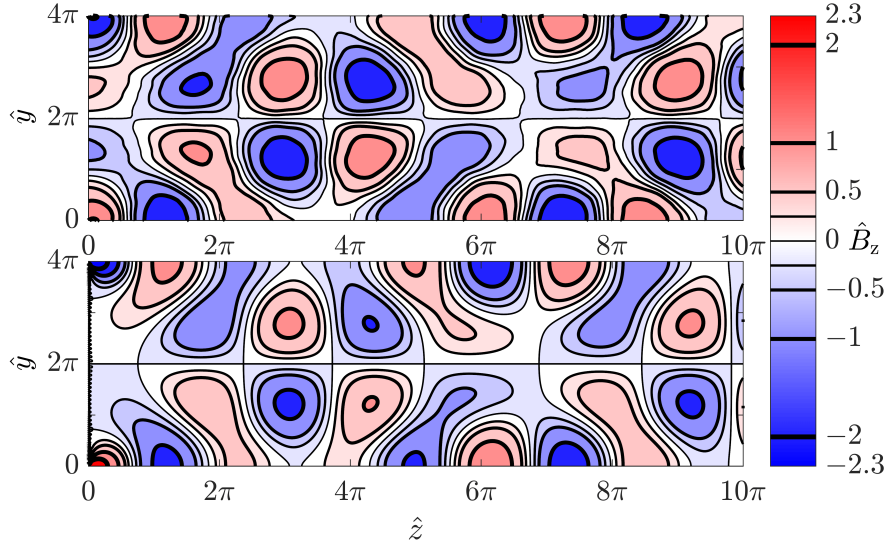
Figure 3.8. The z-component of the magnetic field $\hat{B}_z$ inside the gap of size $\hat{D} = 4\pi$, obtained from PIC simulation (top) with x-polarized laser and analytical model from Subsection 3.1.1 (bottom).

3.4.2   y-polarization

In Section 3.2, we demonstrate that when the y-polarized pulse propagates between nanoplates, it extracts some of the electrons. To illustrate the process of electron extraction, we consider the setup with $a_0 = 2.4$ and $\hat{D} = 4\pi$. From the PIC simulation of this setup, we plot the electron density between two nanoplates at time $\hat{t} = 22\pi$, as shown in Fig. 3.10. Note that electron extraction from the same target was also considered in Fig. 3.9 in Section 3.4.1. Simulation data presented in Figs. 3.9 and 3.10 shows that the y-polarized laser extracts more electrons than the x-polarized does from the same target, in agreement with analysis from Section 3.1.1.

Our analysis presented in Section 3.2 suggests that extraction of electrons from the nanoplates leads to creation of quasi-static electric $\hat{\mathbf{E}}_{qs}$ and magnetic $\hat{\mathbf{B}}_{qs}$ fields. We now verify this prediction with our PIC simulation. To get the static components of $\hat{\mathbf{E}}$ and $\hat{\mathbf{B}}$ fields in PIC simulation, we time-averaging these fields over one laser period $\hat{T}$. We use the

45
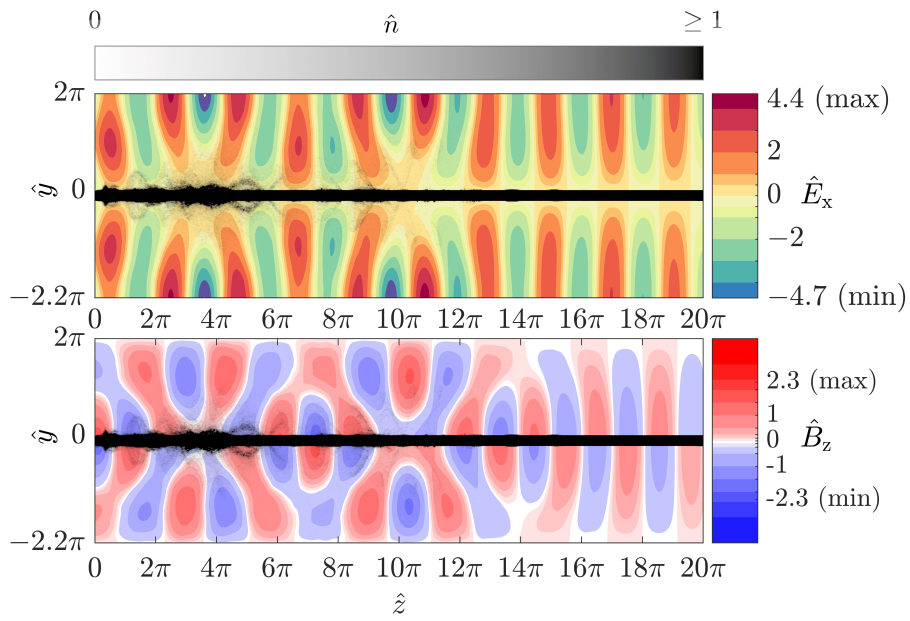
Figure 3.9. Electron number density, overlaid with the components of electric $\hat{E}_x$ and magnetic $\hat{B}_z$ fields for the case of polarized pulse.

y-component of the time-averaged electric field $\langle \hat{\mathbf{E}} \rangle \equiv \hat{\mathbf{E}}_{qs}$ to calculate the scalar potential $\hat{U}^{PIC}$ defined as $\langle \hat{E}_y \rangle = d\hat{U}^{PIC}/d\hat{y}$, and the z-component of the time-averaged magnetic field $\langle \hat{\mathbf{B}} \rangle = \hat{\mathbf{B}}_{qs}$ to calculate the vector potential $\hat{A}_B^{PIC}$ defined as $\langle \hat{B}_z \rangle = d\hat{A}_B^{PIC}/d\hat{y}$. The magnitude of $\langle \hat{E}_y \rangle$ is largest near the nanoplates where $|\langle \hat{E}_y \rangle| \approx a_0$, as predicted in Section 3.2. Profiles of $\hat{U}^{PIC}$ and $\hat{A}_B^{PIC}$ from PIC simulations with $a_0 = 2.4$ and different gap sizes $\hat{D}$ are shown in Fig. 3.11. In agreement with the analysis in Section 3.2, electrons extracted from targets with larger $\hat{D}$ travel further along the z-axis before mixing and creating homogeneous electron density, and hence for targets with larger $\hat{D}$ parabolic U^{PIC} and A^{PIC} potentials are formed at larger $\hat{z}$. We note that Fig. 3.11 includes the cases of $\hat{D} = 12\pi$, 16π and 24π, where the length $\hat{L} = 40\pi$ was insufficient for the parabolic potentials to form. In PIC simulations with $a_0 = 2.4$ and $\hat{D} < 8\pi$, the amplitudes of scalar $\hat{U}^{PIC}$ and vector $\hat{A}_B^{PIC}$ potentials are approximated well by a parabolic curve. In agreement with our analysis, parabolic potentials scale with the gap size $\hat{A}_B^{PIC}$, $\hat{U}^{PIC} \propto \hat{D}$. The
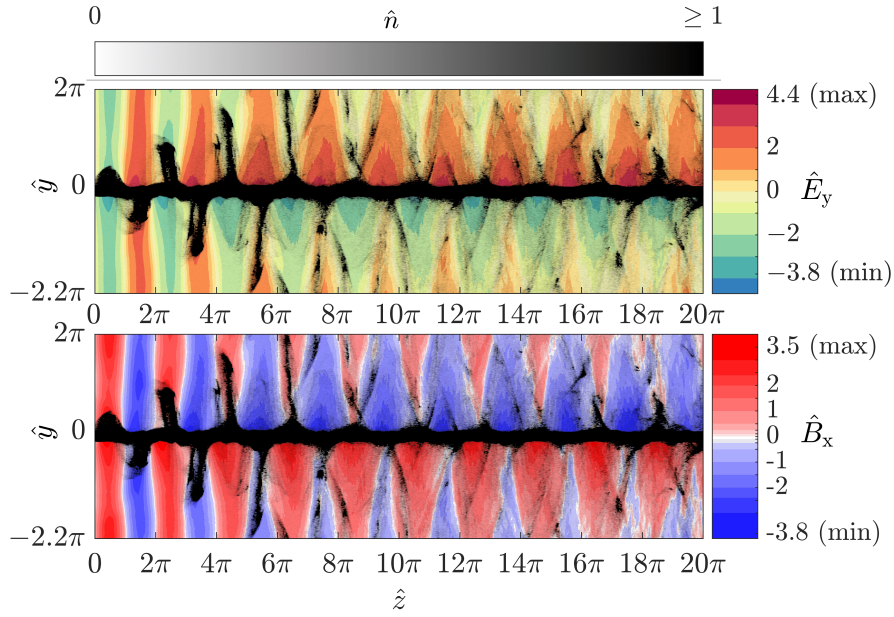
Figure 3.10. Electron number density, overlaid with the components of electric $\hat{E}_{\mathrm{y}}$ and magnetic $\hat{B}_{\mathrm{x}}$ fields for the case of polarized pulse.

estimate for static electric and magnetic fields neglects aspects such as the z-dependence of $a(z)$ laser potential due to absorption of laser energy by the target, however the derived scalings for $\max(\hat{U})$ and $\max(\hat{A}_{\mathrm{B}})$ match reasonably well with the analysis. Specifically, for simulations with $a_0 = 2.4$, Eqs. (3.8) and (3.9) predict scaling $\max(\hat{U}) = a_0\hat{D}/4 = 0.6\hat{D}$, while the scaling in PIC simulations is $\max(\hat{U}) \propto 0.4\hat{D}$ as shown in Fig. 3.11. The $\max(\hat{U}) = |\hat{v}_{\mathrm{z}}|\hat{A}_{\mathrm{B}}$ estimate agrees well with the series of simulations presented in Fig. 3.12, where we varied a_0 while keeping $\hat{D} = 2\pi$ and tracked the subset of electrons to determine the average velocity component $\langle \hat{v}_{\mathrm{z}} \rangle$ in the gaps of the target. Results shown in Fig. 3.12 also confirm that $\langle \hat{v}_{\mathrm{z}} \rangle$ increases with a_0, even though the values of $\langle \hat{v}_{\mathrm{z}} \rangle$ for larger a_0 are smaller estimate (3.7), and therefore the ponderomotive $\langle \hat{v}_{\mathrm{z}} \rangle$ estimate becomes less adequate in the presence of larger $\hat{U}$ and $\hat{A}_{\mathrm{B}}$ potentials. For the $a_0 = 2.4$, estimate (3.7) gives $\langle \hat{v}_{\mathrm{z}} \rangle = 0.74$, which agrees with $\hat{v}_{\mathrm{z}}^{\mathrm{PIC}} = 0.73$ recorded in a PIC simulation with $\hat{D} = 2\pi$. The main conclusion regarding quasi-static $\hat{\mathbf{E}}_{\mathrm{qs}}$ and $\hat{\mathbf{B}}_{\mathrm{qs}}$ fields is that their corresponding

47
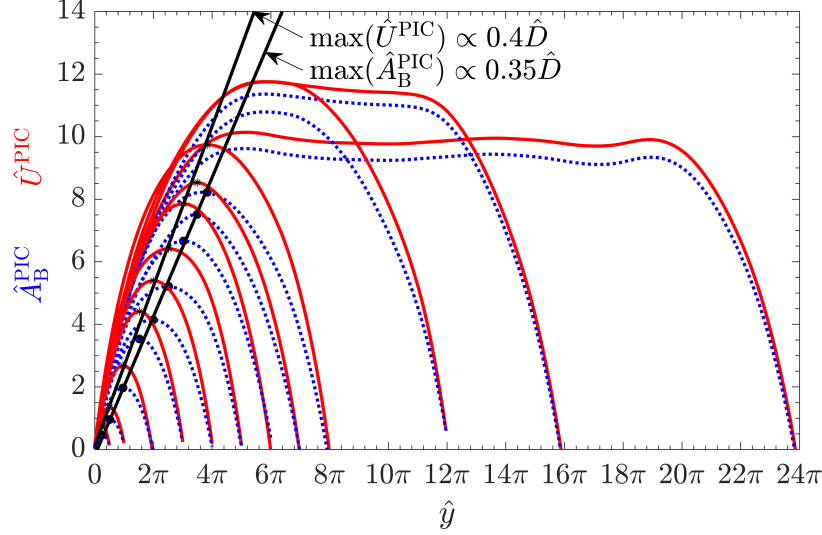
Figure 3.11. Profiles of the electrostatic potential $\hat{U}^{\mathrm{PIC}}$ (red solid lines) and vector potential $\hat{A}_{\mathrm{B}}^{\mathrm{PIC}}\mathbf{e}_{\mathrm{z}}$ (blue dotted lines). Each $\hat{U}^{\mathrm{PIC}}$ and $\hat{A}_{\mathrm{B}}^{\mathrm{PIC}}\mathbf{e}_{\mathrm{z}}$ is shown from $\hat{y} = 0$ to $\hat{y} = \hat{D}$, where $\hat{D}$ is the gap size from the corresponding PIC simulation. All PIC simulations shown on this figure had the same laser with $a_0 = 2.4$.

potentials $\hat{U}$ and $\hat{A}_{\mathrm{B}}\mathbf{e}_{\mathrm{z}}$ are indeed parabolic if the depth L is sufficient, and $|\hat{U}| = |\hat{v}_{\mathrm{z}}\hat{A}_{\mathrm{B}}|$ hence there is a residual $W_{\max}^{(-)}$ always present.

Having confirmed the onset of quasi-static $\hat{\mathbf{E}}_{\mathrm{qs}}$ and $\hat{\mathbf{B}}_{\mathrm{qs}}$ fields and the residual between them, we now consider the acceleration of electrons in our PIC simulations to verify the analysis presented in Section 3.3. To demonstrate when the problem setup considered in Section 3.3 becomes relevant to our PIC simulations, consider an example from PIC simulation with $a_0 = 2.4$ and $\hat{D} = 8\pi$, shown in Fig. 3.13, where we plot the subset of electrons between two nanoplates at time $\hat{t} = 38\pi$. As Fig. 3.13 shows, the profiles of $\hat{U}^{\mathrm{PIC}}$ and $\hat{A}_{\mathrm{B}}^{\mathrm{PIC}}$ remain constant with $\hat{z}$ after $\hat{z} \gtrsim 12\pi$, where the electrons have filled the gap. Therefore, electrons with $\hat{z} \gtrsim 12\pi$, shown in Fig. 3.13, are relevant to the analysis from Section 3.3. We note that in the setup considered in Section 3.3, C of the electron is conserved, meanwhile in PIC simulation, C can change prior to formation of quasi-static fields, and also in the quasi-static fields via mechanisms discussed at the end of Section 3.3.
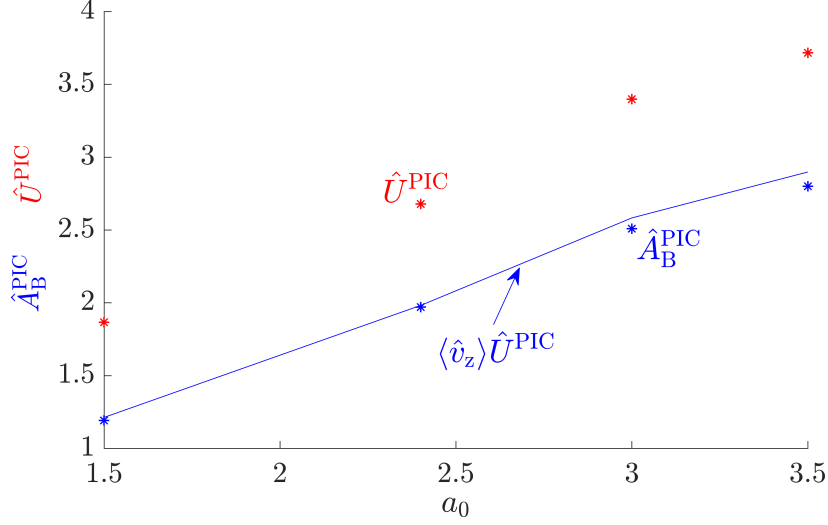
Figure 3.12. Maximum values of scalar $\max(\hat{U}^{\mathrm{PIC}})$ and vector $\max(\hat{A}_B^{\mathrm{PIC}})$ agree with the estimate $\max(\hat{A}_{\mathrm{B}}^{\mathrm{PIC}}) = \langle v_z \rangle \max(\hat{U}^{\mathrm{PIC}})$, where $\langle v_z \rangle$ is the average v_z velocity component of the electrons in the gap.

Since the immobile electron has $C \sim 1$, it is reasonable to assume that the majority of electrons will have $C \sim 1$ when the quasi-static fields are established. Furthermore, if the residual between the quasi-static electric and magnetic field corresponds to $W_{\max}^{(-)} \sim 1$, then there will be electrons with $C \sim W_{\max}^{(-)}$ that can undergo efficient stochastic acceleration. As the electrons undergo stochastic acceleration, the density in the gap $\langle n \rangle$ and the average velocity $\langle \hat{v}_z \rangle$ remains unchanged, so the quasi-static electric and magnetic fields also stay the same. Our next step is to show that the low-energy electrons with C closest to $W_{\max}^{(-)}$ can accelerate the most efficiently, and that their maximum stochastic energy matches the maximum energy in PIC simulations. We start by finding the maximum electron energy $\gamma_{\max}^{\mathrm{PIC}}$ in PIC simulations from the energy distribution functions $f(\gamma)$, as shown in Fig. 3.14. Then, we use $\hat{U}^{\mathrm{PIC}}$ and $\hat{A}_{\mathrm{B}}^{\mathrm{PIC}}$ from each simulation to study the electron heating in a single particle model. For given $\hat{U}^{\mathrm{PIC}}$ and $\hat{A}_{\mathrm{B}}^{\mathrm{PIC}}$ potentials, we calculate how the unperturbed frequency $\hat{\Omega}(C)$ changes with C for the electron with $\gamma_{\max}^{\mathrm{PIC}}$. The $\hat{\Omega}(C)$
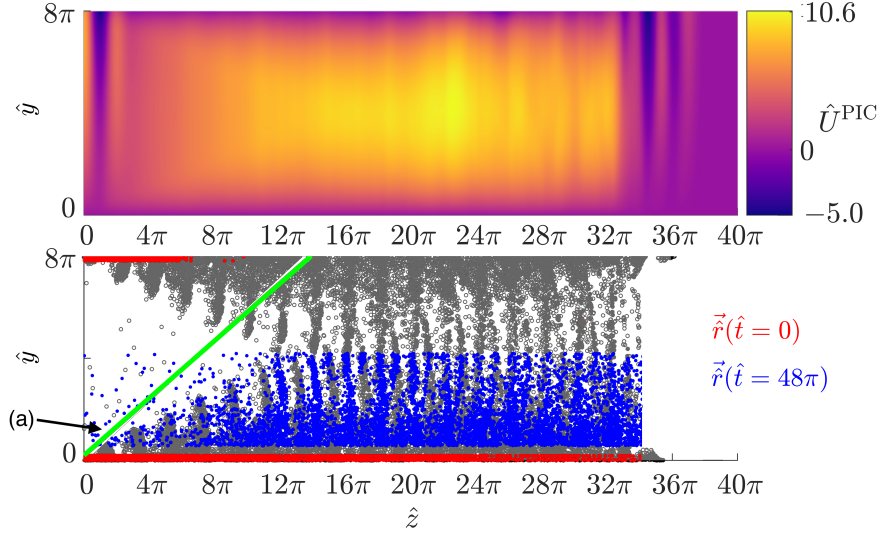
Figure 3.13. The top panel shows scalar potential $\hat{U}^{\mathrm{PIC}}$ inside the gap from a PIC simulation with $a_0 = 2.4$, $\hat{D} = 8\pi$, at time $\hat{t} = 48\pi$. The bottom panel shows the positions of the electrons from the random subset (light gray dots) sampled in the same PIC simulation at time $\hat{t} = 48\pi$. Extracted electrons fill the region of the gap with $\hat{z}$ from 12π to 32π, the same region has the $\hat{U}^{\mathrm{PIC}}$ and $\hat{A}_{\mathrm{B}}^{\mathrm{PIC}}$ independent of $\hat{z}$. The green line marked (a) shows the extraction angle estimate (3.6). On the bottom panel, red points (dark gray if grayscale) at $\hat{D} = 0$ and 8π show the initial position $\vec{\hat{r}}(\hat{t} = 0)$ of the electrons that are located between $\hat{D} = 0$ and 4π at time $\hat{t} = 48\pi$.
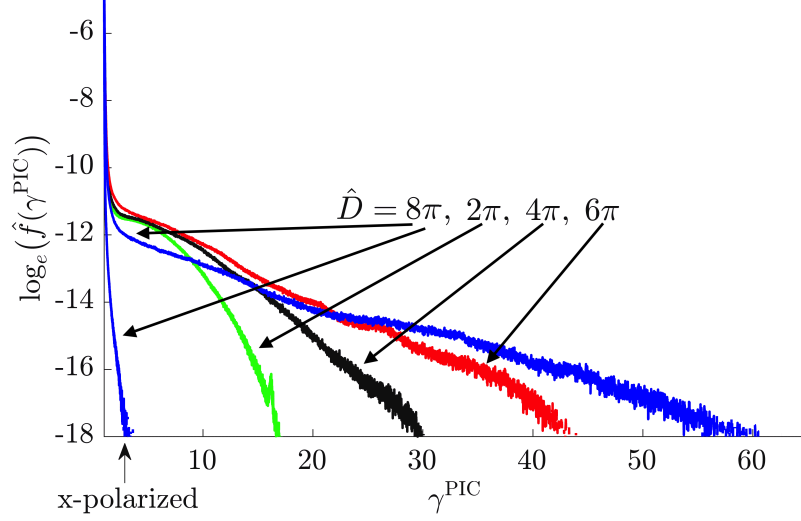
Figure 3.14. Distribution of electron's Lorentz factor γ normalized by total number of particles in the target ($\sim 10^{10}$ taking the size along x as $\Delta x \sim \lambda$ and size along y as $\Delta y \sim d + D$) for PIC simulations with $a_0 = 2.4$ and different $\hat{D}$. The corresponding values of $\hat{D}$ are 2π (green), 4π (black), 6π (red), 8π (blue). Data shown for the x-polarized $\hat{D} = 8\pi$ verifies that x-polarized pulse heats electrons less efficiently, in agreement with Section 3.1.1.

dependencies shown in Fig. 3.15 shows that $C \ll 1$ electrons have $\hat{\Omega} \gg 1$ and therefore unable to exchange energy with the laser efficiently. The frequency $\hat{\Omega}$ drops to $\hat{\Omega} < 1$ in a narrow region of $C \approx W_{\max}^{(-)}$. This $C \approx W_{\max}^{(-)}$ also corresponds to the maximum stochastic energy recorded in the single-particle simulation, as shown in Fig. 3.16. Our analysis shows that the maximum stochastic energy $\max(\hat{H})$ surpasses the ponderomotive energy $\hat{\mathcal{E}}_{\text{pond}}$ for electrons with $\zeta \gtrsim 1$, and scales as $\max(\hat{H}) \propto \hat{\mathcal{E}}_{\text{pond}} \zeta^{6/5}$. The scaling from PIC results shown in Fig. 3.17 is $\max(\hat{H}) \propto \hat{\mathcal{E}}_{\text{pond}} \zeta^{0.98}$.

Apart from the maximum energy, hot electron bunches are also characterized by assigning them a temperature or considering the heat flux of electrons [25]. To characterize the mean energy of electrons, we determine the energy $\hat{\mathcal{E}}_{\text{mean}}$ at which half of the electron's heat flux is captured. In the series of PIC simulations shown in Fig. 3.17, the scaling of
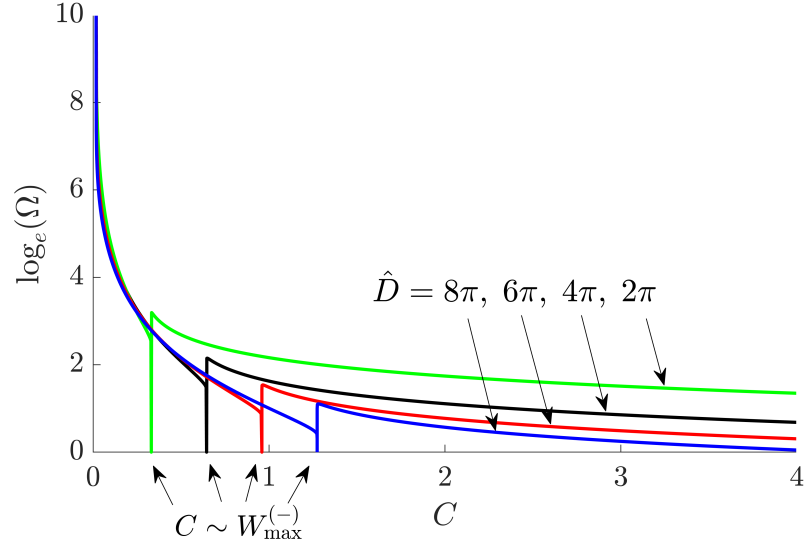
Figure 3.15. The frequency of unperturbed electron motion $\hat{\Omega}$ for scalar $\hat{U}$ and vector $\hat{A}_{\mathrm{B}}\mathbf{e}_{\mathrm{z}}$ potentials measured in PIC simulations with $a_0 = 2.4$ and $\hat{D} = 2\pi$(green), 4π (black), 6π (red), 8π (blue). Dotted lines show $C \approx W_{\mathrm{max}}^{(-)}$, where $\hat{\Omega}$ drops to zero

mean electron energy is $\max(\hat{\mathcal{E}}_{\mathrm{mean}}) \propto a_0^2 \zeta^{0.8}$.

3.5   Conclusion

In this chapter, we investigated various aspects of laser interaction with a 2D nanoplate array target. It showed that the target behaves much like a waveguide for the laser propagation: for the x-polarized pulse, the plane wave laser pulse becomes a superposition of TE-modes, whereas, for a y-polarized pulse, the laser propagates as TEM mode. The analysis showed that for x-polarized laser, the ponderomotive force from the EM fields would prevent the extraction of electrons from the target. As a result, electrons remain in the target and do not interact with the laser field. The electron acceleration is suppressed, which has been confirmed by the PIC simulations, which show that the maximum electron energies for an x-polarized pulse are lower than those for a y-polarized pulse. On the other hand, the y-polarized laser pulse, propagating between the nanoplates
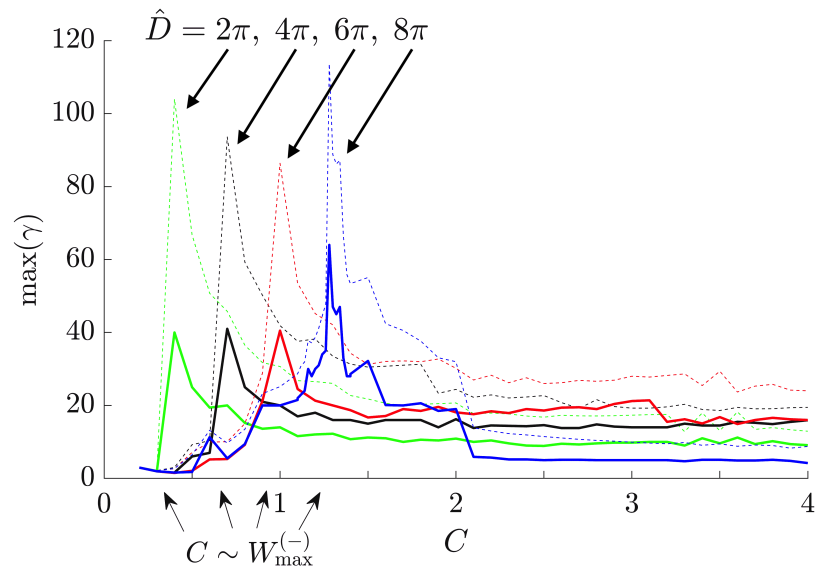
Figure 3.16. The maximum energy (dashed curves) and energy below stability arms (solid curves) from single particle simulations with initial $\hat{H} \sim 1$ and for scalar $\hat{U}$ and vector $\hat{A}_B \mathbf{e}_z$ potentials from PIC simulations with $a_0 = 2.4$ and $\hat{D} = 2\pi$(green), 4π (black), 6π (red), 8π (blue)
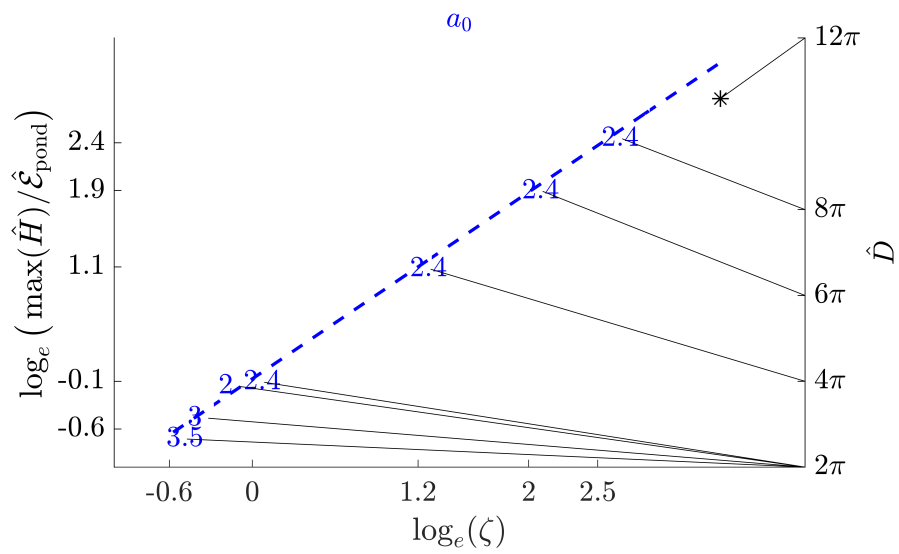
Figure 3.17. The energy scaling in the PIC simulations with $W_{\max}^{(-)} \sim 1$. Data is labeled with blue numbers, corresponding to the values of a_0 in PIC simulations. The fitted slope is 0.98. Black star that does not fit the scaling corresponds to the simulation with $a_0 = 2.4$ and $\hat{D} = 12\pi$, where $\hat{L} = 20$ turned out to be insufficient for the electrostatic potentials to form.

while preserving the plane-wave structure, can pull electrons out from the nanoplates due to the Lorentz force from its electric field. This extraction of electrons can be described well by the motion of a single electron in a plane wave, where the laser pulse can extract bunches of electrons from their parent nanoplates. Electron bunches streaming along and against the y-axis are shifted in the z-axis direction by the laser phase $\Delta\xi = \pi$. As a result, when these counter-propagating bunches pass through each other, they form homogeneous electron density $\hat{\tilde{n}}$ depending on the laser amplitude a_0 and gap depth $\hat{D}$ and thus create a quasi-static electric field $\hat{\mathbf{E}}_{qs}$ in the y-direction. Simultaneously, the electrons in the gap move along the z-axis, and thus their current generates a quasi-static magnetic field $\hat{\mathbf{B}}_{qs}$ in the x-direction. Our estimates for the quasi-static EM fields suggest that $|\hat{\mathbf{E}}_{qs}| = |\hat{v}_z \hat{\mathbf{B}}_{qs}|$, where $\hat{v}_z$ is the averaged longitudinal speed of extracted electrons. Therefore, the quasi-static magnetic field is relatively smaller than the electric field. In contrast to the ion-channel case, we showed that this small difference in these quasi-static fields is crucial for the electron acceleration beyond the ponderomotive scaling.

After the formation of these quasi-static fields, the new injected electrons in the gap can be accelerated via the resonance between the frequency of electron oscillating in the quasi-static fields and laser frequency. We show that the electron can be accelerated via the stochastic motion, which we study within the 3/2D Hamiltonian framework. Our analysis shows that the electron energy can largely exceed the ponderomotive energy scaling due to the onset of stochastic motion, which depends on a universal parameter ζ combining the laser amplitude a_0, gap size $\hat{D}$ and initial electron conditions. We found that the stochastic motion requires $\zeta > 1$, which can be easily satisfied for our PIC simulations. The analysis demonstrated that for larger gap depth $\hat{D}$, the stochastic motion results in larger electron energy. However, if the laser amplitude increases, even though the maximum electron energy is enhanced, its ratio to the ponderomotive scaling is decreased. Particularly, if the laser amplitude is large enough that $\zeta \tilde{<} 1$, then the stochastic motion is not possible, and the maximum electron energy will be the same order with ponderomotive scaling.

We note that the process of electron acceleration in laser-particle interaction is more complex than the simple model we considered, but our analysis explains how the energetic electrons will be produced in laser-target interaction via the stochastic electron motion. Presented analysis can help with interpreting the results of both future experiments and simulations.

The work presented in this chapter is a reprint of the material as it appears in *Laser-driven electron acceleration in nanoplate array targets* in Physical Review E 103, 013204 (2021), by A. R. Knyazev, Y. Zhang, and S. I. Krasheninnikov. The dissertation author was the primary investigator and author of this paper.

Chapter 4

Linearized multi-species collision operator for gyrokinetic simulations

4.1 Introduction

In recent years, various collision operator models have been implemented in numerous gyrokinetic codes in order to simulate Coulomb collisions in tokamak plasmas (see [42, 43, 44, 45, 46, 47, 48] and references therein). The correct expression for the Coulomb operator is well known (e.g., Landau form [49]) but often avoided in kinetic modeling because of the high computation cost. Accordingly, only some gyrokinetic codes [50, 51] include the correct collision operator, typically referred to as the Fokker-Planck operator. Instead, recent reports [44, 43, 45, 46, 47, 48] focus on implementing increasingly complex reduced collision operators and extending these operators for the case of unlike species. The implemented models differ in physical properties, such as, for example, the rate of entropy production and the velocity dependence of the collision frequency. Accordingly, proposed operators have different scope of use. Notably, some recent implementations of unlike collisions (e.g., [47, 46]) produce no thermal force, which is important for impurity transport in the tokamak edge [52, 53].

This chapter describes the implementation of a multi-species linearized collision operator, in the continuum gyrokinetic code COGENT [54]. The operator is based on the Landau operator, and preserves the correct $\lambda \sim (\mathbf{v}_a - \mathbf{v}_b)^4$ dependence of the Coulomb

mean free path on a relative velocity $\mathbf{v}_a - \mathbf{v}_b$ of colliding species a and b. This retained velocity dependence enables to recover thermal force, as well as the friction force as they appear in the Braginskii fluid model [6], in the COGENT simulations of highly collisional plasmas. For the case of equal background temperatures of the colliding species, the operator reduces to the operators developed by Sugama [42] and Kolesnikov [55] for gyrokinetic simulations with fixed background Maxwellians. However, in contrast to the Sugama model, the newly implemented operator directly retains collisional thermalization of background Maxwellians with different temperatures. The resulting operator provides a numerically efficient way to simulate collisions between unlike species. It is also worth noting an alternative approach to include energy exchange between background centered Maxwellians implemented in the gyrokinetic code GYSELA [44] code.

We benchmark this operator in COGENT kinetic simulations of a parallel plasma transport in a slab geometry, against the Braginskii fluid model. We measure values of transport coefficients from kinetic simulations results and find that they are close to values obtained by Braginskii [6] for the Landau operator [49]. Finally, we consider a toroidal annulus geometry and simulate radial impurity transport in the strongly collisional Pfirsch-Schlüter regime, demonstrating good agreement with the results [56] of the local neoclassical theory.

The chapter is organized as follows. Section 2 contains an overview of the COGENT code and describes the newly implemented collision operator. In Section 3, we review COGENT simulations of single component plasma in a slab geometry, and the heavy impurity transport in toroidal geometry. Section 4 summarizes presented results and gives a conclusion.

4.2 Model description

This section describes the main aspects of the COGENT code and introduces the newly implemented collision model. COGENT is a continuum Eulerian gyrokinetic code. The electrostatic version of the COGENT code (used for simulations in this article) describes coupled evolution of the gyrocenter distribution function and the electrostatic potential for plasma in the external magnetic field. The code solves for a gyrocenter distribution function $f_a(\mathbf{R}_a, v_{||}, \mu_a, t)$ for kinetic species a, where $\mathbf{R}_a$ is the guiding center coordinate, $v_{||} = \mathbf{v} \cdot \mathbf{B}/B$ is the component of velocity $\mathbf{v}$ along the magnetic field $\mathbf{B}$ of magnitude B, and μ_a is the adiabatic invariant of species a with mass m_a. COGENT supports several magnetic $\mathbf{B}$ field geometries: slab, Miller closed-flux model [57] for the core region, and a single-null [58] X-point geometry for cross-separatrix simulations. The numerical algorithm used in COGENT utilizes a high-order finite-volume conservative discretization. The current electrostatic implementation of the code adopts a long wavelength limit $k\rho_i \ll 1$, where ρ_i is the gyroradius of ion species and k is the wavenumber for electrostatic potential variations. For simulations considered in this article, the gyrokinetic equation simulated in COGENT can be written for species a as

$$\frac{\partial B_{||a}^* f_a}{\partial t} + \nabla \cdot (\dot{\mathbf{R}}_a B_{||a}^* f_a) + \frac{\partial}{\partial v_{||}}(\dot{v}_{||} B_{||a}^* f_a) =$$

$$= B_{||a}^* \left(C(f_a) + C(f_a, f_b) \right), \tag{4.1}$$

$$\dot{\mathbf{R}}_a = \frac{1}{B_{||a}^*} \left[v_{||}\mathbf{B}_a^* + \frac{1}{e_a}\mathbf{b} \times (e_a \nabla \Phi + \mu_a \nabla B) \right], \tag{4.2}$$

$$\dot{v}_{||} = -\frac{1}{m_a B_{||a}^*}\mathbf{B}_a^* \cdot (e_a \nabla \Phi + \mu_a \nabla B), \tag{4.3}$$

$$\mathbf{B}_a^* = \mathbf{B} + \frac{m_a v_{||}}{e_a}\nabla \times \mathbf{b}, \tag{4.4}$$

where $\mathbf{b} = \mathbf{B}/B$ and $B_{||a}^* = \mathbf{B}_a \cdot \mathbf{b}$, Φ is the long wavelength neoclassical electrostatic potential, $C(f_a)$ is a like-species collision operator, and $C(f_a, f_b)$ is the newly implemented

unlike-species collision operator described in the rest of this section. Further implementation details for the axisymmetric (4D) and non-axisymmetric (5D) versions of the COGENT code are available elsewhere [59, 60].

The linearized multi-species collision operator presented in this section utilizes the approach described by Kolesnikov in [55]. Specifically, the distribution functions of colliding species f_a and f_b are assumed to be close to Maxwellian distributions with zero bulk velocities,

$$f_s^M = \frac{n_s}{\pi^{3/2} v_{Ts}^3} \exp\left(-\frac{v^2}{v_{Ts}^2}\right); \ s = a, b, \tag{4.5}$$

where $v = \sqrt{v_\parallel^2 + 2\mu_s B/m_s}$ is the velocity and $v_{Ts} = \sqrt{2T_s/m_s}$ is the thermal speed of species s with temperature T_s, mass m_s and density n_s. Collision operator $C(f_a^M + \delta f_a, f_b^M + \delta f_b)$ is then approximated with a sum of linear operators as

$$C(f_a, f_b) = C_T(f_a^M, f_b^M) + C_T(\delta f_a, f_b^M) + C_F(f_a^M, \delta f_b). \tag{4.6}$$

The first two terms in Eq. (4.6) describe collisions of species a with the Maxwellian background f_b^M of species b. For the background species with charge e_b and mass m_b, the corresponding *test particle* operator C_T can be expressed in the Landau form [49] as

$$C_T(f_a, f_b^M) = -\frac{m_a L^{a/b}}{8\pi} \times$$
$$\times \frac{\partial}{\partial v_\alpha} \int d\mathbf{v}' \{ \frac{f_a(\mathbf{v})}{m_b} \frac{\partial f_b^M(\mathbf{v}')}{\partial v_\beta'} - \frac{f_b^M(\mathbf{v}')}{m_a} \frac{\partial f_a(\mathbf{v})}{\partial v_\beta} \} U_{\alpha\beta}, \tag{4.7}$$

$$U_{\alpha\beta} = \frac{1}{u^3}(u^2 \delta_{\alpha\beta} - u_\alpha u_\beta); \ u_\beta = v_\beta - v_\beta', \tag{4.8}$$

$$L^{a/b} = \ln \Lambda \left(\frac{4\pi e_a e_b}{m_a}\right)^2, \tag{4.9}$$

where $\ln \Lambda$ is the Coulomb logarithm. This test particle operator C_T can be expressed in

COGENT coordinates as a divergence of the probability flux $\mathbf{\Pi}$ in the velocity space,

$$
\begin{aligned}
C_{\mathrm{T}}(f_{\mathrm{a}}, f_{\mathrm{b}}^{\mathrm{M}}) &= \nabla_{\mathrm{v}} \cdot \mathbf{\Pi} = \frac{\partial \Pi^{v_{\|}}}{\partial v_{\|}} + \frac{\partial \Pi^{\mu_{\mathrm{a}}}}{\partial \mu_{\mathrm{a}}} = \\
&= \frac{\partial}{\partial v_{\|}} \left\{ \nu_{\mathrm{D}} \left(\frac{\mu_{\mathrm{a}} B}{m_{\mathrm{a}}} \frac{\partial f_{\mathrm{a}}}{\partial v_{\|}} - v_{\|} \mu_{\mathrm{a}} \frac{\partial f_{\mathrm{a}}}{\partial \mu_{\mathrm{a}}} \right) + \right. \\
&\quad \left. + \frac{m_{\mathrm{a}}}{m_{\mathrm{a}} + m_{\mathrm{b}}} \nu_{\mathrm{s}} v_{\|} f_{\mathrm{a}} + \nu_{\|} v_{\|} \left(\mu_{\mathrm{a}} \frac{\partial f_{\mathrm{a}}}{\partial \mu_{\mathrm{a}}} + \frac{v_{\|}}{2} \frac{\partial f_{\mathrm{a}}}{\partial v_{\|}} \right) \right\} + \\
&\quad + \frac{\partial}{\partial \mu_{\mathrm{a}}} \left\{ \nu_{\mathrm{D}} \left(\frac{m_{\mathrm{a}}}{B} v_{\|}^2 \mu_{\mathrm{a}} \frac{\partial f_{\mathrm{a}}}{\partial \mu_{\mathrm{a}}} - v_{\|} \mu_{\mathrm{a}} \frac{\partial f_{\mathrm{a}}}{\partial v_{\|}} \right) + \right. \\
&\quad \left. + \frac{2m_{\mathrm{a}}}{m_{\mathrm{a}} + m_{\mathrm{b}}} \nu_{\mathrm{s}} \mu_{\mathrm{a}} f_{\mathrm{a}} + \nu_{\|} \mu_{\mathrm{a}} \left(2\mu_{\mathrm{a}} \frac{\partial f_{\mathrm{a}}}{\partial \mu_{\mathrm{a}}} + v_{\|} \frac{\partial f_{\mathrm{a}}}{\partial v_{\|}} \right) \right\}.
\end{aligned}
\tag{4.10}
$$

Expression Eq. (4.10) contains standard notations [61] for deflection frequency ν_{D}, slow-down rate ν_{s} and parallel diffusion rate ν_{s}, given by expressions

$$
\nu_{\mathrm{D}} = \nu_{\mathrm{ab}} \frac{v_{\mathrm{Ta}}^3}{v_{\mathrm{Tb}}^3} \left(\frac{\Omega}{\zeta^3} + \frac{1}{\zeta^3} \frac{d\Omega}{d\zeta^2} - \frac{\Omega}{2\zeta^5} \right),
\tag{4.11}
$$

$$
\nu_{\mathrm{s}} = \nu_{\mathrm{ab}} \frac{v_{\mathrm{Ta}}}{v_{\mathrm{Tb}}} \frac{T_{\mathrm{a}}}{T_{\mathrm{b}}} \left(1 + \frac{m_{\mathrm{b}}}{m_{\mathrm{a}}} \right) \frac{\Omega}{\zeta^3},
\tag{4.12}
$$

$$
\nu_{\|} = \nu_{\mathrm{ab}} \left(\frac{v_{\mathrm{Ta}}}{v_{\mathrm{Tb}}} \right)^3 \frac{\Omega}{\zeta^5},
\tag{4.13}
$$

where $\zeta = v/v_{\mathrm{Tb}}$, ν_{ab} is the collision frequency given by

$$
\nu_{\mathrm{ab}} = \frac{4\pi e_{\mathrm{a}}^2 e_{\mathrm{b}}^2 \ln \Lambda n_{\mathrm{b}}}{m_{\mathrm{a}}^2 v_{\mathrm{Ta}}^3},
\tag{4.14}
$$

and Ω is the Maxwell integral [62] that gives normalized value of integrating the Maxwellian distribution over sphere with radius ζ^2,

$$
\Omega = \frac{2}{\sqrt{\pi}} \int_0^{\zeta^2} \sqrt{t} e^{-t} dt = \mathrm{erf}(\zeta) - \frac{d\Omega}{d\zeta^2}, \quad \frac{d\Omega}{d\zeta^2} = \frac{2}{\sqrt{\pi}} \zeta e^{-\zeta^2}.
$$

As can be seen from the expression Eq. (4.10), $C_{\mathrm{T}}(f_{\mathrm{a}}, f_{\mathrm{b}}^{\mathrm{M}})$ is a differential operator, which makes it cheap to evaluate numerically.

The *field particle* operator $C_F(f_a^M, \delta f_b)$ describes collisions of Maxwellian component f_a^M with perturbation δf_b. When written in the Landau form (as done for C_T in Eq. (4.7)), the field particle operator involves a convolution integral over the velocity space, and is, from the numerical viewpoint, as expensive to evaluate as the full Landau operator. Accordingly, only some codes [63, 64] implement the field particle component of the linearized collision operator in the Landau form. Instead, linear collision models typically [42, 43, 44] postulate a reduced field particle operator that is more efficient to evaluate numerically. In the collision operator model proposed by Kolesnikov [55], the field particle operator is given by expressions

$$C_F(f_a^M, \delta f_b) = \delta P_{ab} \mathcal{R}_{ab} v_{||} + \delta E_{ab} \mathcal{Q}_{ab}, \tag{4.15}$$

$$\delta P_{ab} = - \int d\mathbf{v} \, m_b v_{||} C_T(\delta f_b, f_a^M), \tag{4.16}$$

$$\delta E_{ab} = - \int d\mathbf{v} \, \frac{m_b v^2}{2} C_T(\delta f_b, f_a^M), \tag{4.17}$$

$$\mathcal{R}_{ab} v_{||} = \frac{C_T(m_a v_{||} f_a^M, f_b^M)}{\int d\mathbf{v} \, m_a v_{||} C_T(m_a v_{||} f_a^M, f_b^M)}, \tag{4.18}$$

$$\mathcal{Q}_{ab} = \frac{C_T(m_a v^2 f_a^M, f_b^M)}{\int d\mathbf{v} \, (m_a v^2/2) C_T(m_a v^2 f_a^M, f_b^M)}. \tag{4.19}$$

Since previous reports [65, 55] contain typos in explicit form of the field operator C_F, corrected expressions are given below. In the case of equal temperatures $T_a = T_b = T$,

$$\mathcal{R}_{ab} = \frac{3\sqrt{\pi} f_a^M}{4 n_a T} \left(1 + \frac{m_b}{m_a}\right)^{3/2} \frac{\Omega}{\zeta^3}, \tag{4.20}$$

$$\mathcal{Q}_{ab} = \frac{\sqrt{\pi} f_a^M}{2 n_a T} \left(1 + \frac{m_b}{m_a}\right)^{3/2} \frac{1}{\zeta} \left(\frac{m_a}{m_b} \Omega - \frac{d\Omega}{d\zeta^2}\right). \tag{4.21}$$

It can be easily demonstrated that C_F provides conservation of momentum,

$$
\frac{d}{dt}\int d\mathbf{v} m_\mathrm{a} v_{||} f_\mathrm{a} = \int d\mathbf{v} m_\mathrm{a} v_{||} \Bigg(C_\mathrm{F}(f_\mathrm{a}^\mathrm{M}, \delta f_\mathrm{b})) +
$$

$$
+ C_\mathrm{T}(\delta f_\mathrm{a}, f_\mathrm{b}^M) + C_\mathrm{T}(f_\mathrm{a}^M, f_\mathrm{b}^M) \Bigg) = \delta P_\mathrm{ab} - \delta P_\mathrm{ba} -
\tag{4.22}
$$

$$
- \int d\mathbf{v} m_\mathrm{b} v_{||} C_\mathrm{T}(f_\mathrm{b}^M, f_\mathrm{a}^M) = -\frac{d}{dt}\int d\mathbf{v} m_\mathrm{b} v_{||} f_\mathrm{b},
$$

and energy (as can be shown analogously to Eq. (4.22)). From expressions Eqs. (4.15)-(4.19), it follows that the field particle C_F operator conserves particles if the test particle operator C_T does. Because of the divergence form Eq. (4.10) of the test particle operator $C_\mathrm{T}(f_\mathrm{a}, f_\mathrm{b}^\mathrm{M})$, conservation of the particle number density n_a during collisions can be enforced by setting the probability flux to zero $\mathbf{S} \cdot \mathbf{\Pi} = 0$ through the boundaries of the velocity domain S,

$$
\int d\mathbf{v} C_\mathrm{T}(f_\mathrm{a}, f_\mathrm{b}^\mathrm{M}) = \int_\mathrm{S} d\mathbf{S} \cdot \mathbf{\Pi} = 0,
\tag{4.23}
$$

where $\mathbf{S}$ is normal to surface S. Since the finite volume discretization scheme used in COGENT exactly recovers the Gauss divergence theorem, the test particle C_T (and, therefore, field particle C_F) operator conserves particles up to machine precision if the probability flux of C_T is adjusted according to Eq. (4.23).

It is instructive to compare the collision operator given by Eq (4.6) to previously published [44, 45, 48] linearized collision operator models. For the case of equal background temperatures, the operator described by Eq. (4.6) is equivalent to the Sugama collision operator [42]. Accordingly, in thermal equilibrium $T_\mathrm{a} = T_\mathrm{b}$, the test and field particle

operators satisfy adjointness relations

$$\int d\mathbf{v} \frac{\delta f_\mathrm{a}}{f_\mathrm{a}^\mathrm{M}} C_\mathrm{T}(\delta g_\mathrm{a}, f_\mathrm{b}^\mathrm{M}) = \int d\mathbf{v} \frac{\delta g_\mathrm{a}}{f_\mathrm{a}^\mathrm{M}} C_\mathrm{T}(\delta f_\mathrm{a}, f_\mathrm{b}^\mathrm{M}), \qquad (4.24)$$

$$T_\mathrm{a} \int d\mathbf{v} \frac{\delta f_\mathrm{a}}{f_\mathrm{a}^\mathrm{M}} C_\mathrm{F}(f_\mathrm{a}^\mathrm{M}, \delta f_\mathrm{b}) = T_\mathrm{b} \int d\mathbf{v} \frac{\delta f_\mathrm{b}}{f_\mathrm{b}^\mathrm{M}} C_\mathrm{F}(f_\mathrm{b}^\mathrm{M}, \delta f_\mathrm{a}), \qquad (4.25)$$

for arbitrary δg_a, and it was shown (see [42], [4] and references therein) that relations Eq. (4.24) and Eq. (4.25) ensure that the operator Eq. (4.6) satisfies the H-theorem for case of equal temperatures of colliding species. In the case of different background temperatures, $T_\mathrm{a} \neq T_\mathrm{b}$, the operator given by Eq. (4.6) is no longer equivalent to the Sugama [42] operator. This is because the latter operator does not include collisions between the Maxwellian backgrounds, and modifies the test particle term in order to ensure that the self-adjointness relation in Eq. (4.24) holds for unequal temperatures. The Sugama model [45] does not include collisional thermalization between the background distribution functions $f_\mathrm{a,b}^\mathrm{M}$. Such an approach is suitable for simulations with fixed backgrounds, but additional care must be taken to avoid energy transfer from the different-temperature Maxwellian $f_\mathrm{a,b}^\mathrm{M}$ backgrounds into the $\delta f_\mathrm{a,b}$ perturbations. Instead, the collision operator can directly retain the energy exchange between background Maxwellians, represented by the $C_\mathrm{T}(f_\mathrm{a}^M, f_\mathrm{b}^M)$ term that drives the system towards an equilibrium temperature $T = T_\mathrm{a} = T_\mathrm{b}$. We note that another approach to a linearized collision operator is used in the GYSELA [66, 44] code, where a term representing the energy exchange between Maxwellians describes the evolution of the background temperatures, and the field particle operator is constructed based on the expansion of a distribution function in spherical harmonics and Laguerre polynomials [44] to recover the friction and thermal forces that will be discussed in Section 4.3 below.

Finally, we note that the long-wavelength approximation adopted in the model collision operator [Eqs. (4.6)-(4.19)] does not account for finite Larmor radius (FLR) effects [45], which, for instance, are required to describe classical transport perpendicular to the magnetic field.

4.2.1 Stable timestep condition

Time integration in COGENT can be done via explicit fourth-order Runge-Kutta (RK4) or semi-implicit additive Runge-Kutta (ARK) scheme. In this section, we analyze the numerical stability condition for the explicit time stepping scheme, arising from the diffusion in velocity space associated with the test particle operator. We illustrate that the diffusion coefficient $D_{\mu\mu}$ along μ grows linearly with the velocity v of colliding species a, and this can cause the maximum stable time step δt of the explicit integration scheme to be much less than the collision time $1/\nu_{\mathrm{ab}}$.

Because Maxwellian distribution $f_{\mathrm{b}}^{\mathrm{M}}$ is spherically symmetric in the velocity space, the Rosenbluth φ_{b}, ψ_{b} potentials associated with the test particle operator are easily found to be

$$\nabla_v^2 \varphi_{\mathrm{b}} = f_{\mathrm{b}}^{\mathrm{M}} \Rightarrow \varphi_{\mathrm{b}} = -\frac{n_{\mathrm{b}}}{4\pi v_{\mathrm{Tb}}} \frac{1}{\zeta} \left(\Omega + \frac{d\Omega}{d\zeta^2} \right), \tag{4.26}$$

$$\nabla_v^2 \psi_{\mathrm{b}} = \varphi_{\mathrm{b}} \Rightarrow \psi_{\mathrm{b}} = -\frac{n_{\mathrm{b}} v_{\mathrm{Tb}}}{8\pi\zeta} \left[(\zeta^2 + 1)\frac{d\Omega}{d\zeta^2} + \left(\zeta^2 + \frac{1}{2} \right) \Omega \right]. \tag{4.27}$$

Probability fluxes $\mathbf{\Pi}$ in Eq. (4.10) can be expressed in drag-diffusion form

$$\Pi^{v_{||}} = A_{v_{||}} f_{\mathrm{a}} + D_{v_{||}\mu} \frac{\partial f_{\mathrm{a}}}{\partial \mu_{\mathrm{a}}} + D_{v_{||}v_{||}} \frac{\partial f_{\mathrm{a}}}{\partial v_{||}}, \tag{4.28}$$

$$\Pi^{\mu} = A_{\mu} f_{\mathrm{a}} + D_{\mu v_{||}} \frac{\partial f_{\mathrm{a}}}{\partial v_{||}} + D_{\mu\mu} \frac{\partial f_{\mathrm{a}}}{\partial \mu_{\mathrm{a}}}, \tag{4.29}$$

with the diffusion coefficients given by [51]

$$\begin{aligned}
D_{v_{||}v_{||}} &= -L^{\mathrm{a/b}} \frac{\partial \psi_{\mathrm{b}}^2}{\partial v_{||}^2} = \frac{1}{2}(\nu_{\mathrm{D}} \frac{2\mu_{\mathrm{a}} B}{m_{\mathrm{a}}} + \nu_{||} v_{||}^2) = \\
&= \frac{\nu_{\mathrm{ab}} v_{\mathrm{Ta}}^3}{2 v_{\mathrm{Tb}}} \left(\sin^2(\xi) \left(\frac{1}{\zeta}\frac{d\Omega}{d\zeta^2} + \frac{\Omega}{\zeta} - \frac{\Omega}{2\zeta^2} \right) + \cos^2(\xi)\frac{\Omega}{\zeta^3} \right),
\end{aligned} \tag{4.30}$$

$$D_{v_{||}\mu} = -L^{a/b}\frac{2m_a}{B}\mu_a\frac{\partial^2\psi_b}{\partial\mu_a\partial v_{||}} = (\nu_{||} - \nu_D)v_{||}\mu_a =$$
$$= \nu_{ab}\frac{v_{Ta}^3 m_a}{2B}\sin^2(\xi)\cos(\xi)\left(\frac{3\Omega}{2\zeta^2} - \Omega - \frac{d\Omega}{d\zeta^2}\right), \tag{4.31}$$

$$D_{\mu\mu} = -L^{a/b}\frac{2m_a^2}{B^2}\mu_a\left(2\mu_a\frac{\partial^2\psi_b}{\partial\mu_a^2} + \frac{\partial\psi_b}{\partial\mu_a}\right) =$$
$$= \frac{m_a v^4}{8B^2}(\nu_D\sin^2(2\xi) + 4\nu_{||}\sin^4(\xi)) = \nu_{ab}\frac{m_a^2 v_{Ta}^3 v_{Tb}}{8B^2} \times \tag{4.32}$$
$$\times\left(\sin^2(2\xi)\left(\zeta\Omega + \zeta\frac{d\Omega}{d\zeta^2} - \frac{\Omega}{2\zeta}\right) + 4\sin^2(\xi)\frac{\Omega}{\zeta}\right),$$

where $\cos(\xi) = v_{||}/v$. Since $\Omega \to 1$ and $d\Omega/d\zeta^2 \to 0$ for $\zeta \to \infty$, it follows from Eq. (4.32) that diffusion $D_{\mu\mu}$ grows unbounded with the velocity v of the species a. Recall that explicit schemes typically have a numerical stability threshold d_{FDA}, setting stable resolution criteria $D_{\mu\mu}\delta t/\delta\mu_a^2 < d_{FDA}$. Therefore, stable timestep δt is bounded by condition

$$\nu_{ab}\delta t \lesssim 2d_{FDA}\left(\frac{2B\delta\mu_a}{m_a v_{Ta}^2}\right)^2\frac{v_{Ta}}{v}, \tag{4.33}$$

where $\delta\mu_a$ is the velocity grid spacing along μ_a. Condition Eq. (4.33) becomes a severe restriction since, on the one hand, the bulk of the Maxwellian function f_a^M needs to be well resolved in the velocity space $\delta v/v_{Ta} \sim 2B\delta\mu_a/m_a v_{Ta}^2 \sim 10^{-1}$, while, on the other hand, superthermal particles (with velocities $v/v_{Ta} \sim 10$ and above) make important contributions to current and heat flux [7] and need to be retained. Note that, unlike $D_{\mu\mu}$, other diffusion coefficients [given by Eqs. (4.30) and (4.31)] are bounded by conditions

$$D_{v_{||}v_{||}} < \frac{\nu_{ab}v_{Ta}^3}{2\sqrt{\pi}v_{Tb}}, \quad D_{v_{||}\mu} < \frac{\nu_{ab}v_{Ta}^3 m_a}{3\sqrt{3}B}, \tag{4.34}$$

and the associated stable timestep conditions are independent of v. Furthermore, recall that the condition in Eq. (4.33) is derived in the $\zeta = v/v_{Tb} \to \infty$ limit, yet, in practice, the

value of ζ is limited by the velocity domain bounds ($|v_\parallel|_{\max}$ and $\mu_{\max}$) of the simulation. Therefore, in general, expressions Eqs. (4.30)-(4.32) must be used to determine the stable timestep condition from the diffusion in velocity space.

4.2.2 Convergence studies

We verify that the operator is implemented correctly by doing a convergence study. We verify that $\mathcal{R}_{ab}$ and $\mathcal{Q}_{ab}$ computed by COGENT from expressions Eqs. (4.18) and (4.19) agree with expressions Eqs. (4.20) and (4.21). To confirm correct implementation of energy and momentum terms given by Eqs. (4.16) and (4.17), we consider an analytically given distribution functions f_a^t (e.g., $f_a^t = (1 + 0.02v_\parallel/v_{Ta} + 0.05v_\parallel^2/v_{Ta}^2)f_a^M$ used in the test shown in Fig. 4.1), and compare analytical (δP_{ab}^t, δE_{ab}^t) values to COGENT (δP_{ab}^Δ, δE_{ab}^Δ) values from simulation with the same velocity domain boundaries $|v_\parallel|_{\max}$ and $\mu_{\max}$, but with different velocity grid cell sizes $\delta v_\parallel$ and $\delta \mu$. In what follows, we label $\delta v_\parallel$ and $\delta \mu$ velocity grid sizes as Δ. We repeat COGENT simulation with different resolutions, simultaneously changing $\delta v_\parallel$ and $\delta \mu_\parallel$ by a factor of two, and measure the residue as shown in Fig. 4.1 to verify that $|\delta E_{ab}^t - \delta E_{ab}^\Delta| \propto (\Delta/\Delta_0)^2$ and $|\delta P_{ab}^t - \delta P_{ab}^\Delta| \propto (\Delta/\Delta_0)^2$, where Δ_0 is the velocity grid cell size for the COGENT simulation with the velocity resolution $(v_\parallel, \mu)$ of 1024×512, as illustrated in Fig. 4.1. This quadratic rate of convergence is consistent with a second-order cell-centered finite-volume discretization presently utilized for the newly implemented collision operator Eq. (4.6) in COGENT. We also verified that COGENT satisfies both the particle conservation

$$\int d\mathbf{v}C(f_a, f_b) = 0, \tag{4.35}$$

and the momentum balance

$$\int d\mathbf{v}m_a v_\parallel C(f_a, f_b) + \int d\mathbf{v}m_b v_\parallel C(f_b, f_a) = 0, \tag{4.36}$$
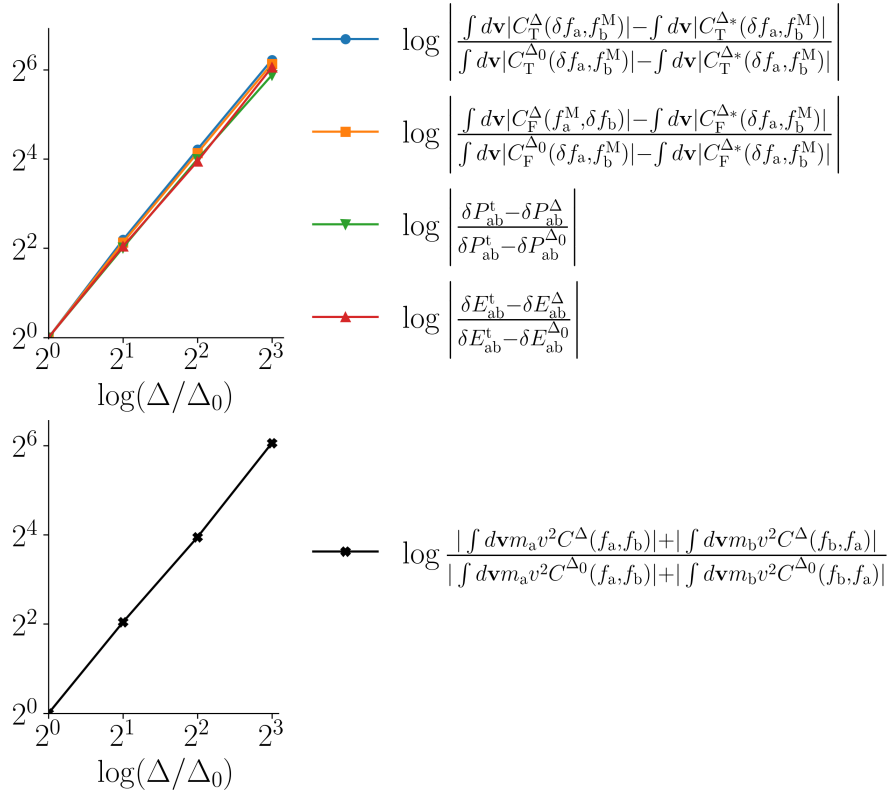
Figure 4.1. (Top panel) Example results from the convergence studies, with $f_{\mathrm{a}} = (1 + 0.02 v_{\|}/v_{\mathrm{Ta}} + 0.05 v_{\|}^2/v_{\mathrm{Ta}}^2) f_{\mathrm{a}}^{\mathrm{M}}$, demonstrating quadratic convergence. Grid cells Δ/Δ_0 correspond to $(v_{\|}, \mu)$ resolutions 1024×512, 512×256, 256×128, and 128×64, where Δ_0 corresponds to 1024×512. Grid cell size Δ_* corresponds to $(v_{\|}, \mu)$ resolution of 2048×1024. All shown simulations have the same velocity domain boundaries $\mu_{\max}$ and $|v_{\|}|_{\max}$ given by $2B\mu_{\max}/T_{\mathrm{a}} = 27$ and $|v_{\|}|_{\max}/v_{\mathrm{Ta}} = 8$. (Bottom panel) Example results of the energy conservation error in simulations which include collisions between background collisions. The resolution of the velocity domain corresponds to the data on the top panel.

up to numerical precision, regardless of the velocity domain resolution. The particle conservation Eq. (4.35) is obtained by setting the probability flux through the $|v_{||}|_{\max}$ and $\mu_{\max}$ boundaries to zero, as in Eq. (4.23).

The energy conservation

$$\int d\mathbf{v} \frac{m_\mathrm{a} v^2}{2} C(f_\mathrm{a}, f_\mathrm{b}) + \int d\mathbf{v} \frac{m_\mathrm{b} v^2}{2} C(f_\mathrm{b}, f_\mathrm{a}) = 0 \tag{4.37}$$

is demonstrated in the bottom panel of Fig. (4.1) as a function of the velocity grid resolution. Note that the error in energy conservation comes entirely from the terms describing the background Maxwellian interactions, i.e., $C_\mathrm{T}(f_\mathrm{a}^\mathrm{M}, f_\mathrm{b}^\mathrm{M})$ and $C_\mathrm{T}(f_\mathrm{b}^\mathrm{M}, f_\mathrm{a}^\mathrm{M})$. When background Maxwellians are in the thermal equilibrium, the corresponding collision term vanishes $C_\mathrm{T}(f_\mathrm{a}^\mathrm{M}, f_\mathrm{b}^\mathrm{M}) = 0$ and can be excluded from the operator, resulting in energy conservation up to machine precision for all velocity resolutions.

Recall that the denominators of the $\mathcal{R}_\mathrm{ab}$ and $\mathcal{Q}_\mathrm{ab}$ terms of the field operator in Eqs. (4.18) and (4.19) are designed to balance momentum and energy loss caused by the test particle operator for species b , as illustrated in Eq. (4.22). To recover the corresponding discretized energy and momentum conservation properties (Eqs. (4.36, 4.37)) up to numerical precision, we employ numerical evaluation and integration of the denominators in expressions Eqs. (4.18) and (4.19), instead of evaluating them analytically as in Eq. (4.20) and (4.21).

4.3   COGENT simulations in the highly collisional regime

In this section, we use the model collision operator to simulate transport in case of high mass ratio $m_\mathrm{b} \gg m_\mathrm{a}$ and for high enough collisionality to assume small deviations from a Maxwellian distribution for colliding species a and b, justifying the use of a linearized collision operator. Collisions in such regime produce thermal and friction

forces, as was demonstrated by Braginskii [6] for electron-ion plasma. In what follows, background Maxwellian distributions are fixed and have equal temperature $T_{\mathrm{a}} = T_{\mathrm{b}} = T$, so $C_{\mathrm{T}}(f_{\mathrm{a}}^{\mathrm{M}}, f_{\mathrm{b}}^{\mathrm{M}}) = 0$.

The friction force along the magnetic field, resulting from operator Eq. (4.6), can be expressed as

$$\int d\mathbf{v} m_{\mathrm{a}} v_{||} C(f_{\mathrm{a}}, f_{\mathrm{b}}) = \delta P_{\mathrm{ab}} - \delta P_{\mathrm{ba}}, \tag{4.38}$$

with δP_{ab} and δP_{ba} defined by Eq. (4.16).

Our first goal is to verify that, in linear approximation, the friction force Eq. (4.38) from the model operator agrees with the result from Braginskii's [6] original work. We consider the bulk velocities of electrons u_{a} and ions u_{b} (relative to the velocity of background Maxwellians $f_{\mathrm{s}}^{\mathrm{M}}$) to be much less than their thermal speeds v_{Ts}. We follow Braginskii's approach and compute the friction force on light species by approximating the distribution function to first order as

$$f_{\mathrm{a}} \approx f_{\mathrm{a}}^{\mathrm{M}} \left(1 + \frac{2\mathbf{u}_{\mathrm{a}}\mathbf{v}}{v_{\mathrm{Ta}}} \right). \tag{4.39}$$

Since for the test particle collision operator the energy transfer rate between the light species a and the heavy species b is a factor of $m_{\mathrm{a}}/m_{\mathrm{b}}$ smaller than the momentum transfer rate, we can calculate the δP_{ba} as

$$\delta P_{\mathrm{ba}} = \int d\mathbf{v} \frac{m_{\mathrm{a}} v_{||} n_{\mathrm{b}} L^{\mathrm{a/b}}}{8\pi} \frac{\partial}{\partial v_{\alpha}} \frac{v^2 \delta_{\alpha\beta} - v_{\alpha} v_{\beta}}{v^3} \frac{\partial \delta f_{\mathrm{a}}}{\partial v_{\beta}} =$$
$$= \frac{n_{\mathrm{b}} m_{\mathrm{a}} L^{\mathrm{a/b}}}{2\pi} \int d\mathbf{v} \frac{v_{||}}{v^3} \frac{u_{\mathrm{a}\beta} v_{\beta}}{v_{\mathrm{Ta}}^2} f_{\mathrm{a}}^{\mathrm{M}} = \frac{4\nu_{\mathrm{ab}} m_{\mathrm{a}} n_{\mathrm{a}}}{3\sqrt{\pi}} u_{\mathrm{a}}. \tag{4.40}$$

The δP_{ba} obtained in Eq. (4.40) depends on the u_{a}, yet it is clear from the physics of the Coulomb collisions that the friction force must depend on the relative bulk velocity

$u_a - u_b$. Therefore, the contribution from δP_{ab} must also be considered. To calculate δP_{ab}, we use the Landau form of the test particle operator given by Eq. (4.7) in the expression Eq. (4.16), and expand the relative velocity tensor defined in Eq. (4.8) to first order as

$$U_{\alpha\beta} \approx \frac{v'^2 \delta_{\alpha\beta} - v'_\alpha v'_\beta}{v'^3} + v_\gamma \frac{\partial}{\partial v'_\gamma}\left(\frac{v'^2 \delta_{\alpha\beta} - v'_\alpha v'_\beta}{v'^3}\right), \tag{4.41}$$

with the ratio between the velocities of species b and a as the expansion parameter. Combining Eqs. (4.7), (4.16) and (4.41), we can evaluate δP_{ab} as

$$\begin{aligned}
\delta P_{ab} &= \int d\mathbf{v} m_b v_{\parallel} \frac{m_b L^{b/a}}{8\pi} \frac{\partial}{\partial v_\alpha} \int d\mathbf{v}' \frac{\delta f_b(\mathbf{v})}{m_a} \frac{\partial f_a^M(\mathbf{v}')}{\partial v'_\beta} \left\{ \frac{v'^2 \delta_{\alpha\beta} - v'_\alpha v'_\beta}{v'^3} + \right. \\
&\left. + v_\gamma \frac{\partial}{\partial v'_\gamma}\left(\frac{v'^2 \delta_{\alpha\beta} - v'_\alpha v'_\beta}{v'^3}\right) \right\} = -\frac{m_b^2 L^{b/a}}{8\pi m_a} \int d\mathbf{v} \delta f_b v_{\parallel} \int d\mathbf{v}' \frac{v'^2 \delta_{\alpha\beta} - v'_\alpha v'_\beta}{v'^3} \frac{\partial f_a^M}{\partial v'_\beta \partial v'_{\parallel}} = \\
&= \frac{4}{3\sqrt{\pi}} \nu_{ba} \sqrt{\frac{m_a}{m_b}} m_b n_b u_b,
\end{aligned} \tag{4.42}$$

where

$$u_b = \frac{1}{n_b} \int d\mathbf{v} \delta f_b v_{\parallel}. \tag{4.43}$$

Combining expressions Eq. (4.40) and Eq. (4.42) above, we find that the linear approximation for friction force

$$\begin{aligned}
\int d\mathbf{v} m_a v_{\parallel} C(f_a, f_b) &= \delta P_{ab} - \delta P_{ba} = \\
&= \frac{4\nu_{ab} m_a n_a}{3\sqrt{\pi}} (u_b - u_a) = -\int d\mathbf{v} m_b v_{\parallel} C(f_b, f_a).
\end{aligned} \tag{4.44}$$

matches the result of Braginskii. This is to be expected, since, in the infinite mass ratio $m_b/m_a \to \infty$ limit, the operator described by Eq. (4.6) is the same as the Landau operator. Indeed, the test particle $C_T(\delta f_a, f_b^M)$ operator in this limit reduces to the Lorentz operator,

while the field particle operator vanishes for infinitely heavy species b.

4.3.1 Modeling electric conductivity with COGENT

We now simulate the friction force in COGENT with the setup described in this paragraph. For simplicity, we consider a slab geometry with two species (a and b), which are initialized with uniform Maxwellian distributions f_a^M and f_b^M, respectively. We set masses of colliding species to $m_a = m_p$, $m_b = 100 m_p$ in the units of proton mass m_p. The charge of species a is set equal to the electron charge, $e_a = -|e|$. The charge of the heavy species $e_b = Z_b|e|$ is varied between simulations. The density n_a of species a is set to $10^{21} \ m^{-3}$, and the density n_b of species b is set by the quasi-neutrality condition,

$$e_a n_a + e_b n_b = 0. \tag{4.45}$$

The temperature of both species is homogeneous and set to 20 eV. We consider a slab geometry with a uniform fixed magnetic $B\mathbf{e}_z$ and electric $E\mathbf{e}_z$ fields along the z-axis, and periodic boundary conditions in the z-direction. For the outlined simulation setup, the kinetic equation Eq. (4.1) solved in COGENT for the species a reduces to

$$\frac{\partial f_a}{\partial t} + \frac{e_a E}{m_a} \frac{\partial f_a}{\partial v_{||}} = C(f_a) + C(f_a, f_b). \tag{4.46}$$

Collisions $C(f_a, f_b)$ between species a and species b are modeled using the operator described in Section 4.2. Note that, for a finite charge e_b of species b, the impact of collisions $C(f_a)$ between light species a on their distribution function f_a is compatible to the impact of the collisions between species a and b, $C(f_a, f_b) \sim C(f_a)$. Therefore, collisions between species a must be included into the simulation with finite charge state of species b, $Z_b \sim 1$. Various like-species collision models are available [67] in the COGENT code, including the full Fokker-Planck [51] collision operator $C_{FP}(f_a)$, and a model collision

operator $C_A(f_a)$ proposed by Abel [68] that is similar to the operator $C(f_a, f_b)$ described in Section 4.2 (both $C_A(f_a)$ and $C(f_a, f_b)$ are based on the linearized Landau collision operator). As we mentioned earlier, the Fokker-Planck operator gives the highest fidelity, but is expensive to evaluate numerically since it requires solving a pair of Poisson equations [51] for the Rosenbluth potentials. Therefore, it is of interest to assess the impact of replacing the Fokker-Planck operator $C_{FP}(f_a)$ with the Abel collision operator $C_A(f_a)$, which is much faster to evaluate. The use of a linearized collision model in the considered simulations can be justified for the case where the magnitude of the electric field E is much less than the Dreicer [69] field E_D. Because the role of electrons is assumed here by the species a with a mass of a proton, the corresponding Dreicer [69] field is $E_D \sim 1$ kV/m. For $E \ll E_D$ and homogeneous background profiles, the deviations from the Maxwellian can be assumed to be small and the use of linearized collision operators is justified. In what follows, we perform two sets of COGENT simulations, where the like-species collisions of the light species a are described with either the Fokker-Planck, C_{FP}, or the model Abel operator, C_A. In addition to verification purposes, this test elucidates validity limits of the reduced Abel operator.

We simulate the described setup in COGENT over hundred collision times $1/\nu_{ab}$, allowing the bulk velocities

$$u_b \equiv \frac{1}{n_b} \int d\mathbf{v} v_{||} \delta f_b = -\frac{Z_b m_a}{Z_a m_b} u_a, \tag{4.47}$$

$$u_a \equiv \frac{1}{n_a} \int d\mathbf{v} v_{||} \delta f_a, \tag{4.48}$$

to reach a steady state. Note that the right equality in Eq. (4.47) follows from the quasi-neutrality condition Eq. (4.45) and momentum conservation Eq. (4.36). We then

analyze the kinetic simulation results with the Braginskii [6] fluid model,

$$m_s n_s \frac{du_s}{dt} + \frac{\partial P_s}{\partial z} = e_s n_s E + R_s, \tag{4.49}$$

$$\frac{3}{2} n_s \frac{dT_s}{dt} + P_s \frac{\partial u_s}{\partial z} = -\frac{\partial q_s}{\partial z} + Q_s, \tag{4.50}$$

where $P_s = n_s T_s$ is the pressure, Q_s is the heat from friction given for species a as

$$Q_a = \int d\mathbf{v} \frac{m_a v^2}{2} C(f_a, f_b), \tag{4.51}$$

$R_s = R_{u,s} + R_{T,s}$ is the parallel force combined from friction $R_{u,s}$ and thermal $R_{T,s}$ forces expressed for species a as

$$R_a = \int \mathbf{d}v m_a u_\| C(f_a, f_b) = R_{u,a} + R_{T,a} =$$
$$= -C_1 \frac{4\nu_{ab} m_a n_a}{3\sqrt{\pi}} (u_a - u_b) - C_2 n_a \nabla_\| T_a, \tag{4.52}$$

and q_s is the parallel heat flux expressed for a species as

$$q_a = \int d\mathbf{v} \frac{m_a}{2} (\mathbf{v} - u_a \mathbf{e_z})^2 (v_\| - u_a) f_a = q_{u,a} + q_{T,a} =$$
$$= C_2 n_a T_a (u_a - u_b) - C_3 \frac{3\sqrt{\pi} n_a T_a}{4 m_a \nu_{ab}} \nabla_\| T_a. \tag{4.53}$$

The transport coefficients C_1, C_2, C_3 depend on details of a collision model and can be inferred from the results of COGENT simulation. It is important to emphasize that the thermal force $R_{T,a}$ arises from the velocity dependence of the Coulomb collisions $\lambda \sim (\mathbf{v_a} - \mathbf{v_b})^4$, and the unlike-species collision operator must recover this dependence in order to recover the thermal force in Eq. (4.52). For example, the thermal force $R_{T,a}$ in Eq. (4.52) cannot be recovered from Bhatnagar-Gross-Krook (BGK) [70] collision operator $C_{BGK}(f) = \nu(f - f^M)$ with ν independent of a particle velocity. Indeed, the force produced

74

by BGK operator is

$$\int \mathbf{v} C_{\text{BGK}}(f) d\mathbf{v} = \nu \left(\int \mathbf{v} f d\mathbf{v} - \int \mathbf{v} f^{\text{M}} d\mathbf{v} \right), \quad (4.54)$$

which depends solely on the bulk velocities of distributions f and f^{M} and does not depend on temperature gradients. Likewise, the thermal force $R_{\text{T,a}}$ is not recovered by the Lenard-Bernstein-Dougherty (LBD) [71, 72] operator of the form

$$C_{\text{LBD}}(f_{\text{a}}) = L \frac{\partial}{\partial v_\alpha} \left[(\mathbf{v} - \mathbf{V}^{\text{LBD}}) f_{\text{a}} + D_{\alpha\beta}^{\text{LBD}} \frac{\partial f_{\text{a}}}{\partial v_\beta} \right], \quad (4.55)$$

where L, V^{LBD} and D^{LBD} are some functions independent of velocity, as in, for example, recently reported GKeyll [46] or GENE-X [47] implementations. Indeed, the force from the C_{LBD} collision operator, described in Eq. (4.55), is

$$\int \mathbf{v} C_{\text{LBD}}(f_{\text{a}}) d\mathbf{v} = -L \left(\int \mathbf{v} f_{\text{a}} d\mathbf{v} - \mathbf{V}^{\text{LBD}} \right), \quad (4.56)$$

and in order for this expression to recover the thermal force $R_{\text{T,a}}$ from expression (4.52) would require for the $\mathbf{V}^{\text{LBD}}$ function to have a particular explicit $\nabla_\parallel T$ dependence. Current LBD implementations often [47, 46] disregard the thermal force entirely, despite this force being important [53] for the impurity transport.

The multi-species collision operator given by Eq. (4.6) is based on the test particle operator C_{T} which preserves the velocity dependence of Coulomb collisions, and therefore can recover the thermal force. For simulations described in Sections 4.3.1 and 4.3.2, we measure the parallel force R_{a} and the heat flux q_{a}, verify that they have the forms given by Eq. (4.52) and Eq. (4.53), and compute the transport coefficients $C_{1,2,3}$.

For the simulation setup with a fixed electric field described above, a steady-state solution corresponds to a balance between the parallel force R_{a} and the electric force

$e_a n_a E$ [see Eqs.(4.49) and (4.52)], giving

$$C_1 = \frac{3\sqrt{\pi}|e_a|E}{4\nu_{ab}m_a n_a|u_a - u_b|}. \tag{4.57}$$

From simulation without a-a collisions, we obtain $C_1 = 0.30$ from Eq. (4.57). This value is very close to the value $C_1^B = 0.29$ reported by Braginskii for the case of an electron-ion plasma with $Z_b \to \infty$. Such agreement is expected since $Z_b = e_b/|e| \to \infty$ allows to neglect electron-electron collisions in the electron-ion problem, and electrons correspond to the species a in the described simulation. For finite Z_b, collisions between the light species a must also be included in the corresponding COGENT simulation. We use Eq. (4.57) to measure the transport coefficient in COGENT simulations with various values of e_b and compare them to the corresponding results from the Braginskii's problem for an electron-ion plasma [6, 56], as shown in the top and bottom left panel in Fig. 4.2. We also perform several additional runs with different values of the electric field, E, to verify that the measured force is proportional to $u_a - u_b$, in agreement with the expression for the friction force $R_{u,a}$ in Eq. (4.52). These runs are illustrated in the bottom right panel in Fig. 4.2. When the Fokker-Planck operator $C_{FP}(f_a)$ is used to model collisions between the species a, the values of C_1 are within $3 - 6\%$ of Braginskii's results for all Z_b. Recall that the difference between the newly implemented operator Eq. (4.6) and the linearized Landau operator vanishes in the limit of high mass ratios, justifying the observed agreement with Braginskii's results for the electron ion plasma since $m_e \ll m_i$. Furthermore, in simulations where the Abel collision operators $C_A(f_a)$ is used instead of the Fokker-Planck $C_{FP}(f_a)$ operator, the values of C_1 are within 20% of Braginskii's results. When using the model collision operator $C_A(f_a)$ for the like-species collisions, the difference with the values reported by Braginskii is the largest for the smallest charge of species b, $Z_b = 1$, which is to be expected since, for higher charge state Z_b, the influence of like-species collisions on the light species distribution function f_a decreases relative to

the influence of collisions between the light species a and the heavy species b.

4.3.2 Thermal force and heat flux coefficients measurement with COGENT

The heat flux q_a for species a is given by Eq. (4.53) in the Braginskii model presented above. We use Eq. (4.53) to measure C_2 in the simulation setup from Section 4.3.1 as

$$C_2 = \frac{q_a}{n_a T (u_a - u_b)}, \tag{4.58}$$

and present the results in Fig. 4.2. For the simulation corresponding to $Z_b \to \infty$ (i.e., without self-collisions of species a), Eq. (4.58) gives $C_2 = 1.44$, which is close to the heat flux coefficient value of $C_2^B = 1.5$ reported by Braginskii for the electron-ion problem. For the simulations corresponding to finite Z_b, the values of C_2 are within 3-6% of Braginskii's results for the case where the Fokker-Planck operator $C_{FP}(f_a)$ is used to simulate collisions between the light species a, as shown in Fig 4.2. When the Fokker-Planck operator is replaced by the Abel linearized collision operator $C_A(f_a)$, the observed C_2 values are within 20% of Braginskii's results.

Our next goal is to consider a hydrodynamic equilibrium in the presence of the temperature gradient along the magnetic field, to measure the thermal $R_{T,a}$ force in Eq. (4.52) and the $q_{T,a}$ component of the parallel thermal flux in Eq. (4.53). We do this in the rest of this section.

We consider a slab geometry introduced in Sec. 4.3.1, although we turn off the electric field. For the outlined simulation setup, the kinetic equation Eq. (4.1) solved by COGENT for the species a can then be simplified to

$$\frac{\partial f}{\partial t} + \frac{\partial}{\partial z}(v_{\parallel} f_a) = C(f_a) + C(f_a, f_b), \tag{4.59}$$

where z is the coordinate along the magnetic field. We set the initial temperature profile
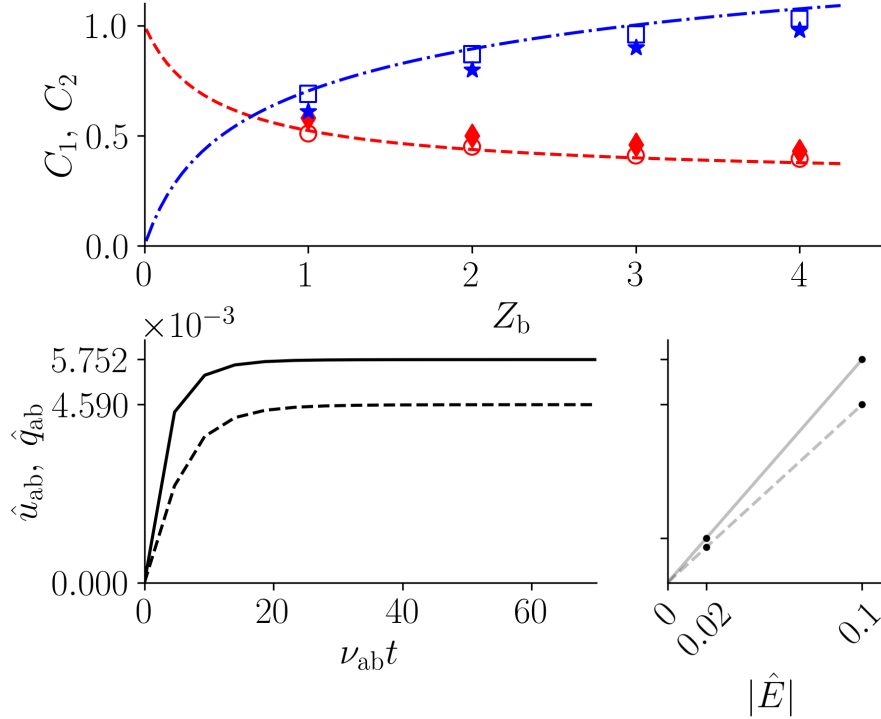
Figure 4.2. (Top panel): Values of transport coefficients C_1 (red circle and diamond labels) and C_2 (blue square and star labels) from COGENT simulation of the setup described in Section 4.3.1, measured using Eq. (4.57) and Eq. (4.58) for various e_b. The red dashed line and blue dash-dot line show Braginskii's values [6, 56] for electron-ion transport coefficients C_1 and C_2, respectively. For simulations with Abel collision operator $C_A(f_a)$ for collisions between species a, the transport coefficients C_1 (diamonds) and C_2 (stars) are within 20% of the Braginskii's values. When the Fokker-Planck operator is used to model a-a collisions, agreement of C_1 (circles) and C_2 (squares) with Braginskii's results is within $3 - 6\%$.

(Bottom left panel): Time series of the bulk velocity u_a (solid line) and heat flux q_a (dashed line) for simulation with $e_b = 2|e|$, illustrating the steady state. (Bottom right panel) Scaling of steady state velocity (top line) and heat flux (bottom line) from COGENT simulations with different E, demonstrating that steady state bulk velocity and heat flux scale linearly with E, in agreement with theory. Velocity is normalized by v_{Ta}, heat flux by $n_a T_a v_{\mathrm{Ta}}$, distance by $\tilde{l} = 1$ m and electric field by $T_a/(|e|\tilde{l})$. The simulation has velocity domain boundaries $|v_{||}|_{\max}/v_{\mathrm{Ta}} = 8$, $\mu_{\max}B/T_a = 12$, and velocity grid resolution $n_{v_{||}} = n_\mu = 128$.
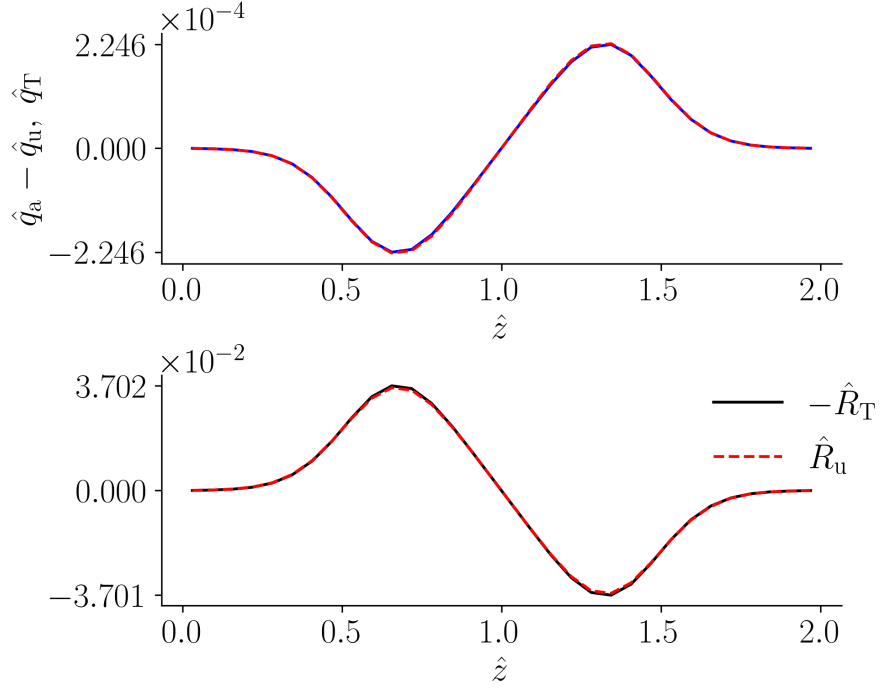
Figure 4.3. (Top panel): Profiles of the thermal heat flux $q_{\mathrm{T,a}}$ and residue $\mathbf{q}_\mathrm{a} - \mathbf{q}_\mathrm{u}$, as defined in Eq. (4.53).
(Bottom panel) profiles of the pressures from friction R_u and thermal R_T forces at steady state, demonstrating $|u_\mathrm{a} - u_\mathrm{b}| \propto \nabla_{||}T$ in agreement with Eq. (4.52). Velocity is normalized by v_{Ta}, heat flux by $n_{\mathrm{a,0}}T_\mathrm{a}v_{\mathrm{Ta}}$, distance by $\tilde{l} = 1$ m, pressure by $n_{\mathrm{a,0}}m_\mathrm{a}v_{\mathrm{Ta}}^2/\tilde{l}$. The simulated velocity grid is bounded by $|v_{||}|_{\max}/v_{\mathrm{Ta}} = 8$, $\mu_{\max}B/T_\mathrm{a} = 12$ and has resolution $n_{\mathrm{v}_{||}} = n_\mu = 128$. Domain resolution along the magnetic field is $n_\mathrm{z} = 32$.
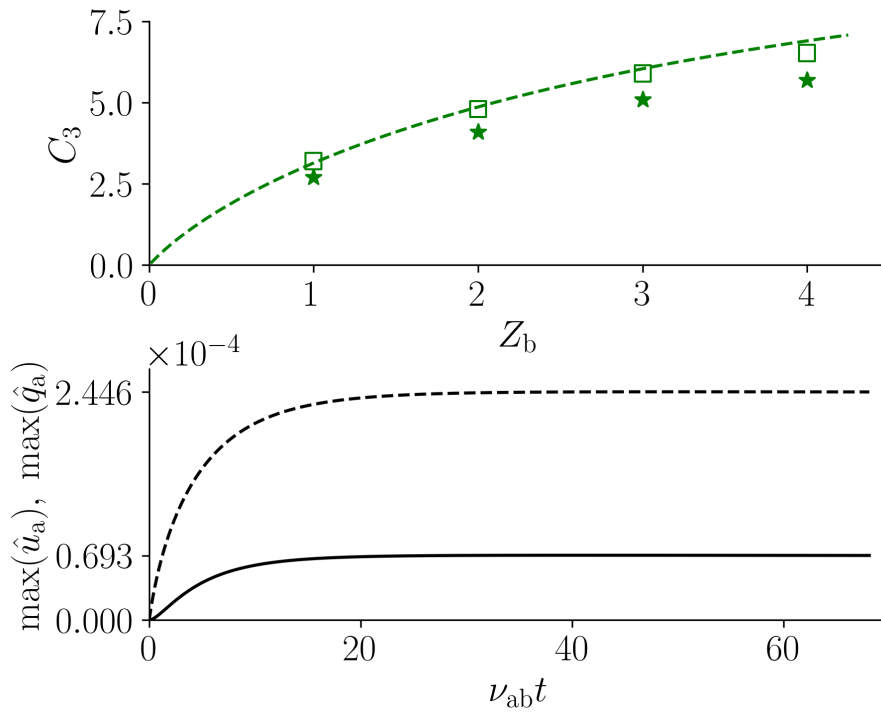
Figure 4.4. (Top panel): Values of the conductive heat flux coefficient C_3 (green labels) from COGENT simulation of the setup described in Section 4.3.2, measured using Eq. (4.53) for various e_b. The green dashed line shows the heat flux coefficient C_3 reported by Braginskii [6, 56]. Simulations with Abel like-species collision operator $C_A(f_a)$ are labeled with stars and agree within 20% of the Braginskii's values. When the Fokker-Planck C_{FP} operator is used instead to model the like-species collisions, the agreement of C_3 values (squares) with Braginskii's results is improved to within $3 - 6\%$.

(Bottom panel) Time series of relative velocity $\hat{u} = |\hat{u}_a - \hat{u}_b|$ (solid lines), and heat flux (dashed lines) $\hat{q}_a$ from simulation with $e_b = 3|e|$, illustrating the steady state. Velocity is normalized by v_{Ta}, heat flux by $n_{a,0}T_a v_{Ta}$.

for both species as

$$\frac{T_{\rm s}}{T_{\rm s,0}} = 1.05 - 0.05 \left(1 + \exp\left(2\pi \frac{z - z_{\rm min}}{z_{\rm max} - z_{\rm min}} - \pi \right) \right)^{-1}, \tag{4.60}$$

where $T_{\rm s,0} = 20$ eV, $z_{\rm min} = 0$ m and $z_{\rm max} = 2$ m. The density profile for each species is set to $n_{\rm s,0}T_{\rm s,0}/T_{\rm s}$ so that the system is in hydrodynamic equilibrium $\nabla p_{\rm s} = 0$. We take $n_{\rm a,0} = 5 \times 10^{21}$ m^{-3} and $n_{\rm b,0}$ is set by the quasi-neutrality condition given by Eq. (4.45). The masses of species are set to $m_{\rm a} = m_{\rm p}$ and $m_{\rm b} = 100m_{\rm p}$ as in the setup from the previous section, $e_{\rm a} = -|e|$, and the value of $e_{\rm b}$ is varied between the simulations. COGENT simulations demonstrate that the bulk velocities and heat fluxes reach their quasi-stationary state values after about a dozen of collisional times. In this quasi-stationary state, the thermal force, $R_{\rm T,a}$, should be balanced by the friction force, $R_{\rm u,a}$, according to Eqs. (4.49) and (4.52). This property is confirmed in our simulations, as illustrated in Fig. 4.3 and bottom panel of Fig. 4.4. From Eq. (4.52) and $R_{\rm u,a} + R_{\rm T,a} = 0$, we can measure the C_1/C_2 ratio. For example, for $Z_{\rm b} = 3$, in the simulation with the Abel collision operator $C_{\rm A}$, we recover the ratio $C_2/C_1 = 1.92$. Recall that we previously measured $C_1 = 0.46$ and $C_2 = 0.9$ for the case of $Z_{\rm b} = 3$ in the counterpart simulation which included external electric field (see Sec. 4.3.1). For that case, we obtained the transport coefficients from the steady-state values of the friction force (C_1) and the heat flux (C_2). It is instructive to note that the ratio of those coefficients $C_2/C_1 = 1.96$ is within 2% from what we obtain here from the force balance. This is a manifestation of the Onsager symmetry in the transport coefficient. The Onsager principle follows from $(t, B) \rightarrow (-t, -B)$ invariance of underlying equations of motion and yields the transport coefficient for the convective heat flux [the first term in the right-hand side of Eq. (4.53)] to be the negative of the transport coefficient for the friction force [the second term in the right-hand-side of Eq. (4.52)]. This principle is represented in the self-adjointness relations Eqs. (4.24) and (4.25) of the collision operator (see [4] and references therein). Note that the Onsager property is related to the entropy

production [4] rate. Therefore, model operators which do not recover Onsager symmetry do not, in general, result in the correct rate of entropy production, which can be important [73] for kinetic studies. The model operator in Eq. (4.6) does recover Onsager symmetry for the case $T_a = T_b$ considered here, and we verify that the C_2/C_1 ratio measured from the two different setups described in Secs. 4.3.1 and 4.3.2 agree within 2% for all Z_b we simulated. We can therefore use the value of C_2 obtained from Eq. (4.58) to measure the transport coefficient C_3 in the Eq. (4.48) as illustrated in the top panel of Fig. 4.3. Without the like-species collisions for species a, we obtain $C_3 = 12.4$, which recovers Braginskii's value $C_3^B = 12.5$ for the $Z_b \to \infty$ case in the electron-ion problem. Similarly to previous results, when we use the Fokker-Planck operator $C_{FP}(f_a)$ to simulate collisions between the light species a, the values of the conductive heat flux coefficient C_3 from COGENT simulations are within $3 - 6\%$ of Braginskii's result for all Z_b, as illustrated in the top panel of Fig. 4.4. In the corresponding simulations with the Abel collision operator $C_A(f_a)$, we obtain C_3 values within 20% of Braginskii's result.

In summary, in this section we performed simulations using COGENT with the model collision operator given by expression Eq. (4.6) to measure the parallel transport coefficients $C_{1,2,3}$ in a strongly collisional regime for a two-component plasma with a large species mass ratio $m_a/m_b = 1/100$. For the case where the Fokker-Planck operator $C_{FP}(f_a)$ is used to model the like-species collisions for the light species a, the results of the COGENT simulations for all transport coefficients are found to be in good agreement (within 3-6%) with Braginskii's results for an electron-ion plasma. For the case where the linearized Abel operator $C_A(f_a)$ is used to model a-a collisions, the departure from Braginskii's results increases to 20%. The maximum difference is observed for smaller values of Z_b, consistent with a pronounced role of the like-species collisions for $Z_b \sim 1$. We also verified that the Onsager symmetry relationship is recovered in our simulations for the case of equal $T_a = T_b$, as expected from the self-adjointness of the model unlike collision operator.

It is expected that the model unlike-species collision operator given by Eq. (4.6) does not, in general, yield physically accurate transport coefficient outside the high mass ratio limit addressed in this section, since the error from the ad-hoc field particle operator is significant for $m_a \sim m_b$. This limitation can be addressed by utilizing the moment method [74] to further improve a linearized collision model, as proposed by Sugama in Ref. [43].

4.3.3 Modeling radial neoclassical transport in the presence of heavy impurities with COGENT

In this section, we consider a plasma of electrons, ions, and heavy impurities in a concentric circular tokamak geometry. The magnetic field geometry is given by

$$B_{\phi,\theta}(r,\theta) = \frac{B_{\mathrm{T,p}}R_0}{R_0 + r\cos(\theta)}, \tag{4.61}$$

where r is the minor radius coordinate, θ is the poloidal angle, B_T and B_p are the toroidal and poloidal components of the magnetic field. We take the major radius of the tokamak to be $R_0 = 8.5$ m. The minor radius coordinate ranges from $r_{\min} = 0.8075$ m to $r_{\max} = 0.8925$ m, so the middle of the simulation domain is located at $r_0 = (r_{\min}+r_{\max})/2 = 0.85$ m and the tokamak aspect ratio is $\epsilon = r_0/R_0 = 0.1$ We consider plasma transport in a Pfirsch-Schlüter regime, i.e., for collisionality

$$\nu^* = \frac{\nu_{\mathrm{ab}}\epsilon^{-3/2}qR_0}{v_{\mathrm{Tb}}} \gg 1, \tag{4.62}$$

where $q \sim \epsilon B_{\mathrm{T}}/B_{\mathrm{p}} \sim 1.14$ is the characteristic safety factor, ν_{ab} is the collision frequency defined in Eq. (4.14), main plasma ions are denoted as species a with mass $m_a = m_{\mathrm{p}}$ and charge $e_a = |e|$, and impurities are denoted as species b with $m_b = 100m_{\mathrm{p}}$ and charge $e_b = 2|e|$. We simulate a strongly magnetized plasma by taking $B_{\mathrm{T}} = 28.9$ T, $B_{\mathrm{p}} = 2.53$ T, and assuming the background temperature $T = 500$ eV for all species. Initial condition for

f_a and f_b correspond to a local Maxwellian distribution function with uniform temperature and a density profiles given by

$$n_s = n_{s,0} \left(1 - 0.05 \tanh \left(2\pi \frac{r - r_{\min}}{r_{\max} - r_{\min}} - \pi \right) \right), \tag{4.63}$$

where $n_{a,0} = 2.8 \times 10^{20}$ m^{-3} and $n_{b,0} = 7 \times 10^{19}$ m^{-3}. These plasma parameters correspond to $\nu^* \approx 34 \gg 1$. For the outlined parameters, plasma is strongly magnetized, with the gyroradius much smaller than the mean free path $\rho_a \ll \lambda_a$.

The electron density is described by the linear Boltzmann response as

$$n_e = \langle n_a + Z_b n_b \rangle \left(1 + \frac{e\Phi}{T} - \frac{e\langle \Phi \rangle}{T} \right), \tag{4.64}$$

where the angular brackets represent the flux surface average

$$\langle f \rangle = \oint f \frac{dl_\theta}{B_\theta} \bigg/ \oint \frac{dl_\theta}{B_\theta}. \tag{4.65}$$

In contrast to the slab geometry simulations presented in Secs. 4.3.1 and 4.3.2, here we also evolve the electric field. This is done in COGENT by including the gyrokinetic Poisson equation [67, 75] in the long-wavelength limit

$$\sum_s \frac{4\pi e_s^2}{m_s \Omega_s^2} \nabla_\perp \cdot (n_s^{\mathrm{gc}} \nabla_\perp \Phi) = 4\pi e \left(n_e - \sum_s n_s^{\mathrm{gc}} \right), \tag{4.66}$$

where $\Omega_s = e_s B / m_s c$ is the gyrofrequency, n_s^{gc} is the gyrocenter density given by

$$n_s^{\mathrm{gc}} = \frac{2\pi}{m_s} \int B_{\|s}^* f_s dv_\| d\mu_s, \tag{4.67}$$

and $\nabla_\perp = \nabla - \mathbf{b}(\mathbf{b} \cdot \nabla)$. The radial boundary conditions for the Poisson equation Eq. (4.66)
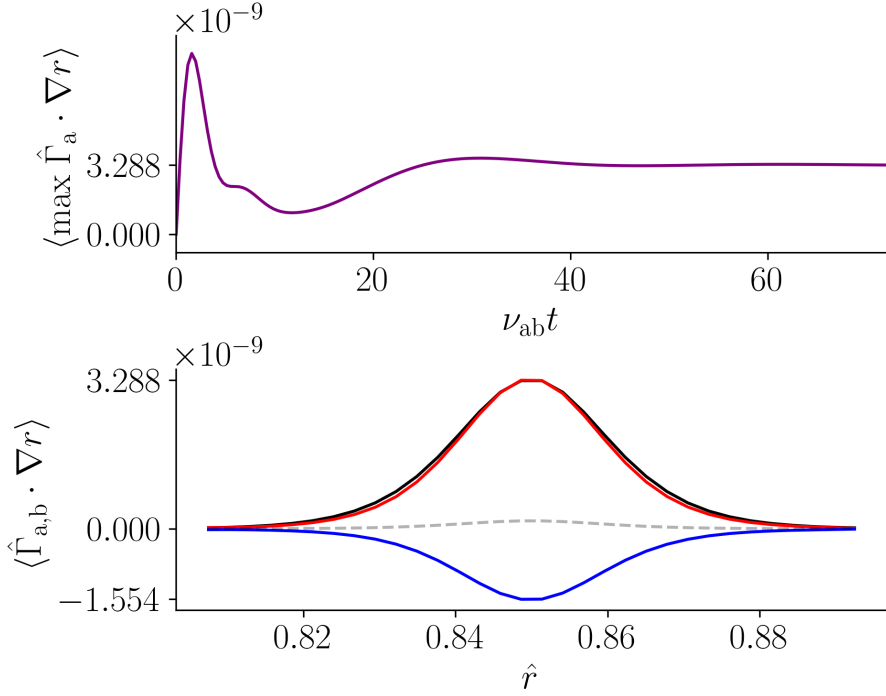
Figure 4.5. (Top panel): Maximum of $\langle \hat{\Gamma}_a \cdot \nabla r \rangle$ along the radius plotted against time, showing the steady state.
(Bottom panel) The radial profile of $\langle \hat{\Gamma}_a \cdot \nabla r \rangle$ is positive and shown as a solid red curve, and is in good agreement with Eq. (4.70) shown with a black curve. The blue curve shows the radial profile of $\langle \hat{\Gamma}_b \cdot \nabla r \rangle$, and the gray dashed curve verifies the ambipolarity condition Eq. (4.72). Particle flux is normalized by $n_{a,0} v_{Ta}$, distance by $\tilde{l} = 1$ m. $|v_{||}|_{\max}/v_{Ta} = 6$, $\mu_{\max} B/T_a = 6$, $n_{v_{||}} = 96$, $n_\mu = 48$, $n_\theta = 32$, $n_r = 32$.

is

$$\left\langle \sum_s \frac{c^2 n_s m_s}{B^2} |\nabla \psi|^2 \right\rangle \frac{\partial \Phi}{\partial \psi} = \int_0^t dt \langle \nabla \psi \cdot \sum_s \mathbf{j}_s \rangle, \tag{4.68}$$

where ψ denotes the flux surface and $\mathbf{j}_s$ is the gyrocenter current density given by

$$\mathbf{j}_s = \frac{2\pi e_s}{m_s} \int \dot{\mathbf{R}}_s f_s B_{||}^* dv_{||} d\mu_s. \tag{4.69}$$

We solve Eq. (4.66) with Neumann radial boundary conditions together with the gyrokinetic equation Eq. (4.1) in the annular toroidal geometry. We run simulation for about $100/\nu_{ab}$ to allow for collisional GAM [76] relaxation and the establishment of steady radial profiles for radial particle fluxes. We analyze simulation results by using the analogy [56] between electron-ion and proton-heavy impurity transport problems. In the ion-heavy impurity problem, the protons (species a) play the role of "electrons", while the impurities (species b) play the role of "protons" in the Braginskii treatment. In the electron-ion problem, the electron-electron collision operators scale as n_e and electron-ion collision operator scale as $n_i Z^2$. In the ion-impurity problem considered here, ion-ion collision operators scale as n_a and the ion-impurity collision operator scales as $n_b Z_b^2$. This suggests [56] that the ion-heavy impurity transport problem is analogous to the electron ion problem of Braginskii for the case of the ion charge Z_b given by $\alpha = n_b e_b^2/(n_a e_a^2)$. In the high aspect ratio $\epsilon = r/R \ll 1$ toroidal geometry, it was shown [56] that the radial magnetic surface averaged particle $\langle \Gamma_a \cdot \nabla r \rangle$ flux can be expressed in terms of the parallel transport coefficients C_1, C_2 and C_3 from Eqs. (4.52)-(4.53) as

$$\begin{aligned}
\langle \Gamma_a \cdot \nabla r \rangle = -2q^2 D_a n_a \bigg(&\left(C_1 + \frac{C_2^2}{C_3} \right) \times \\
&\times \left(\frac{\partial \ln p_a}{\partial r} - \frac{T_b}{Z_b T_a} \frac{\partial \ln p_a}{\partial r} \right) - \frac{5}{2} \frac{C_2}{C_3} \frac{\partial \ln T_a}{\partial r} \bigg),
\end{aligned} \tag{4.70}$$

86

where

$$D_{\mathrm{a}} = \frac{T_{\mathrm{a}}}{\tau_{\mathrm{ab}}\Omega_{\mathrm{a}}^2 m_{\mathrm{a}}}. \tag{4.71}$$

In a quasi-stationary state, the flux surface averaged impurity flux $\langle\Gamma_{\mathrm{b}} \cdot \nabla r\rangle$ is related to the corresponding main ion flux $\langle\Gamma_{\mathrm{a}} \cdot \nabla r\rangle$ by the ambipolarity condition,

$$e_{\mathrm{a}}\langle\Gamma_{\mathrm{a}} \cdot \nabla r\rangle + e_{\mathrm{b}}\langle\Gamma_{\mathrm{b}} \cdot \nabla r\rangle = 0, \tag{4.72}$$

because of the momentum conservation during the unlike-species collisions. The constraint in Eq. (4.72) is also consistent with the quasi-neutrality requirement. Indeed, for a quasi-stationary state where the polarization current can be neglected, the total flux surface average neoclassical radial current has to be zero. Recalling that a Boltzmann electron response given by Eq. (4.64) yields a zero electron flux-surface average current, we obtain Eq. (4.72). Since for our simulations $\alpha = 1$, in the radial flux expression Eq. (4.70) we use transport coefficients for $Z_{\mathrm{b}} = 1$, obtained in Sections 4.3.1 and 4.3.2 from the simulations with Abel collision operator C_{A} that was used to model like-species collisions in the Miller geometry simulations discussed in this section. The resulting predicted surface averaged particle flux profile $\langle\Gamma_{\mathrm{a}} \cdot \nabla r\rangle$ agrees with results from the COGENT simulation, as illustrated in Fig. (4.5). The ion and impurity radial particle fluxes are related by ambipolarity Eq. (4.72) condition, as expected from the analysis above. These results demonstrate the consistency of COGENT neoclassical simulations with theory [56] and results from slab geometry simulations discussed in Sections 4.3.1 and 4.3.2.

4.4   Conclusion and discussion

In this chapter, we report on the implementation and testing of a model unlike-particle linearized collision operator in the gyrokinetic continuum code COGENT. This

operator is similar to the model operators for unlike-species collisions developed for delta-f simulations in Refs. [55, 42] and it is based on the linearization of the Landau operator. However, the newly implemented operator also retains collisional thermalization of Maxwellian backgrounds for the case of different species temperatures. It conserves particle number, momentum, and energy of colliding species, is self-adjoint for equal background temperatures of colliding species, and preserves the velocity dependence of the Coulomb mean free path. The latter property is critically important to recover the thermal force from the unlike-species collisions. The model operator is tested in simulations of parallel plasma transport in a uniform slab geometry by considering a large species mass ratio ($m_a/m_b = 100$) and a strongly collisional regime. This problem is analogous to the electron-ion transport problem analyzed by Braginskii, and we analyze our simulation results by using the Braginskii model. For the case where like-particle collisions within the light species are modeled with the Fokker-Planck operator, the parallel transport coefficients obtained in the COGENT simulations are within $3 - 6\%$ of the corresponding Braginskii's results. When we replace the Fokker-Planck operator with the previously implemented Abel linearized operator for self-collisions, we obtain coefficients within 20% of Braginskii's results. In addition, we verify the Onsager symmetry of the transport coefficients, which follows from the self-adjointness property of the collision model for equal background temperatures. Finally, we simulate the Pfirsch-Schlüter problem of the radial ion-heavy impurity transport in a toroidal geometry, and recover the theoretical expression [56] for radial neoclassical fluxes in terms of parallel transport coefficients.

The ability of the implemented operator to recover the thermal force is important for simulating experimentally relevant plasma, since this force is widely recognized [6, 52, 53] to play one of the major roles in impurity transport in a tokamak edge. We, however, note that an ion distribution function can substantially deviate from a Maxwellian background in regions with a steep profile variations (e.g., under H-mode conditions). Because the operator presented here is linearized, it is only applicable to problems where the bulk

distribution functions of all colliding species are Maxwellian. However, when the bulks are Maxwellian, the linear operator allows simulating plasma transport influenced by the energetic components δf of the distribution functions, which are typically non-Maxwellian in the tokamak edge region. For example, high-energy tails δf carry [7] significant part of the parallel electron heat flux, which can be illustrated as follows. In the steady state of highly collisional electron-proton plasma with species densities n_e and bulk Maxwellian distribution of electrons $f_e = f_e^M + \delta f_e$, $\delta f_e \ll f_e^M$, the non-Maxwellian component δf_e can be estimated from

$$v_x \frac{\partial f_e^M}{\partial x} \approx -\frac{4\pi n_e e^4 \ln \Lambda}{m_e^2 v^3} \delta f_e, \tag{4.73}$$

where x is the direction of the electron temperature gradient $T_e = T_e(x)$ and the mean velocity of the electron bulk f_e^M is zero. The electron heat flux is then

$$q_e = \int d\mathbf{v} \frac{m_e v^2}{2} v_x f_e = \int d\mathbf{v} \frac{m_e^3 v^5}{8\pi n_e e^4 \ln \Lambda} v_x^2 \left(\frac{3}{2} \frac{1}{T_e} - \frac{m_e v^2}{2 T_e^2} \right) f_e^M \frac{dT}{dx}. \tag{4.74}$$

Observe that a significant contribution to the electron heat flux comes from the super-thermal tail of the electron distribution function, $\sim \int v^{11} f_e^M dv$. For this super-thermal tail to be nearly Maxwellian requires the Coulomb mean free path λ_C of thermal electrons to be much shorter than the electron gradient scale length $\lambda_C |d \ln T_e/dx| \ll 10^{-2}$. This condition is not met [77] in the tokamak edge plasmas, even in regions with a Maxwellian bulk. For such regimes, kinetic simulations with the COGENT linearized collision operator Eq. (4.6) can be used to model the non-Maxwellian components of the distribution functions and the resulting parallel heat flux. Apart from contributing the majority of parallel heat fluxes as shown above, high-energy tails of distribution functions also increase [77] the sheath potential, enhancing ion acceleration towards the divertor, which results in additional sputtering and hot spot [78] formation. For cold plasmas with temperatures below the

inelastic excitation process thresholds, high-energy electron tails significantly alter the excitation rate of high-Z impurities. In addition, kinetic simulation of the energetic tails of distribution functions can help to interpret plasma diagnostics, addressing the discrepancies in, for example, the difference [79] in temperature measured with a Langmuir probe versus Thomson scattering.

However, as noted earlier, the assumptions employed to achieve the numerical efficiency of the collision operator can compromise the fidelity of the simulation with similar masses of colliding species. This limitation can be addressed with further model enhancements [43] or by simulating collisions with a full Landau operator.

The work presented in this chapter is a reprint of the material as it appears in *Implementation and verification of a model linearized multi-species collision operator in the COGENT code* in Computer Physics Communications 291 (2023) 108829, by A. R. Knyazev, M. Dorf, and S. I. Krasheninnikov. The dissertation author was the primary investigator and author of this paper.

Chapter 5

Summary

The main goal of this thesis is to compose and apply reduced models to analyze kinetic effects in various plasma setups. This is accomplished through analytical work and numerical modeling, including direct simulation of the kinetic equation.

The previous analysis of electron dynamics in the counter-propagating linearly polarized laser plane waves is extended to the case of arbitrary canonical momenta of the electron in the plane of colliding waves, for both parallel and perpendicular polarizations. Using the 3/2-dimensional Hamiltonian formalism to describe the electron motion, the onset of stochastic electron dynamics and the role of stochasticity in electron acceleration is investigated. Using this one-particle model, it is demonstrated that large perpendicular canonical momentum $\mathbf{P}_\perp \gg a_1$ suppresses the long harmonic tail in the unperturbed electron motion (the motion of in the field of main laser a_1). In agreement with the Chirikov resonance cut-off criterion, suppression of harmonics decreases the stochasticity region, resulting in suppressed stochastic heating. This physical picture agrees with the obtained analytical estimates for the stochasticity boundaries, which in turn agree with the direct simulations of Hamiltonian equations. The model is further extended to include the effects of radiation friction (RF), and it is demonstrated that the Hamiltonian analysis results remain valid within the applicability of classical RF approximation.

The interaction of a relativistic laser with a structured nanoplate target is considered

using direct kinetic simulations and reduced analytical models. The semi-analytical model for the onset of the quasi-static electromagnetic fields within the target is proposed and verified against the kinetic simulation results. Stochastic electron acceleration in the presence of laser and quasi-static electromagnetic laser fields is analyzed using a one-particle model. Electron dynamics is described using the 3/2-dimensional Hamiltonian. Using this Hamiltonian model, the residue between the amplitude of the quasi-static electric and magnetic fields of the target is identified as the key parameter for the stochastic electron acceleration beyond the ponderomotive scaling. Although the described model neglects many effects of the laser-target interaction, it illustrates the mechanism of producing energetic electrons via stochastic heating in laser-target interactions.

A linearized multi-species collision operator model is implemented in the gyrokinetic code COGENT to study the impurity transport. Conservation of energy, momentum, and density during the collision is demonstrated. The newly implemented model is tested in the high collisionality and high mass ratio regime, and results are analyzed using the Braginskii fluid model. The operator's ability to recover thermal force is demonstrated, which is important for impurity transport simulation. For the uniform slab geometry, strongly collisional plasma with mass ratio of 100, the linearized multi-species collision operator produces parallel transport coefficients in good agreement with Braginskii's results when the full Fokker-Planck operator is used to model like-species collisions. Furthermore, transport coefficients remain within 20% of Braginskii values when Abel model operator instead of the Fokker-Planck operator. The slab geometry results are verified to be in agreement with the simulations of Pfirsch-Schlüter radial ion-heavy impurity transport problem in toroidal geometry. Although the newly implemented model operator may not produce accurate transport coefficients for plasmas with similar mass ratios, this limitation can be addressed in future work. Meanwhile, the ability of the operator to retain thermal force enables analysis of neoclassical impurity transport with the COGENT code.

Bibliography

[1] Georgii M Zaslavskii, Roal'd Z Sagdeev, Daniel'a Usikov, and Aleksandr A Chernikov. *Weak chaos and quasi-regular structures*. Weak chaos and quasi-regular structures Izdatel'stvo Nauka, 1991.

[2] Gerard A Mourou, Toshiki Tajima, and Sergei V Bulanov. Optics in the relativistic regime. *Reviews of modern physics*, 78(2):309, 2006.

[3] C Joshi, S Corde, and WB Mori. Perspectives on the generation of electron beams from plasma-based accelerators and their near and long term applications. *Physics of Plasmas*, 27(7), 2020.

[4] Fred L Hinton. Collisional transport in plasma. *Handbook of Plasma Physics*, 1(147):331, 1983.

[5] Lev Davidovich Landau. Kinetic equation for the coulomb effect. *Phys. Z. Sowjetunion*, 10:154, 1936.

[6] SI Braginskii. Transport processes in a plasma, in reviews of plasma physics, vol. 1 (ma leontovich ed.). *Consultants Bureau, New York*, 1965.

[7] DR Gray and JD Kilkenny. The measurement of ion acoustic turbulence and reduced thermal conductivity caused by a large temperature gradient in a laser heated plasma. *Plasma Physics*, 22(2):81, 1980.

[8] Sven Wiesen, Detlev Reiter, Vladislav Kotov, Martine Baelmans, Wouter Dekeyser, AS Kukushkin, SW Lisgo, RA Pitts, Vladimir Rozhansky, Gabriella Saibene, I Veselova, and S. Voskoboynikov. The new solps-iter code package. *Journal of nuclear materials*, 463:480–484, 2015.

[9] Hazime Mori. Transport, collective motion, and brownian motion. *Progress of theoretical physics*, 33(3):423–455, 1965.

[10] Albert Einstein et al. On the motion of small particles suspended in liquids at rest required by the molecular-kinetic theory of heat. *Annalen der physik*, 17(549-560):208, 1905.

[11] Valery I Klyatskin. *Lectures on dynamics of stochastic systems*. Elsevier, 2010.

[12] Allan J Lichtenberg and Michael A Lieberman. *Regular and stochastic motion*, volume 38. Springer Science & Business Media, 2013.

[13] Roal'd Z Sagdeev, Danièl' Alekseevich Usikov, and George M Zaslavsky. Nonlinear physics. from the pendulum to turbulence and chaos. *nppt*, 1988.

[14] GM Zaslavskii and Boris Valerianovich Chirikov. Stochastic instability of non-linear oscillations. *Soviet Physics Uspekhi*, 14(5):549, 1972.

[15] Enrico Fermi. On the origin of the cosmic radiation. *Physical review*, 75(8):1169, 1949.

[16] JT Mendonca. Threshold for electron heating by two electromagnetic waves. *Physical Review A*, 28(6):3592, 1983.

[17] Jean-Marcel Rax. Compton harmonic resonances, stochastic instabilities, quasilinear diffusion, and collisionless damping with ultra-high-intensity laser waves. *Physics of Fluids B: Plasma Physics*, 4(12):3962–3972, 1992.

[18] Z-M Sheng, K Mima, Y Sentoku, MS Jovanović, T Taguchi, J Zhang, and J Meyer-ter Vehn. Stochastic heating and acceleration of electrons in colliding laser fields in plasma. *Physical review letters*, 88(5):055004, 2002.

[19] SG Bochkarev, E d'Humières, VT Tikhonchuk, Ph Korneev, and V Yu Bychenkov. Stochastic electron heating in an interference field of several laser pulses of a picosecond duration. *Plasma Physics and Controlled Fusion*, 61(2):025015, 2019.

[20] Kathleen Weichman, Alexander PL Robinson, Farhat N Beg, and Alexey V Arefiev. Laser reflection as a catalyst for direct laser acceleration in multipicosecond laser-plasma interaction. *Physics of Plasmas*, 27(1):013106, 2020.

[21] AJ Kemp and SC Wilks. Direct electron acceleration in multi-kilojoule, multi-picosecond laser pulses. *Physics of Plasmas*, 27(10):103106, 2020.

[22] Yanzeng Zhang and Sergei Krasheninnikov. Novel approach to stochastic acceleration of electrons in colliding laser fields. *Physics of Plasmas*, 26(5):050702, 2019.

[23] Lev Davidovich Landau. *The classical theory of fields*, volume 2. Elsevier, 2013.

[24] Tatsufumi Nakamura. Stationary solutions of equations of motion for a radiating charged particle including a radiation reaction effect. *Physical Review E*, 102(3):033210, 2020.

[25] BS Paradkar, MS Wei, T Yabuuchi, RB Stephens, MG Haines, SI Krasheninnikov, and FN Beg. Numerical modeling of fast electron generation in the presence of preformed plasma in laser-matter interaction at relativistic intensities. *Physical Review E*, 83(4):046401, 2011.

[26] MM Murnane, HC Kapteyn, SP Gordon, J Bokor, EN Glytsis, and RW Falcone. Efficient coupling of high-intensity subpicosecond laser pulses into solids. *Applied physics letters*, 62(10):1068–1070, 1993.

[27] Michael A Purvis, Vyacheslav N Shlyaptsev, Reed Hollinger, Clayton Bargsten, Alexander Pukhov, Amy Prieto, Yong Wang, Bradley M Luther, Liang Yin, Shoujun Wang, and Jorge J. Rocca. Relativistic plasma nanophotonics for ultrahigh energy density physics. *Nature Photonics*, 7(10):796, 2013.

[28] G Kulcsar, D AlMawlawi, FW Budnik, PR Herman, M Moskovits, L Zhao, and RS Marjoribanks. Intense picosecond x-ray pulses from laser plasmas by use of nanostructured "velvet" targets. *Physical Review Letters*, 84(22):5149, 2000.

[29] FY Khattak, RJ Clarke, EJ Divall, M Edwards, PS Foster, CJ Hooker, AJ Langley, P Mistry, D Neely, OAMB Percie du Sert, J Smith, C Spindloe, G Tallents, M Tolley, and D Riley. Enhanced he-α emission from "smoked" ti targets irradiated with 400 nm, 45 fs laser pulses. *EPL (Europhysics Letters)*, 72(2):242, 2005.

[30] Luca Fedeli, Arianna Formenti, Lorenzo Cialfi, Andrea Pazzaglia, and Matteo Passoni. Ultra-intense laser interaction with nanostructured near-critical plasmas. *Scientific reports*, 8(1):3834, 2018.

[31] Joseph Snyder, LL Ji, Kevin M George, Christopher Willis, Ginevra E Cochran, RL Daskalova, Abraham Handler, Trevor Rubin, Patrick L Poole, Derek Nasir, Anthony Zingale, Enam Chowdhury, BF Shen, and DW Schumacher. Relativistic laser driven electron accelerator using micro-channel plasma targets. *Physics of Plasmas*, 26(3):033110, 2019.

[32] Yanzeng Zhang and SI Krasheninnikov. Electron dynamics in the laser and quasi-static electric and magnetic fields. *Physics Letters A*, 382(27):1801–1806, 2018.

[33] Yanzeng Zhang and SI Krasheninnikov. Electron heating in the laser and static electric and magnetic fields. *Physics of Plasmas*, 25(1):013120, 2018.

[34] Yanzeng Zhang, SI Krasheninnikov, and Alexey Knyazev. Stochastic electron heating in the laser and quasi-static electric and magnetic fields. *Physics of Plasmas*, 25(12):123110, 2018.

[35] SC Wilks, WL Kruer, M Tabak, and AB Langdon. Absorption of ultra-intense laser pulses. *Physical review letters*, 69(9):1383, 1992.

[36] Clayton Bargsten, Reed Hollinger, Maria Gabriela Capeluto, Vural Kaymak, Alexander Pukhov, Shoujun Wang, Alex Rockwood, Yong Wang, David Keiss, Riccardo Tommasini, Richard London, Jaebum Park, Michel Busquet, Marcel Klapisch, Vyacheslav N Shlyaptsev, and Jorge J Rocca. Energy penetration into arrays of aligned nanowires irradiated with relativistic intensities: Scaling to terabar pressures. *Science advances*, 3(1):e1601558, 2017.

[37] DA Gozhev, SG Bochkarev, NI Busleev, AV Brantov, SI Kudryashov, AB Savel'ev, and V Yu Bychenkov. Laser-triggered stochastic volumetric heating of sub-microwire array target. *High Energy Density Physics*, page 100856, 2020.

[38] TD Arber, Keith Bennett, CS Brady, A Lawrence-Douglas, MG Ramsay, NJ Sircombe, P Gillies, RG Evans, Holger Schmitz, AR Bell, and CP Ridgers. Contemporary particle-in-cell approach to laser-plasma modelling. *Plasma Physics and Controlled Fusion*, 57(11):113001, 2015.

[39] Lev Davidovich Landau, JS Bell, MJ Kearsley, LP Pitaevskii, EM Lifshitz, and JB Sykes. *Electrodynamics of continuous media*, volume 8. elsevier, 2013.

[40] AV Arefiev, APL Robinson, and VN Khudik. Novel aspects of direct laser acceleration of relativistic electrons. *Journal of Plasma Physics*, 81(4), 2015.

[41] National Institute of Standards and Technology (NIST). The estar stopping power and range tables by electrons https://physics.nist.gov/physrefdata/star/text/estar.html. Data for electrons in solid copper is used in this work.

[42] H Sugama, T-H Watanabe, and M Nunami. Linearized model collision operators for multiple ion species plasmas and gyrokinetic entropy balance equations. *Physics of Plasmas*, 16(11):112503, 2009.

[43] Hideo Sugama, Seikichi Matsuoka, Shinsuke Satake, Masanori Nunami, and T-H Watanabe. Improved linearized model collision operator for the highly collisional regime. *Physics of Plasmas*, 26(10):102108, 2019.

[44] Peter Donnel, Xavier Garbet, Yanick Sarazin, Virginie Grandgirard, Yuuichi Asahi, Nicolas Bouzat, Elisabetta Caschera, Guilhem Dif-Pradalier, Charles Ehrlacher, Philippe Ghendrih, Camille Gillot, Guillaume Latu, and Chantal Passeron. A multi-species collisional operator for full-f global gyrokinetics codes: Numerical aspects and verification with the gysela code. *Computer Physics Communications*, 234:1–13, 2019.

[45] Paul Crandall, Denis Jarema, Hauke Doerk, Q Pan, Gabriele Merlo, Tobias Görler, A Bañón Navarro, Daniel Told, Maurice Maurer, and Frank Jenko. Multi-species collisions for delta-f gyrokinetic simulations: Implementation and verification with gene. *Computer Physics Communications*, 255:107360, 2020.

[46] Manaure Francisquez, James Juno, Ammar Hakim, Gregory W Hammett, and Darin R Ernst. Improved multispecies dougherty collisions. *Journal of Plasma Physics*, 88(3):905880303, 2022.

[47] Philipp Ulbl, Dominik Michels, and Frank Jenko. Implementation and verification of a conservative, multi-species, gyro-averaged, full-f, lenard-bernstein/dougherty collision operator in the gyrokinetic code gene-x. *Contributions to Plasma Physics*, 62(5-6):e202100180, 2022.

[48] BJ Frei, S Ernst, and P Ricci. Numerical implementation of the improved sugama collision operator using a moment approach. *Physics of Plasmas*, 29(9):093902, 2022.

[49] Lev Davidovich Landau. Kinetic equation for the case of coulomb interaction. *Phys. Z. Sowjetunion.*, 10: 154–164., 1936.

[50] Robert Hager, ES Yoon, S Ku, Eduardo F D'Azevedo, Patrick H Worley, and Choong-Seock Chang. A fully non-linear multi-species fokker–planck–landau collision operator for simulation of fusion plasma. *Journal of Computational Physics*, 315:644–660, 2016.

[51] MA Dorf, RH Cohen, M Dorr, J Hittinger, and TD Rognlien. Progress with the cogent edge kinetic code: Implementing the fokker-planck collision operator. *Contributions to Plasma Physics*, 54(4-6):517–523, 2014.

[52] P. C. Stangeby. The magnitude and direction of forces on impurities near a divertor plate. an exploratory investigation. *CFFTP-G–9042*, 1990.

[53] Shohei Yamoto, Yuki Homma, Kazuo Hoshino, Mitsunori Toma, and Akiyoshi Hatayama. Impgyro: The full-orbit impurity transport code for sol/divertor and its successful application to tungsten impurities. *Computer Physics Communications*, 248:106979, 2020.

[54] Mikhail Dorf and Milo Dorr. Progress with the 5d full-f continuum gyrokinetic code cogent. *Contributions to Plasma Physics*, 60(5-6):e201900113, 2020.

[55] RA Kolesnikov, WX Wang, and FL Hinton. Unlike-particle collision operator for gyrokinetic particle simulations. *Journal of Computational Physics*, 229(15):5564–5572, 2010.

[56] Paul Harding Rutherford. Impurity transport in the pfirsch-schlüter regime. *The Physics of Fluids*, 17(9):1782–1784, 1974.

[57] RL Miller, MS Chu, JM Greene, YR Lin-Liu, and RE Waltz. Noncircular, finite aspect ratio, local equilibrium model. *Physics of Plasmas*, 5(4):973–978, 1998.

[58] MA Dorf, MR Dorr, JA Hittinger, RH Cohen, and TD Rognlien. Continuum kinetic modeling of the tokamak plasma edge. *Physics of Plasmas*, 23(5):056102, 2016.

[59] Mikhail Dorf and Milo Dorr. Continuum kinetic modelling of cross-separatrix plasma transport in a tokamak edge including self-consistent electric fields. *Contributions to Plasma Physics*, 58(6-8):434–444, 2018.

[60] Mikhail Dorf and Milo Dorr. Progress with the 5d full-f continuum gyrokinetic code cogent. *Contributions to Plasma Physics*, 60(5-6):e201900113, 2020.

[61] Andrew S Richardson. 2019 nrl plasma formulary. Technical report, US Naval Research Laboratory, 2019.

[62] B. A. Trubnikov. *Review of Plasma Physics*, volume 1. Consultants Bureau, New York, 1965.

[63] EA Belli and J Candy. Full linearized fokker–planck collisions in neoclassical transport simulations. *Plasma physics and controlled fusion*, 54(1):015015, 2011.

[64] Qingjiang Pan, Darin R Ernst, and Paul Crandall. First implementation of gyrokinetic exact linearized landau collision operator and comparison with models. *Physics of Plasmas*, 27(4):042307, 2020.

[65] RA Kolesnikov, WX Wang, FL Hinton, G Rewoldt, and WM Tang. Drift-kinetic simulation of neoclassical transport with impurities in tokamaks. *Physics of Plasmas*, 17(2):022506, 2010.

[66] D Estève, X Garbet, Y Sarazin, V Grandgirard, T Cartier-Michaud, G Dif-Pradalier, P Ghendrih, G Latu, and C Norscini. A multi-species collisional operator for full-f gyrokinetics. *Physics of Plasmas*, 22(12):122506, 2015.

[67] MA Dorf, RH Cohen, M Dorr, T Rognlien, J Hittinger, J Compton, P Colella, D Martin, and P McCorquodale. Simulation of neoclassical transport with the continuum gyrokinetic code cogent. *Physics of Plasmas*, 20(1):012513, 2013.

[68] IG Abel, M Barnes, SC Cowley, W Dorland, and AA Schekochihin. Linearized model fokker–planck collision operators for gyrokinetic simulations. i. theory. *Physics of Plasmas*, 15(12):122509, 2008.

[69] H Dreicer. Electron and ion runaway in a fully ionized gas. ii. *Physical review*, 117(2):329, 1960.

[70] Prabhu Lal Bhatnagar, Eugene P Gross, and Max Krook. A model for collision processes in gases. i. small amplitude processes in charged and neutral one-component systems. *Physical review*, 94(3):511, 1954.

[71] Andrew Lenard and Ira B Bernstein. Plasma oscillations with diffusion in velocity space. *Physical Review*, 112(5):1456, 1958.

[72] JP Dougherty. Model fokker-planck equation for a plasma and its solution. *The Physics of Fluids*, 7(11):1788–1799, 1964.

[73] Guilhem Dif-Pradalier, PH Diamond, Virginie Grandgirard, Yanick Sarazin, J Abiteboul, Xavier Garbet, Ph Ghendrih, Guillaume Latu, A Strugarek, S Ku, and Choong-Seock Chang. Neoclassical physics in full distribution function gyrokinetics. *Physics of Plasmas*, 18(6):062309, 2011.

[74] V.M. Zhdanov. *Transport processes in multicomponent plasma*. CPC Press, 2002.

[75] Mikhail Dorf and M Dorr. Continuum gyrokinetic simulations of edge plasmas in single-null geometries. *Physics of Plasmas*, 28(3):032508, 2021.

[76] SV Novakovskii, CS Liu, RZ Sagdeev, and MN Rosenbluth. The radial electric field dynamics in the neoclassical plasmas. *Physics of Plasmas*, 4(12):4272–4282, 1997.

[77] OV Batishchev, SI Krasheninnikov, Peter J Catto, AA Batishcheva, DJ Sigmar, XQ Xu, JA Byers, TD Rognlien, RH Cohen, MM Shoucri, et al. Kinetic effects in tokamak scrape-off layer plasmas. *Physics of Plasmas*, 4(5):1672–1680, 1997.

[78] AV Nedospasov and IV Bezlyudny. Hot spot formation on different tokamak wall materials. *Contributions to Plasma Physics*, 38(1-2):337–342, 1998.

[79] Oleg V Batishchev. Kinetic modeling of sol plasmas in tokamaks. *Contributions to Plasma Physics*, 38, 1998.